Università degli Studi di Bari "Aldo Moro"

Dipartimento Interateneo di Fisica "M. Merlin"

Dottorato di ricerca in Fisica

XXX ciclo

Settore scientifico disciplinare FIS/01

Fermi-LAT data analysis of young Supernova Remnants for Cosmic-ray acceleration studies

Dottorando:
Leonardo Di Venere
Supervisori:
Prof. Francesco Giordano
Dott. Mario Nicola Mazziotta

Coordinatore:
Ch.mo Prof. Gaetano Scamarcio

Esame finale 2018

Contents

List of Figures

List of Tables

Introduction

After more than one hundred years from the discovery of cosmic rays (CRs) by Victor Hess in 1912, the questions about their origin are still unsolved. Many observations have been performed, obtaining a great amount of data which now have to be put in the right place to solve the *puzzle* of cosmic rays.

The measurements of the spectrum and composition of CRs revealed that this "radiation" consists of charged particles which reach incredibly high energies, up to 10^{20} eV. Detailed information about their spectral features and composition provide many ingredients to understand the possible sites where CRs are accelerated up to these high energies and to study the propagation mechanisms that regulate their diffusion in our Galaxy.

In particular, CRs with energy up to 10^{18} eV are thought to be of Galactic origin and the study of Galactic objects is fundamental to look for the CR sources. In 1949, Enrico Fermi proposed an efficient mechanism through which charged particles could be accelerated, which requires only the presence of a strong shock wave. We know that our Galaxy is full of these shock waves, deriving from the Supernovae explosions, which represent the final stage of the evolution of massive stars. For this reason, Supernova Remnants (SNRs) are considered the most plausible candidates to be sources of the Galactic CRs. This hypothesis is known as *SNR paradigm for CRs*.

The Fermi acceleration mechanism, also known as diffusive shock acceleration (DSA), predicts that a strong shock wave propagating in the interstellar medium naturally accelerate particles producing a power-law particle distribution with spectral index equal to -2. This aspect is in good agreement with the CR measurements at the Earth, through which a prediction of the CR spectrum at the source can be performed.

Unfortunately, CR measurements cannot give direct information about the source. Actually, the charged particles produced at the source are deflected by the Galactic magnetic field during their propagation to the Earth and all the directional information is lost.

Nevertheless, CRs continuosly interact with the environment their encounter at the source and in the Galaxy and inevitably emit non-thermal radiation, which can be detected and used to point directly to the source. As a consequence, the study of the electromagnetic spectrum emitted by CR sources from radio to the TeV energy range becomes crucial to understand the acceleration mechanisms. In particular, γ-rays from few tens of MeV to several tens or hundreds of TeV can trace the non-thermal emission of the accelerated cosmic-ray protons.

Fermi-LAT is a γ-ray imaging satellite and has among its scientific goals the study of astrophysical objects in the γ-ray spectrum, such as Supernova Remnants. It is sensitive in the energy range from few tens of MeV to few TeV. In particular, the energy range around and below 100 MeV is crucial to disentangle leptonic from hadronic contribution to the γ-ray spectrum.

The work of this thesis is set in this frame and focuses on the γ-ray analysis of two young SNRs with the *Fermi*-LAT data. Young SNRs are particularly interesting candidates, since their evolution can be studied in detail and they usually expand in clean environments. Furthermore, they are the ideal candidates to understand the maximum energy at which CRs could be accelerated in SNRs, being the energy losses still negligible.

The thesis is divided into six chapters. In chapter 1, the main features of cosmic rays will be described, focusing on the their spectral features and composition. A description of the diffusion mechanism in the Galaxy will be also given. The non-thermal emission processes through which cosmic rays emit photons from radio band to the very high energy γ-rays will be described.

In chapter 2, Supernova Remnants (SNRs) will be described, in order to understand why they are considered good candidates to accelerate cosmic rays. In the second part of the chapter, the attention will be focused on the main acceleration mechanisms which are thought to happen in SNRs. Finally a review of the most recent detection of SNRs in the γ-rays with the *Fermi*-LAT experiment will be provided.

In chapter 3, the γ-ray data analysis with *Fermi*-LAT data will be described. In te first part of the chapter the LAT experiment will be described, while in the second part the data analysis technique will be described.

In chapter 4, one of the main ingredients of the *Fermi*-LAT data analysis will be described: the background diffuse model. A description of the methods followed to derive will be given, in order to highlight the strong and weak points of the procedure and understand how the background diffuse model can affect the spectrum of the sources.

Chapter 5 will be dedicated to the presentation of the *Fermi*-LAT data analysis performed on two young SNRs: Cassiopeia A and Tycho. The first results will show how the diffuse model affects the source sepctrum. The analysis will aim on a better description of the diffuse model in order to get a more reliable results on the sources under investigation. In the second part of the chapter, the systematic uncertainties from the background model will be investigated. The standard methods based on the usage of alternative background models will be applied to the sources analysed. A new approach will be also developed and shown. This new approach consists in the study of the residuals of the baseline background model. Results obtained with this new approach will be shown and compared to the other methods applied.

Finally, chapter 6 will be dedicated to the description of an interpretation model for the spectra of the two sources. The model will be applied to obtain information on the CR spectra at the sources. The model derived will be also compared to other models previously developed.

Chapter 1

Cosmic rays: features and origin

1.1 Introduction

Cosmic rays (CRs) are charged particles coming from the outer space. They were discovered by Victor Hess in 1912, who noticed that the ionizing radiation observed at the surface of the Earth, whose origin was initially attributed to the natural radioactivity of the Earth, increased with altitude, proving that this "radiation" was not coming from the Earth. Later observations showed that this radiation was made of charged particles, with energy up to few 10^{20} eV, an incredibly high value if compared to the energies reached in modern accelerators.

Cosmic rays are classified as primary or secondary. The particles directly produced and accelerated at the source are defined as *Primary Cosmic Rays*. They are mostly made of protons, helium nuclei and electrons, as well as carbon, oxygen, iron, and other nuclei synthesized in stars. After their production, primary CRs are injected in the environment and propagate to the Earth. During this process they interact with the medium they come across and produce other particles, called *Secondary Cosmic Rays*. Nuclei such as lithium, beryllium, and boron (which are not abundant end-products of stellar nucleosynthesis) are part of this category. Antimatter is also produced in these interaction, especially antiprotons and positrons, and is observed at the Earth as secondary CRs. Recent measurements by PAMELA and AMS-02 have revealed an overabundance of positrons [1, 2] with respect to the predictions of the standard CR propagation models, opening to the possibility of new antimatter sources, both of astrophysical (pulsar) or exotic (dark matter) origin.

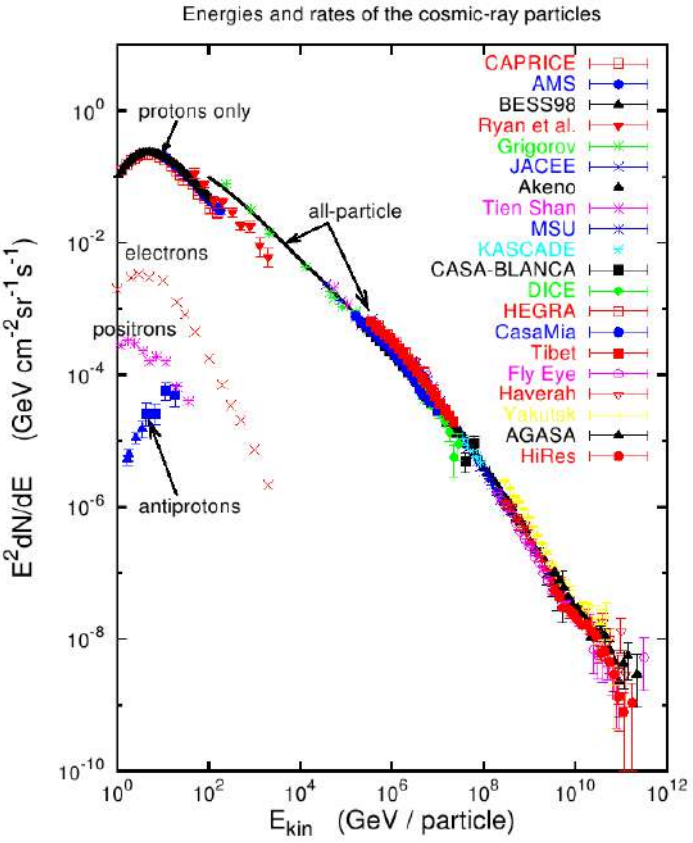

FIGURE 1.1: Cosmic-ray spectrum as measured by different experiments [3].

1.2 Spectrum

Figure 1.1 shows the energy spectrum of cosmic rays, which is the number of particles per unit time and unit solid angle incident on a unit area surface orthogonal to the direction of observation. The spectrum is well described by a power-law distribution over a wide energy range, from few hundreds MeV up to about a hundred EeV. The differential energy spectrum has been multiplied by E^2 in order to display the features of the steep spectrum that are otherwise difficult to discern.

For energy below 1 GeV, the spectrum presents a cut-off relative to the power-law distribution, due to the solar effects on charged particles. In fact, during the periods of high solar activity, the charged plasma emitted by the Sun, called *solar wind*, interacts with the incoming CRs, preventing their propagation to the Earth and reducing the observed flux. Conversely, the CR flux reaches its maximum during the periods of low solar activity. This phenomenon is known as *solar modulation* and has a cycle of about 11 years.

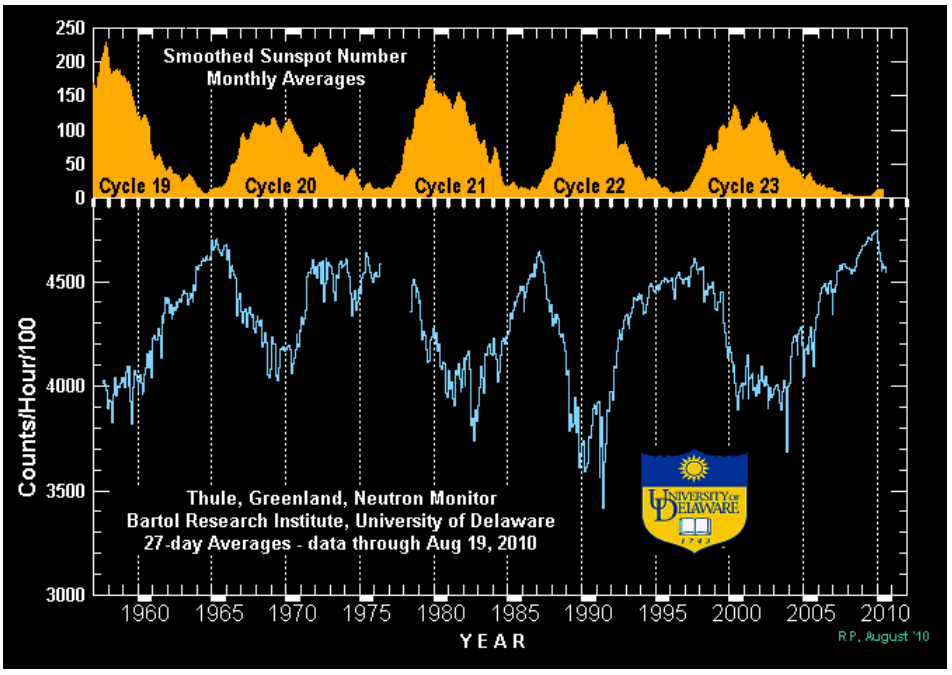

FIGURE 1.2: Number of sunspots and rate of cosmic rays from neutron monitors since 1958 [4]. The anti-correlation of these two quantities with a period of 11 years gives a strong evidence of the solar modulation of cosmic rays.

The evidence of this phenomenon is obtained through the measurements of the intensity of cosmic rays through neutron monitors, which detect the number of neutrons generated in the interaction of primary CRs with the Earth's atmosphere. An (anti-)correlation is observed between the measured rate of neutrons and the number of sunspots, whose presence was first noticed by Galileo Galilei in the XVII century and is a visible sign of the high solar activity (see figure 1.2).

For energies above few tens of GeV, particles are not affected by the solar wind and their spectrum follows a power-law:

$$F(E) = E^{-\alpha}, \tag{1.1}$$

where α represents the spectral index of the distribution. Its value changes significantly in two points of the spectrum. The first break, known as *knee*, occurs at an energy around 10^{15} eV, where the spectral index changes from a value of 2.7 to a value of 3. For energies above 10^{19} eV, which corresponds to the second break in the spectrum and is known as *ankle*, the spectral index becomes again 2.7. Figure 1.3 shows the "all-particle" spectrum observed by air shower experiments at energies greater than 100 TeV, which measure the energy of the incoming cosmic ray through the observation of the shower produced in the interaction with the

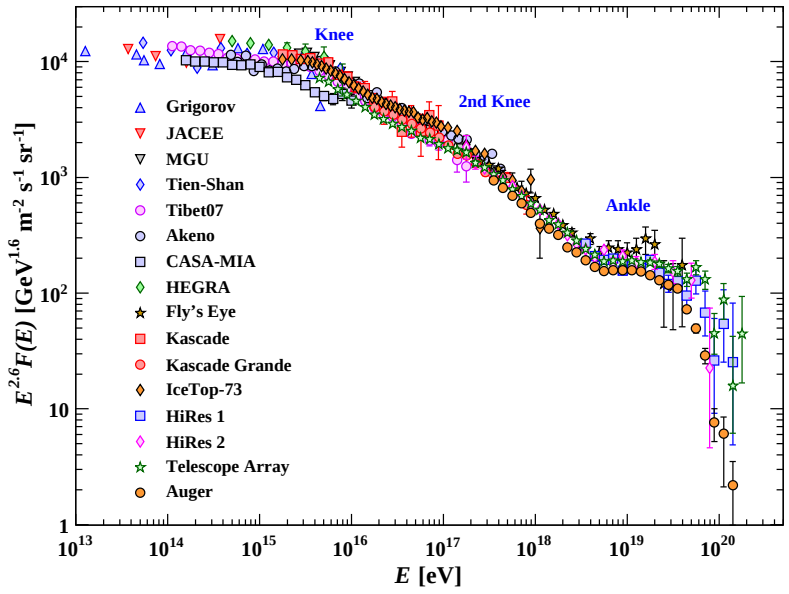

FIGURE 1.3: The "all-particle" spectrum as a function of energy-per-nucleus measured by air shower experiments [5].

atmosphere. In this case, the differential energy spectrum has been multiplied by $E^{2.6}$ in order to display the different values of the spectral index.

The features observed in the spectrum may give information about the origin of cosmic rays. Particles with energy below 10^{18} eV are thought to be of galactic origin. In this picture, the *knee* could originate from the fact that most of cosmic ray accelerators in the Galaxy have reached their maximum energy of acceleration between 10^{15} eV and 10^{18} eV, causing a break in the spectrum observed at the Earth. Actually, the spectrum produced by a single source with a maximum energy $E_{\max}$ would be described by an exponential cut-off. The combination of different exponential cut-off energies in the range 10^{15} eV - 10^{18} eV would result in a steepening of the power-law spectrum. The Kascade-Grande experiment reported the observation of a second steepening of the spectrum near $8 \cdot 10^{16}$ eV, with evidence that this structure is accompanied by a transition to heavy primaries. This is expected since the maximum energy of acceleration scales with the charge of the particle.

Supernova remnants are considered good candidates for the acceleration of cosmic

rays up to energies close to the *knee*. As it will be shown later, the Fermi acceleration mechanism predicts that a shock, like the one originating in a Supernova explosion, can accelerate charged particles, producing a power-law spectrum. Effects of propagation and confinement in the Galaxy also need to be considered, since they modify the observed spectrum of cosmic rays with respect to the one produced at the source.

Concerning the *ankle*, the hardening of the spectrum above 10^{18} eV might be due to a higher energy population for example with extragalactic origin, overtaking the Galactic population. In this case, the most probable candidates to accelerate cosmic rays up to these energies are the Active Galactic Nuclei (AGN), which emit a bright radiation in the entire electromagnetic spectrum.

1.2.1 GZK cut-off

The hypothesis of the extragalactic origin of cosmic rays with energy above the *ankle*, called Ultra-High Energy Cosmic Rays (UHECR), is reinforced by the observation of a cut-off in the spectrum for energy above $5 \cdot 10^{19}$ eV, known as Greisen-Zatsepin-Kutzmin (or GZK) cut-off. This phenomenon appears when the energy of cosmic-ray protons is sufficiently high to activate the photo-pion and photo-pair production processes.

If a proton is bombarded with high energy γ-rays, pions are created:

$$\gamma + p \rightarrow n + \pi^+, \tag{1.2}$$

$$\gamma + p \rightarrow p + \pi^0 \rightarrow p + \gamma + \gamma, \tag{1.3}$$

$$\gamma + p \rightarrow n + N\pi. \tag{1.4}$$

The photon threshold energy for these reactions is approximately $\epsilon_t = 200$ MeV and the cross section is about 250 μbn $= 2.5 \cdot 10^{-28}$ cm^2.

All the free space in the Universe is permeated by photons of the Cosmic Microwave Background (CMB), which is the thermal radiation assumed to be the left over of the Big Bang, and therefore cosmic rays cannot escape from it. The CMB spectrum is described by a black body spectrum with a temperature of approximately 2.7 K, corresponding to an average energy of $\epsilon_0 = 6 \cdot 10^{-4}$ eV, which is much lower than the threshold energy ϵ_t. However, in the rest frame of a cosmic-ray proton

with Lorentz factor Γ, this energy becomes

$$\epsilon = \epsilon_0 \Gamma \left(1 + \beta \cos\theta\right), \tag{1.5}$$

where θ is the angle between the photon and the proton directions. If the Lorentz factor Γ is sufficiently high, this value can exceed the threshold ϵ_t, activating the photo-pion production. The threshold value for the Lorentz factor of the proton, obtained in the limit $\beta \to 1$ and $\cos\theta = 1$, is $\Gamma_t = \epsilon_t/(2\epsilon_0) = 1.7 \cdot 10^{11}$, corresponding to an energy $E = \Gamma_t m_p = 1.7 \cdot 10^{20}$ eV. The proper calculation involves integration over the Planck spectrum of the CMB and over all angles and in this case the proton threshold energy for the photo-pion production process decreases to $5 \cdot 10^{19}$ eV.

The mean free path for a single scattering is $\lambda = (\sigma_{p\pi} N_{ph})^{-1}$. Taking $N_{ph} = 5 \cdot 10^2$ cm^{-3} for the CMB and $\sigma_{p\pi} = 2.5 \cdot 10^{-28}$ cm^2, then $\lambda \approx 10^{25}$ cm ≈ 3 Mpc, which, assuming that the proton travels at the speed of light, corresponds to a propagation time of 10^7 years. The energy of the pion created in this process is Γm_π, so that the fractional loss of energy of the cosmic ray proton is $\Delta E/E \approx m_\pi/m_p \approx 1/10$. The total mean free path for the cosmic ray proton to lose all its energy corresponds to a propagation time of 10^8 years.

A similar calculation can be carried out for the photo-pair production process:

$$\gamma + p \to p + e^+ + e^-. \tag{1.6}$$

The threshold for this process is 1.02 MeV, about 200 times less than the photo-pion production mechanism, corresponding to a threshold proton energy of about 10^{18} eV. The cross-section for this process in the ultra-relativistic limit is $\sigma_{pair} = 10^{-26}$ cm^2, which is 40 times larger than $\sigma_{p\pi}$. However, each photo-pair production event removes only a fraction of 10^{-3} of the energy of the proton. As a result, the propagation time for the protons to lose all their energy is $2.5 \cdot 10^9$ years, which is 25 times longer than the previous case. As a consequence, this process is less important and it just results in a distortion of the particle spectrum down to energies of about 10^{18} eV.

In conclusion, if the extragalactic origin of UHECR is correct, a cut-off in the cosmic-ray energy spectrum is expected at about $5 \cdot 10^{19}$ eV for protons, which cannot have originated further than about 30 Mpc from our Galaxy. On the other

side, a Galactic population of cosmic rays with the same energy would not suffer of the same effect, since the propagation distances would be much shorter than the value of λ. In fact, at such a high energy, cosmic rays are not confined in the Galaxy by the Galactic magnetic field and propagate for distances of the order of the dimension of our Galaxy, which has a diameter of 30 kpc.

As can be seen in figure 1.3, very recent measurements of the cosmic-ray spectrum at energies above 10^{19} eV by some experiments like the Auger experiment seem to show this cut-off in the spectrum, supporting the extragalactic origin of UHECR.

1.3 Composition

The observations of cosmic rays at the top of the atmosphere show that about 98% of the particles are protons and nuclei, while the remaining 2% are electrons. Of the protons and nuclei, about 87% are protons, 12% are helium nuclei and the remaining 1% are heavier nuclei.

Figure 1.4 shows that the energy spectrum of each component is consistent with the overall spectrum up to energies close to the *knee*. The study of the relative abundances of these elements gives information about the acceleration mechanisms at the source and the propagation mechanisms in the Interstellar Medium (ISM).

1.3.1 Chemical abundances

The chemical abundances of elements in cosmic rays give important information about their origin and their propagation in the Galaxy. Figure 1.5 represents the relative abundances of elements observed in cosmic rays, compared to the ones observed in the Solar System.

The most important features which appear in this plot are the following:

- the odd-even effect in the relative stabilities of the nuclei, which is due to the pairing term in the binding energy of nuclei, is evident in both curves;
- the abundance peaks at carbon, nitrogen and oxygen and at the iron group are present in both curves, supporting the idea that these elements do have origin directly in the sources, thanks to processes typical of stellar evolution;

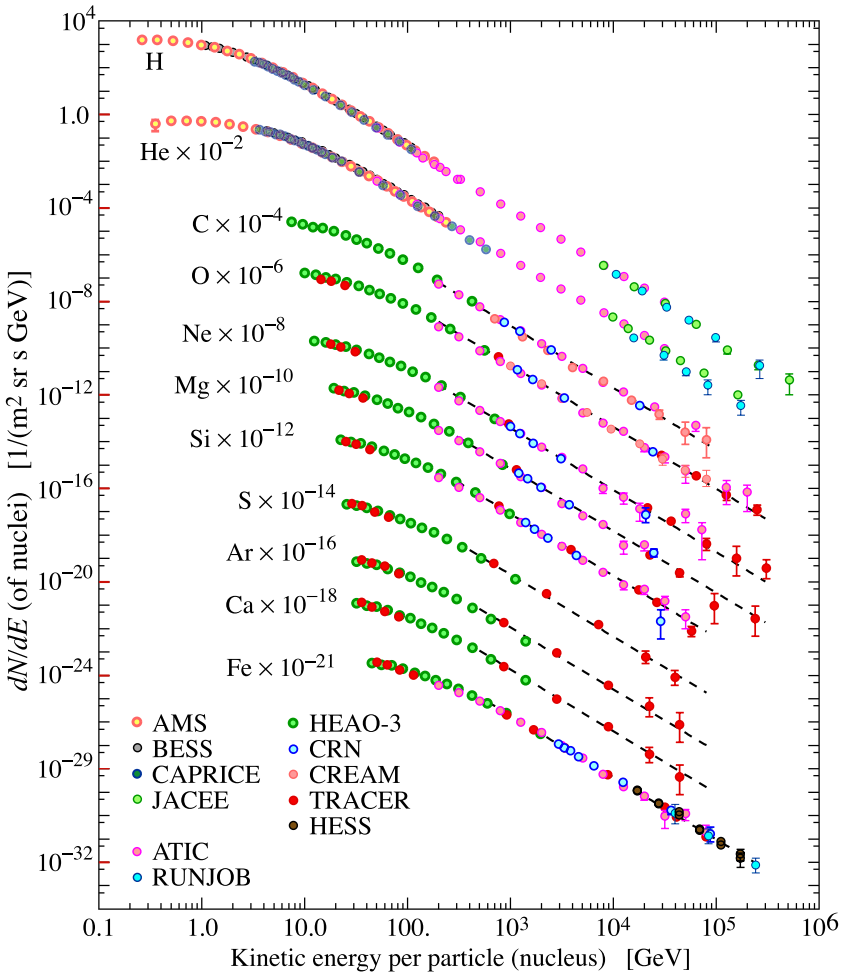

FIGURE 1.4: Fluxes of nuclei of the primary cosmic rays as a function of the kinetic energy per nucleus [5].

- in cosmic rays there is an overabundance of light elements (Li, Be, B) and of elements with atomic number just less than iron.

The last point can be attributed to the *spallation* mechanism. During their propagation to the Earth, primary cosmic ray nuclei collide with the gas in the interstellar medium and are fragmented, resulting in the production of nuclei with smaller atomic and mass number. In particular, spallation of *medium* group elements (carbon, nitrogen and oxygen) produces light elements like lithium, beryllium and boron, while spallation of iron results in nuclei like manganese, chromium and vanadium.

Spallation mechanism can be treated in a formal way using the diffusion-loss equation of cosmic rays, as it will be shown in section 1.4.1.

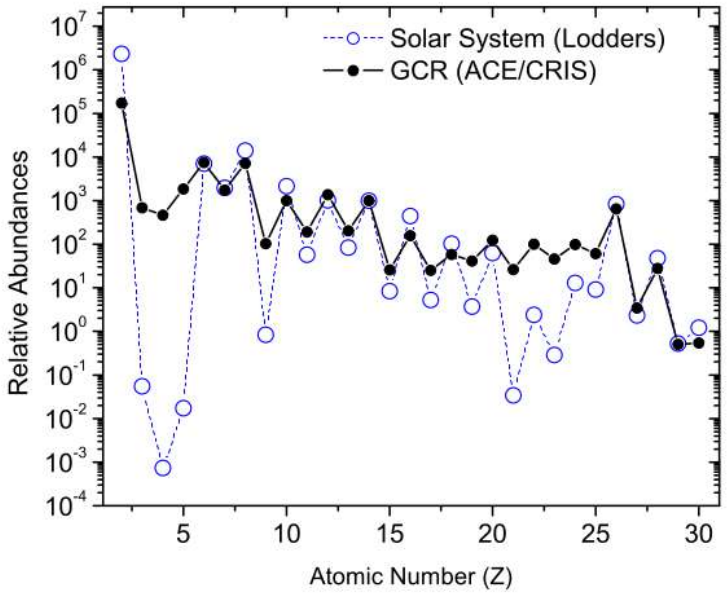

FIGURE 1.5: Abundances of elements observed in the cosmic rays by the Cosmic Ray Isotope Spectrometer (CRIS) compared to the Solar System abundances. Abundances normalized to the value of 1000 for Si. [6]

1.3.2 Isotopic abundances

In addition to overall chemical abundances, isotopic abundances are available for a number of species, in particular for the lightest elements ^{1}H, ^{2}H, ^{3}He and ^{4}He.

Most of helium was synthesised in the Hot Big Bang through the p-p chain. ^{2}H and ^{3}He, which are synthesised in the p-p chain as well, are much less stable and are destroyed much more easily. They are present in greater abundances in the cosmic rays ($\approx 10^{-5}$) than they are in the interstellar medium ($\approx 10^{-2}$). This aspect can be attributed to spallation reactions between the four species considered, providing an independent check of the spallation models.

Another important information which can be obtained from the isotopic abundances regards the propagation or confinement time of cosmic rays in the Galaxy, which is the time that a cosmic ray spends in the Galaxy before escaping from it.

Some of the species created in spallation reactions are radioactive and hence they should decay before reaching the Solar System. However, if their decay time is comparable to the propagation time, an appreciable fraction of these isotopes will survive. The comparison of their abundance with respect to the stable isotopes

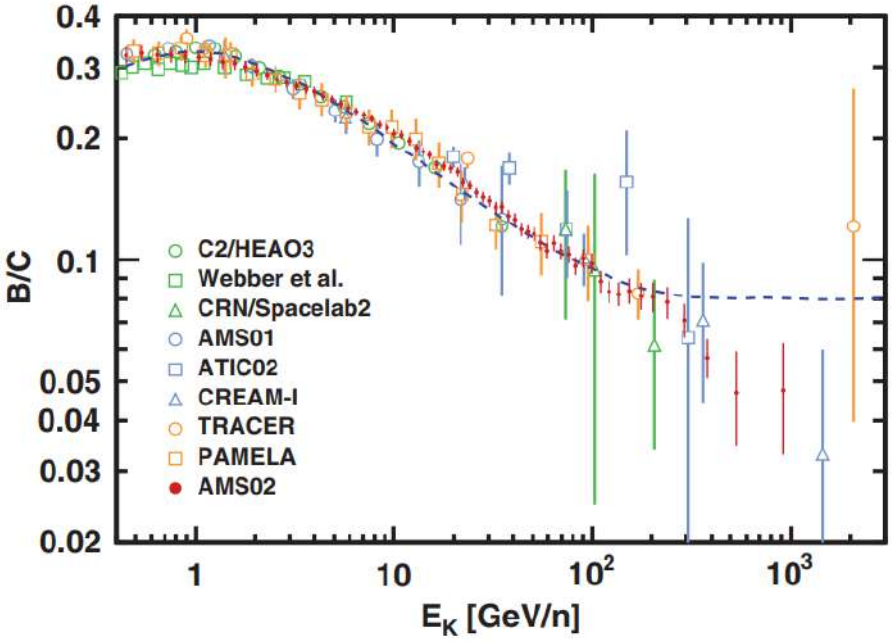

FIGURE 1.6: Boron-to-carbon ratio as a function of kinetic energy per nucleon as measured by different experiments. The figure is taken from AMS-02 measurements [7].

gives information about how much time the unstable nucleus has spent in the Galaxy, giving an estimate of the propagation time. One of the most famous of these *cosmic ray clocks* is the isotope ^{10}Be, which has a radioactive half-life of $1.5 \cdot 10^6$ years. Detailed calculations of the radioactive to stable isotopes ratio for different species give a unique confinement time of (15 ± 1.6) Myr. Also in this case, the diffusion-loss equation of cosmic rays, gives a formal explanation of this mechanism.

A third aspect that can be analysed thanks to relative abundances is the energy dependence of this confinement time. It has been observed that, for energy above 1 GeV, the chemical composition of cosmic rays decreases with increasing energy with a power-law relation $E^{-0.4}$.

Figure 1.6 shows the measurements of the boron-to-carbon ratio as a function of the kinetic energy of the particle, which is proportional to the escape path length and to the escape time of the heavier species (boron in this case). Therefore:

$$\tau(E) \propto E^{-\delta}, \tag{1.7}$$

with $\delta \approx 0.3 - 0.4$ according to the most recent measurements [7, 8]. As a consequence, the diffusion coefficient which appears in the diffusion-loss equation depends also on energy, being $D(E) \sim 1/\tau(E) \sim E^{\delta}$. The diffusion-loss equation gives again a description of this process.

1.3.3 Leptonic component

The leptonic component of cosmic rays is made essentially of electrons and positrons. The spectrum of electrons and positrons incident at the top of the atmosphere is expected to steepen by one power of E at an energy of ≈ 5 GeV because of strong radiative energy loss effects in the Galaxy.

Figure 1.7 shows the electron plus positron spectrum multiplied by a factor E^3 measured by different experiments, confirming an overall trend of E^{-3}. Some deviation from this spectrum are evident from the ATIC experiment, which measured an excess of electrons over propagation model expectations at energies of 300-800 GeV. The *Fermi*-LAT experiment measured a not-entirely flat spectrum without confirming the peak of the ATIC excess at 600 GeV. The HESS imaging atmospheric Cherenkov array also measured the electron flux above 400 GeV, finding indications of a cutoff above 1 TeV, but no evidence for a pronounced peak. The most recent measurements by the experiments *Fermi*-LAT and AMS-02 are reported in [9–11].

Figure 1.8 shows the positron fraction, defined as the ratio of positron flux divided by the electron plus positron flux, as measured by the PAMELA and AMS-02 satellite experiments. These experiments have a magnetic spectrometer which allows the charge discrimination. The measurements show an increase of the positron fraction above 10 GeV instead of the expected decrease from propagation models (heavy black line in the plot), confirming earlier hints seen by the HEAT balloon-borne experiment.

The structure in the electron spectrum, as well as the increase in the positron fraction, may be related to contributions from individual nearby sources (Supernova remnants or pulsars) emerging above a background suppressed at high energy by synchrotron losses. Other explanations have invoked propagation effects or dark matter decay/annihilation processes. The significant disagreement in the ratio

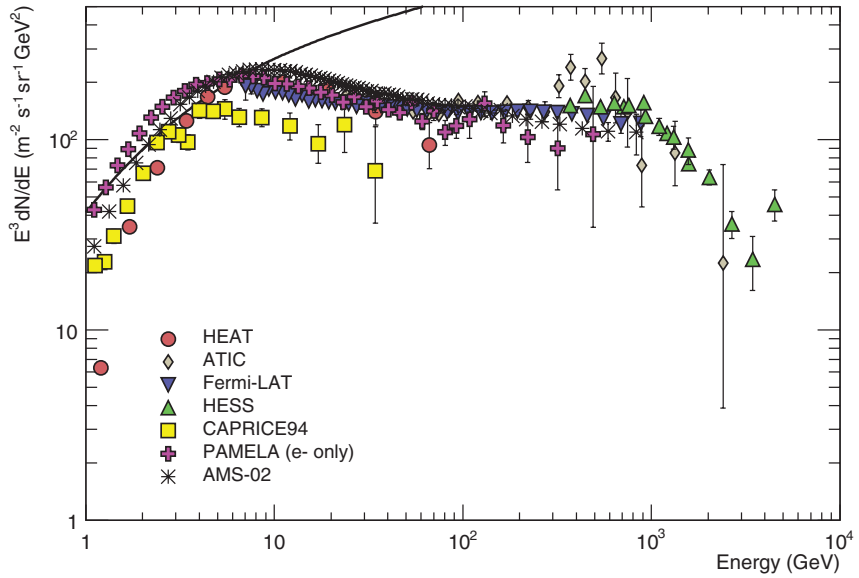

FIGURE 1.7: Differential spectrum of electrons plus positrons (except PAMELA data, which are electrons only) multiplied by E^3. The line shows the proton spectrum multiplied by 0.01. [5]

below 10 GeV is attributable to differences in charge-sign dependent solar modulation effects present near the Earth at the time of the measurements.

1.4 Diffusion mechanisms in the Galaxy

The interaction of charged particles with the interstellar medium (scattering with target gas and interaction with magnetic field) results in a diffusive motion of particles, which can be described by a diffusion equation.

For a species i of cosmic rays the equation can be written as follows: [12]

$$\begin{aligned}\frac{\partial N_i}{\partial t} &= \nabla \cdot (D_i \nabla N_i) - \frac{\partial}{\partial E}[b_i N_i(E)] - \nabla \cdot \mathbf{u} N_i(E) + \\ &+ Q_i - a_i N_i + \frac{v\rho}{m} \sum_{k>i} \int \frac{d\sigma(E, E')}{dE} N_k(E') dE',\end{aligned} \tag{1.8}$$

where $N_i(E, \mathbf{x}, t)dE$ represents the density of particles of species i at position $\mathbf{x}$, at time t, with energy between E and $E + dE$.

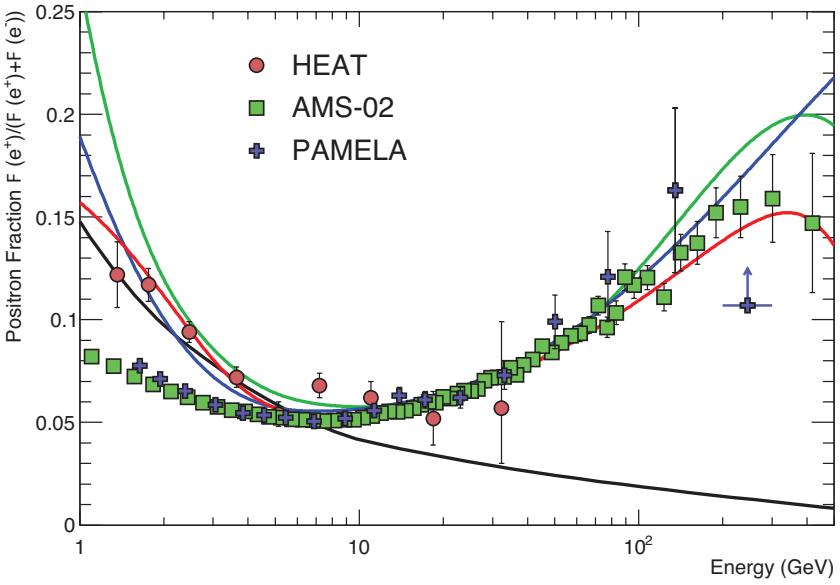

FIGURE 1.8: Positron fraction measured by different experiments. Latest measurements are taken by the experiments AMS-02 and PAMELA. The heavy black line is a model of pure secondary production and the three thin lines show three representative attempts to model the positron excess with different phenomena. Green: dark matter decay; blue: propagation physics; red: production in pulsars. [5]

The first term in the right side of the equation (1.8) represents the diffusion of cosmic rays. D is the diffusion coefficient and can be expressed in the form

$$D = \frac{1}{3}\lambda_D v, \tag{1.9}$$

where λ_D is the diffusion mean free path and v if the particle velocity. The second term represents the energy loss (for example for synchrotron emission). The coefficient $b(E)$ has different expressions according to the type of process considered. The third term represents the convection process at velocity $\mathbf{u}$. The fourth term $Q_i(, \mathbf{x}, t)dE$ is the source term and represents the number of particles of species i per cm^3 injected at position $\mathbf{x}$ and time t with energy between E and $E + dE$. Finally, the last two terms represent the loss rate and production rate of species i, respectively. The coefficient a_i includes all the loss contributions, such as the escaping time and the spallation losses. The last term includes the production rate for species i deriving from the spallation of all heavier species.

There is no analytical solution for this equation in the general case. Simulation codes such as GALPROP [13] and DRAGON [14] have been developed to solve

numerically the diffusion equation. These codes can predict the CR distribution and spectrum in the Galaxy, once some assumptions are made about both the CR sources and the CR diffusion parameters.

1.4.1 Spallation mechanism

The diffusion-loss equation gives information about the expected rates of particles due to the spallation mechanism. A simplified version of the equation (1.8) can be considered (see [15]), neglecting the diffusion and energy loss terms. Furthermore, if the rate equation for species which are not injected at the source, such as the light elements lithium, beryllium and boron, is considered, the source term Q_i can also be neglected. The equation obtained is:

$$\frac{\partial N_i}{\partial t} = -\frac{N_i}{\tau_i} + \sum_{k>i} \frac{P_{ki}}{\tau_k} N_k, \tag{1.10}$$

where τ_i is the spallation lifetime for species i and P_{ki} is the probability that a nucleus of species i is created in an inelastic collision involving the destruction of a nucleus k.

This equation can be re-written in terms of the path length $\xi = \rho x = \rho v t$ (measured in g cm^{-2}), where ρ is the gas density and v is the particle velocity:

$$\frac{\partial N_i(\xi)}{\partial \xi} = -\frac{N_i(\xi)}{\xi_i} + \sum_{k>i} \frac{P_{ki}}{\xi_k} N_k(\xi). \tag{1.11}$$

In order to perform a simplified calculation, the rate equation for a heavy and a light species is considered, including in the heavy species the elements that are fragmented by spallation (for example the *medium* o M group of elements carbon, nitrogen and oxygen) and in the light species the ones that are generated as a result of the spallation process (the *light* o L group of elements lithium, beryllium and boron). Initially, there are no particles in the L group at $\xi = 0$. The differential equations to describe the L and M groups are:

$$\frac{dN_M(\xi)}{d\xi} = -\frac{N_M(\xi)}{\xi_M}, \tag{1.12}$$

$$\frac{dN_L(\xi)}{d\xi} = -\frac{N_L(\xi)}{\xi_L} + \frac{P_{ML}}{\xi_M} N_M(\xi). \tag{1.13}$$

Integrating equation (1.12),

$$N_M(\xi) = N_M(0)\exp(-\xi/\xi_M). \tag{1.14}$$

Multiplying equation (1.13) by the factor $\exp(\xi/\xi_L)$ and integrating:

$$\frac{d}{d\xi}[\exp(\xi/\xi_L)N_L(\xi)] = \frac{P_{ML}}{\xi_M}\exp(\xi/\xi_L - \xi/\xi_M)N_M(0), \tag{1.15}$$

$$\frac{N_L(\xi)}{N_M(\xi)} = \frac{P_{ML}\xi_L}{\xi_L - \xi_M}\left[\exp(\xi/\xi_L - \xi/\xi_M) - 1\right]. \tag{1.16}$$

In this simplified treatment, average values of ξ_L, ξ_M and P_{ML} are adopted (see Table 10.1a in [15]). From the inelastic cross-sections for the M elements, the value of P_{ML} is found to be 0.28, while $\xi_M = 6$ g cm^{-2} and $\xi_L = 8.4$ g cm^{-2}. From the relative abundances measurements in cosmic rays, $\frac{N_L(\xi)}{N_M(\xi)} = 0.25$. Inserting these values into (1.16), the typical path length through which the M elements would have to pass to create the observed abundance ratio of the L to M elements is $\xi = 4.8$ g cm^{-2}, of the same order of magnitude as the mean free path of the M elements, which is hardly surprising.

The same type of calculation can be performed for the production of ^{3}He by the spallation of ^{4}He in the interstellar gas.

There are obviously some discrepancies with experimental data, coming from the fact that this is a simplified model. These discrepancies can be removed if a distribution of path lengths is considered instead of assuming that all the high energy particles traverse the same amount of matter in reaching the Earth. In this case the complete diffusion-loss equation must be considered.

1.4.2 Cosmic ray *clocks*: the case of ^{10}Be

The radioactive species created in spallation reactions can be used to date the samples of cosmic rays observed near the Earth.

The most famous example of these *clocks* is the radioactive isotope of beryllium ^{10}Be, which has a life-time τ_r of the same order of magnitude as the cosmic ray escape time τ_e. From spallation reactions, the expected fraction of the ^{10}Be with respect to its stable isotopes ^{7}Be and ^{9}Be is about 10%. If the escape time τ_e is

much longer than τ_r, this fraction should be much less than 10% and should be of the order of τ_r/τ_e.

This statement can be derived using the simplified version of the diffusion-loss equation (1.10). In this case, a loss term for the propagation time $-N_i/\tau_e$ must be added in the equation.

Defining the production rate of species i as

$$C_i = \sum_{k>i} \frac{P_{ki}}{\tau_k} N_k \tag{1.17}$$

and considering the steady state solution of the equation ($dN_i/dt = 0$), the equation becomes:

$$-\frac{N_i}{\tau_e(i)} + C_i - \frac{N_i}{\tau_{spal}(i)} = 0 \Rightarrow N_i = \frac{C_i}{\frac{1}{\tau_e(i)} + \frac{1}{\tau_{spal}(i)}}. \tag{1.18}$$

For the radioactive isotope, a decay loss term must be included $-N_i/\tau_r$, where τ_r is the characteristic decay time:

$$-\frac{N_i}{\tau_e(i)} + C_i - \frac{N_i}{\tau_{spal}(i)} - \frac{N_i}{\tau_r(i)} = 0 \Rightarrow N_i = \frac{C_i}{\frac{1}{\tau_e(i)} + \frac{1}{\tau_{spal}(i)} + \frac{1}{\tau_r(i)}}. \tag{1.19}$$

So, the steady state ratio of the ^{10}Be to ^{7}Be isotopes is:

$$\frac{N(^{10}Be)}{N(^{7}Be)} = \frac{\frac{1}{\tau_e(^{7}Be)} + \frac{1}{\tau_{spal}(^{7}Be)}}{\frac{1}{\tau_e(^{10}Be)} + \frac{1}{\tau_{spal}(^{10}Be)} + \frac{1}{\tau_r(^{10}Be)}} \frac{C(^{10}Be)}{C(^{7}Be)}. \tag{1.20}$$

If the time-scale for the destruction of the beryllium isotopes by spallation is much greater than their escape times $\tau_{spal} \gg \tau_e$, a simpler expression is obtained:

$$\frac{N(^{10}Be)}{N(^{7}Be)} = \frac{\frac{1}{\tau_e(^{7}Be)}}{\frac{1}{\tau_e(^{10}Be)} + \frac{1}{\tau_r(^{10}Be)}} \frac{C(^{10}Be)}{C(^{7}Be)}. \tag{1.21}$$

Measurements of this ratio lead to an escape time of 10 Myr.

1.4.3 Confinement time and B/C ratio

As discussed is section 1.3.2, the boron-to-carbon ratio decreases with increasing energy.

The simplest interpretation of the energy dependence of secondary to primary ratio is that the path length of the primary particles through interstellar gas changes with energy. Suppose that $\xi_e(E) = \xi_0(E/E_0)^{-\alpha}$, being α a positive number to obtain the requested trend of the path length.

Starting from equations (1.12) and (1.13), including a loss term of the form $-N_L/\xi_e(E)$ in equation (1.13) and considering the steady state solution for this equation ($dN_L/dt = 0$), one obtains:

$$-\frac{N_L}{\xi_e(E)} + \frac{P_{ML}}{\xi_M} N_M - \frac{N_L}{\xi_L} = 0. \tag{1.22}$$

In the high energy limit, the escape path length is much less than the spallation path length, $\xi_e \ll \xi_L$, and the solution of equation (1.22) becomes

$$\frac{N_L(\xi)}{N_M(\xi)} = P_{ML} \frac{\xi_e(E)}{\xi_M}. \tag{1.23}$$

Since P_{ML} and ξ_M are independent on energy, the energy dependence of the ratio of secondary to primary particles is the same as the one of the escape path length $\xi_e(E)$ and of the escape time τ_e, which is proportional to $\xi_e(E)$. Hence, the measurements of the boron-to-carbon ratio shown in figure 1.6 are a direct evidence of the decrease of the escape time with increasing energy.

1.4.4 Confinement volume for cosmic rays: the *leaky box* model

The value of the confinement time found with the previous considerations is not compatible with a free propagation of the relativistic particles in the Galaxy. If the confinement volume had dimension of 10 kpc (order of magnitude of the dimension of the Galactic disk) and if relativistic particles propagate at velocity close to that of light, they would escape from the Galaxy in about $3 \cdot 10^4$ years. Furthermore, their distribution on the sky would be highly anisotropic, since most of the flux

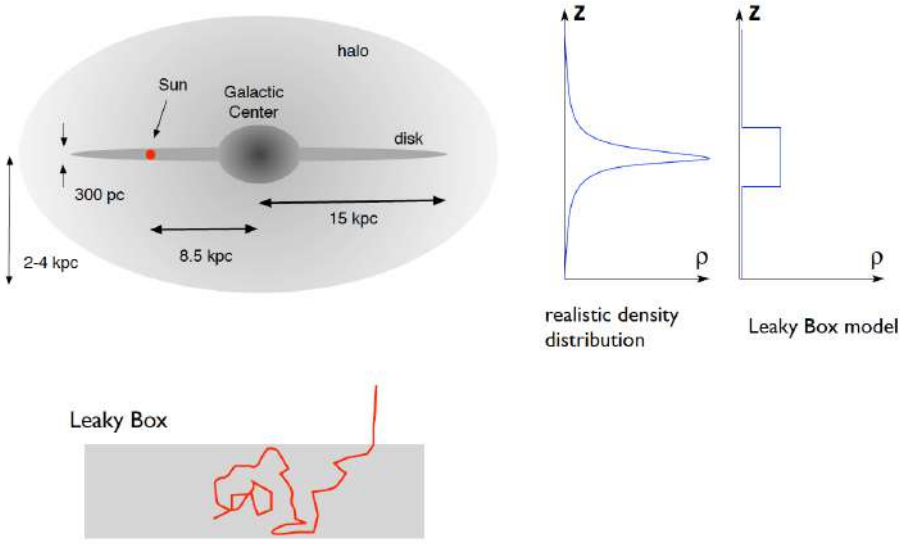

FIGURE 1.9: *Leaky box* propagation model compared to a more realistic distribution of CRs. In the *leaky box* model the number of particles escaping from the box is proportional to the number of particles in the box.

would come from the center of the Galaxy, in contrast with the observed isotropy of cosmic rays. In fact, a small degree of anisotropy is observed ($\approx 10^{-3}$), but it is compatible with the anisotropy resulting from the diffusive motion of cosmic rays [16]. Anisotropy is also searched in UHECR, which are much less confined in the Galaxy and should have an extragalactic origin. Hints of a small degree of anisotropy is observed at very high energies (EeV) by the Pierre Auger and the Telescope Array Observatories and a possible association of these cosmic rays with the extragalactic sources is under investigation (see [17] for a review).

For this reason, cosmic rays are supposed to be confined in the Galaxy in a certain volume by the galactic magnetic field ($B \approx 2\mu$G). A hint of this aspect comes from the fact that the values of the energy densities of the magnetic field ($\rho_B = B^2/2\mu_0 \approx 0.2$ eV cm^{-3}) and cosmic rays ($\rho_{CR} \approx 1$ eV cm^{-3}) are of the same order of magnitude, suggesting that the two components are related to each other.

The confinement of cosmic rays in the Galaxy is often described by the *leaky box* model. Particles are supposed to freely propagate in a box with a horizontal dimension equal to the diameter of the Galactic disk (≈ 30 kpc) and a height h of 3-5 kpc (see figure 1.9) and be reflected by the boundaries of this box. At each reflection, the particle will have a constant probability of escaping from the Galaxy $\tau_e^{-1} \ll c/h$. The diffusion term in equation (1.8) is replaced by a loss term $-N_i/\tau_e$. Neglecting collision processes and convection, the solution of the

equation for a source term $Q(E,t) = N_0(E)\delta(t)$ is:

$$N(E,t) = N_0(E)\exp(-t/\tau_e). \tag{1.24}$$

In this picture, τ_e can be interpreted as the average time that a cosmic ray spends in the confinement volume.

If a steady source term $Q_i(E)$ is considered for the species i and including only a loss term due to interaction with the interstellar gas, equation (1.8) becomes:

$$\frac{\partial N_i}{\partial t} = -\frac{N_i}{\tau_e} + Q_i - \frac{N_i}{\tau_i}. \tag{1.25}$$

The steady-state solution of this equation ($\frac{\partial N_i}{\partial t} = 0$) is:

$$N_i(E) = \frac{Q_i(E)\tau_e}{1+\tau_e/\tau_i}. \tag{1.26}$$

For protons, it is observed that $\tau_e \ll \tau_i$ for all energies and equation (1.26) reduces to

$$N(E) = Q(E)\tau_e(E). \tag{1.27}$$

From cosmic ray measurements we know that both $N(E)$ and $\tau_e(E)$ have a power-law dependence on energy with spectral index -2.7 and -0.4 respectively. As a result, also the source spectrum $Q(E)$ must follow a power-law shape:

$$Q(E) \propto E^{-\alpha}, \tag{1.28}$$

where the spectral index α is approximately 2.3.

In conclusion, in order to reproduce the observed spectrum, cosmic ray sources must accelerate particles up to very high energies and produce a power-law spectrum with spectral index slightly softer (i.e. larger value of α) than 2.

1.5 Non-thermal photon emission processes

During their propagation from the source to the Earth, CRs are deflected by the Galactic magnetic field, leading to an almost isotropic distribution of CRs. For

this reason, CR measurements at the Earth cannot give direct information about the CR spectra in different parts of the Galaxy. As already said, the study and simulation of diffusion processes allow the calculation of the CR spectrum at the Earth, with some assumptions on the CR sources and the propagation parameters.

The only way to directly trace CRs in the Galaxy is the observation of non-thermal photons produced by these accelerated particles with the environment they are propagating into. This aspect is true both for the study of the CRs propagating in the Galaxy and of CRs produced at their source.

The main non-thermal emission mechanisms are:

- synchrotron emission, due to high energy electrons deflected in the magnetic field;
- inverse Compton scattering of high energy electrons on low energy photons from the Cosmic Microwave Background (CMB), from infrared dust emission and from starlight;
- bremsstrahlung radiation of high energy electrons accelerated in the Coulomb field generated by charged particles (electrons, protons and ions) of the gas in the emitting region;
- decay of neutral resonances, produced in the interaction of high energy protons with target protons and ions present in the gas.

The first one produces spectra from the radio to the X-ray band. The other three processes contribute mostly in the γ-ray energy band from few MeV to hundreds of TeV and are of the most interesting for the scope of this work. Nevertheless, synchrotron emission is often important to model radio to X-ray data in a multiwavelength picture.

The study of the cross sections of these processes allows a prediction of the observed photon flux for a given spectrum of the accelerated particles. In the simplest case, this spectrum is described by a simple power-law.

In the following sections, a description of the emission processes will be given, and the specific photon emissivity Q_γ (number of photons emitted per unit volume in unit time per unit energy) will be calculated for each process. In order to evaluate the photon flux at the Earth, the emissivity must be multiplied by the volume

of the emitting region and divided by $4\pi d^2$, where d is the distance of the region considered:

$$F_\gamma = Q_\gamma \frac{V}{4\pi d^2}. \tag{1.29}$$

1.5.1 Synchrotron emission

The synchrotron emission occurs when electrons are deflected by a magnetic field. The spectrum of the emitted photons goes from the radio to the X-ray energy band, according to the strength of the magnetic field and to the electron energy.

The power emitted by a relativistic particle of charge e and Lorentz factor γ with an acceleration $\vec{a}$ is given by the generalized Larmor formula:

$$P_e = \frac{2e^2}{3c^3}\gamma^4 \left[\gamma^2 a_\parallel^2 + a_\perp^2\right], \tag{1.30}$$

where $a_\parallel$ and $a_\perp$ are the components of $\vec{a}$ parallel and perpendicular to the direction of motion respectively,

Since there is no electric field acting on the particle and neglecting any other force in the direction of motion ($a_\parallel = 0$), the acceleration is given by the relativistic Lorentz force:

$$\vec{F} = \frac{d}{dt}(\gamma m \vec{v}) = \frac{e}{c}\vec{v} \times \vec{B} \tag{1.31}$$

which implies:

$$F_\perp = \gamma m a_\perp = e\frac{v_\perp}{c}B \Rightarrow a_\perp = \frac{e v_\perp B}{\gamma m c} \tag{1.32}$$

The resulting trajectory will have an helical shape, with a typical radius (Larmor radius) obtained by setting $a_\perp = v_\perp^2/r_L$ and a corresponding relativistic gyration frequency given by $\nu_B = v_\perp/(2\pi r_L)$:

$$r_L = \frac{v_\perp^2}{a_\perp} = \frac{\gamma m c v_\perp}{eB} \tag{1.33}$$

$$\nu_B = \frac{eB}{2\pi\gamma m c} = \frac{\nu_L}{\gamma} \tag{1.34}$$

where ν_L is the Larmor frequency, i.e. the gyration frequency for non-relativistic particles.

However, the typical frequency of the synchrotron emission does not correspond to the revolution frequency of the particles. Since electrons are relativistic, in the laboratory frame of reference the emission is collimated in a cone of angular aperture of $\approx 2/\gamma$ degrees. Hence photons are emitted in the direction of the observer only for a small fraction of time and the observed period of the rotation of the electron must be multiplied by the factor $2/\gamma$. Furthermore, due to the relativistic nature of the electrons, the time intervals are compressed of a factor $(1-\beta) \approx 1/(2\gamma^2)$. In the end, the typical synchrotron frequency will be multiplied by a factor $(\gamma/2)(2\gamma^2) = \gamma^3$:

$$\nu_s = \gamma^3 \nu_B = \gamma^2 \nu_L = \gamma^2 \frac{eB}{2\pi mc} \tag{1.35}$$

This is the frequency at which the maximum power emission is expected.

The detailed calculation shows that the power emission formula from a single electron in a magnetic field B is given by [18]:

$$\begin{aligned} P_e(\nu, \gamma, \theta) &= \frac{\sqrt{3} e^3 B \sin\theta}{2\pi mc^2} F(\nu/\nu_c) \\ F(x) &= x \int_x^\infty K_{5/3}(y) dy \\ \nu_c &= \frac{3}{2} \nu_s \sin\theta \end{aligned} \tag{1.36}$$

where θ is the angle that the velocity of the electron forms with the magnetic field (*pitch* angle) and $K_{5/3}(y)$ is the modified Bessel function of order 5/3.

Assuming an electron density $n(\gamma, \theta)$, where $n(\gamma, \theta) d\gamma d\theta$ is the number of electrons per unit volume with Lorentz factor between γ and $\gamma + d\gamma$ and pitch angle between θ and $\theta + d\theta$, the power emitted per unit volume and unit frequency is:

$$\epsilon_s(\nu) = \int d\gamma \int d\Omega n(\gamma, \theta) P_e(\nu, \gamma, \theta). \tag{1.37}$$

In case of an isotropic emission, the electron density becomes $n(\gamma, \theta) = n(\gamma)/4\pi$. Hence, substituting the previous equations and recalling that the particle density is related to the differential flux (number of particles crossing a unit area in a unit

time and per unit solid angle) through the relation $dN/d\gamma = n(\gamma)\beta c/4\pi$:

$$\begin{aligned}\epsilon_s(\nu) &= \frac{\sqrt{3}e^3 B}{2\pi mc^2}\int d\gamma \frac{n(\gamma)}{4\pi} 2\pi \int d\theta \sin^2\theta F(\nu/\nu_c) = \\ &= \frac{\sqrt{3}e^3 B}{4\pi mc^2}\int d\gamma \frac{4\pi}{\beta c}\frac{dN}{d\gamma}\int d\theta \sin^2\theta F(\nu/\nu_c) = \\ &= \frac{\sqrt{3}e^3 B}{2\pi mc^2}\int d\gamma \frac{4\pi}{\beta c}\frac{dN}{d\gamma} R(\nu/\nu_c),\end{aligned} \tag{1.38}$$

where

$$R(x) = \frac{1}{2}\int d\theta \sin^2\theta F(x). \tag{1.39}$$

The total emissivity is obtained by integrating over the solid angle, i.e. by multiplying by 4π:

$$Q_\gamma = 4\pi\epsilon_s.^1 \tag{1.40}$$

An important characteristic of the resulting emissivity is that a power law electron distribution produces a power law emissivity spectrum and the two spectral indices are related. If α is the spectral index of the radiation and s the one of the injection, it can be demonstrated (see Appendix A) that

$$\alpha = \frac{s-1}{2}. \tag{1.41}$$

The synchrotron emission contributes to the radio to X-ray energy range, depending on the maximum of the electron population.

1.5.2 Inverse Compton scattering

Inverse Compton scattering consists of the interaction of a high energy electron with a low energy photon; the electron transfers part of its energy to the seed photon, creating a γ-ray. If γ is the Lorentz factor of the relativistic electron ($\gamma \gg 1$) and ϵ_0 is the energy of the seed photon in the laboratory system, the energy of the photon in the rest frame of the electron becomes:

$$\epsilon = \epsilon_0\gamma\left(1 + \beta\cos\theta\right), \tag{1.42}$$

[1]The notation Q_γ in this case is not completely appropriate, since the synchrotron emission does not produce γ-rays, but we still adopt it in conformity with the other processes.

where θ is the angle between the photon and the electron direction in the laboratory system and $\beta = v/c$.

In scattering off the electron in the rest frame of the electron, the photon goes off at an energy ϵ' and scattering angle Θ'. The energy ϵ' after scattering is given by:

$$\epsilon' = \frac{\epsilon}{1 + (\epsilon/mc^2)(1 - \cos\Theta')}. \tag{1.43}$$

Now, in the Thomson limit ($\epsilon \ll mc^2$), $\epsilon' \approx \epsilon$. Going back to the laboratory system an equation similar to (1.42) holds. Then, taking into account that the two angular factors (one per each Lorentz transformation) at most are equal to 2, the maximum photon energy is approximately $\epsilon_1 \approx 4\gamma^2\epsilon_0$. Considering the typical energy of the CMB, the IC contributes mostly to the γ-ray energy range, with a peaked spectrum characterised by a maximum photon energy depending on the maximum energy of the electrons.

The cross-section of the process can be calculated using Feynman diagrams (see figure 1.10). The result is given by the Klein-Nishina formula [18]:

$$\begin{aligned} \sigma_{\mathrm{KN}}(\gamma, \omega_0, \omega) &= \frac{2\pi r_0^2}{\omega_0 \gamma^2}\left[1 + q - 2q^2 + 2q\ln(q) + \frac{\Gamma^2 q^2(1-q)}{2(1+\Gamma q)}\right], \\ q &= \frac{\omega}{4\omega_0\gamma(\gamma - \omega)}, \end{aligned} \tag{1.44}$$

$$\tag{1.45}$$

where $\Gamma = 4\omega_0\gamma$ and $\omega = h\nu/(mc^2)$; ω_0 is the corresponding quantity for the seed photon.

In the general case, seed photons are not monochromatic, but they are described by a density $n(\omega_0)$. For this reason, the previous cross-section must be integrated over all possible seed photons and all possible electrons, whose density is given by the injection spectrum:

$$Q_\gamma(\omega) = 4\pi \int d\omega_0 \int d\gamma \frac{dN_e(\gamma)}{d\gamma} n(\omega_0)\sigma_{\mathrm{KN}}(\gamma, \omega_0, \omega). \tag{1.46}$$

FIGURE 1.10: Feynman diagrams for Inverse Compton Scattering.

1.5.3 Bremsstrahlung radiation

When an electron interacts with the Coulomb field generated by charged particles, it radiates photons up to the γ-ray energy band. The process is described in Quantum Electrodynamics by the Feynman diagrams in figure 1.11. Only the relevant diagrams have been considered, which are the ones where a high energy electron radiates a hard photon.

Bremsstrahlung of high energy electrons on target protons, electrons and helium nuclei can be considered. The cross-section of the process is given by the Bethe-Heitler formula for the electron-hadron interaction, while some relativistic corrections are needed for the electron-electron process [19]. In this case only the electron-proton contribution is taken into account. The Bethe-Heitler cross-section derived in Born approximation is:

$$\frac{d\sigma_{e-p}}{d\epsilon} = \frac{4r_0^2\alpha}{\epsilon}\left[1+\left(\frac{\gamma-\epsilon}{\gamma}\right)^2-\frac{2}{3}\frac{\gamma-\epsilon}{\gamma}\right]\left[\ln\left(\frac{2\gamma(\gamma-\epsilon}{\epsilon}\right)-\frac{1}{2}\right], \tag{1.47}$$

where r_0 is the classical radius of the electron, α is the fine structure constant, γ is the Lorentz factor of the relativistic electron and ϵ is the photon energy.

The total photon rate is obtained by integrating the cross-section with the electron injection spectrum. The target density is assumed to be constant, which means that the integration over target density is straightforward.

The final expression for the efficiency is:

$$Q_\gamma(\epsilon) = 4\pi n_H \int d\gamma \frac{dN_e(\gamma)}{d\gamma}\frac{d\sigma_{e-p}}{d\epsilon}, \tag{1.48}$$

where n_H is the target proton density, also called ambient density.

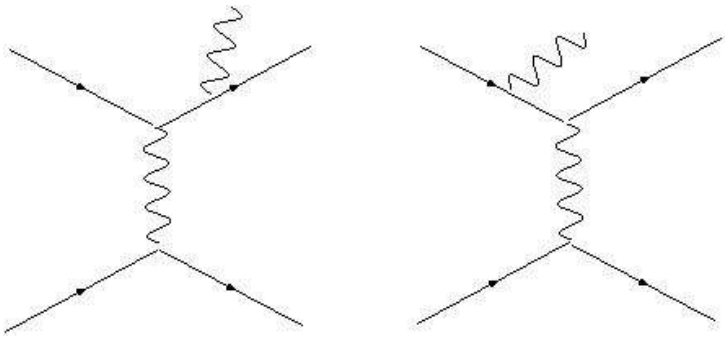

FIGURE 1.11: Feynman diagrams for bremsstrahlung.

1.5.4 Hadronic interaction

The interaction between high energy protons and target protons is more difficult to describe. This process involves the interactions between quarks, which need Quantum Chromodynamics. A small contribution comes also from the interaction of protons with target nuclei (mostly helium). In proton-proton inelastic scattering many particles are produced, among which neutral pions. Neutral pions π^0 decay almost immediately in 2 γ-rays (the mean life of a π^0 is $8.5 \cdot 10^{-17}$s), while charged pions $\pi^{\pm}$ decay in muons and neutrinos (with a mean life of $2.6 \cdot 10^{-8}$s):

$$p + p \rightarrow \pi + X,$$

$$\pi^0 \rightarrow \gamma + \gamma \quad (98.8\%)$$

$$\pi^+ \rightarrow \mu^+ + \nu_\mu \quad (99.9\%), \qquad \mu^+ \rightarrow e^+ + \nu_e + \bar{\nu}_\mu$$

$$\pi^- \rightarrow \mu^- + \bar{\nu}_\mu \quad (99.9\%), \qquad \mu^- \rightarrow e^- + \bar{\nu}_e + \nu_\mu$$

In this case, it is not possible to derive an analytical expression of the γ-ray production cross-section. Therefore, simulation codes or numerical parametrization are necessary to predict the photon flux.

Authors in [20] have provided a parametrisation of the pion production cross section from proton-proton inelastic scattering. This first attempt was then improved at momentum below 2 GeV/c in [21], by introducing the contribution of two baryonic resonances: $\Delta(1232)$, corresponding to the physical resonances of mass around 1232 MeV/c^2 and width of approximately 117 MeV/c^2, and res(1600), which includes the contribution of different resonances with mass around 1600 MeV/c^2.

In this model, the inclusive cross section for the pion production is divided in three contributions, one coming from the diffractive interaction, another from the non-diffractive interaction and the other from the two resonances. The total p-p cross section evaluated with this model is represented in figure 1.12 and compared to experimental cross sections, which are described by a by-eye-fit curve. In figure 1.13, the total inelastic cross section obtained from the model is compared to the empirical inelastic cross section, defined as the difference between the two by-eye best-fit curves of the experimental total and elastic cross sections.

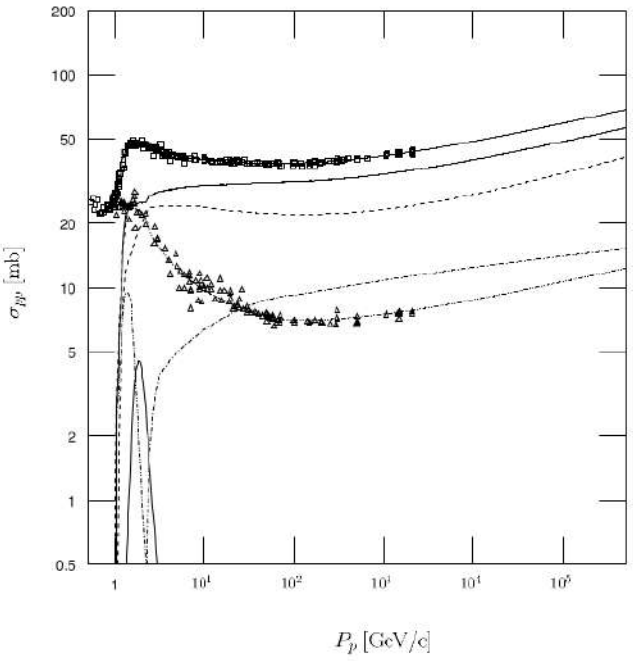

FIGURE 1.12: Experimental p-p cross sections, as a function of proton momentum, compared to the p-p cross section evaluated with the model described in [21]: experimental total (squares), experimental elastic (triangles), total inelastic (thick solid line), nondiffractive process (dashed line), diffractive process (dot-dashed line), $\Delta(1232)$ (dotted line), and res(1600) (thin solid line). The total inelastic is the sum of the four components. The thin solid and double-dot-dashed lines running through the two experimental data sets are by-eye fits to the total and elastic cross sections, respectively.

For each component, the inclusive cross sections for the production of secondary particles (γ-rays, $e^{\pm}$ and ν) are studied and parametrised independently. First, the secondary spectra were extracted generating events of monoenergetic protons. Then, these spectra were fitted with a common parametrised function. Finally, the parameters determined for monoenergetic protons were fitted as functions of proton energy, separately for each component. The functional formulae obtained often introduce tails extending beyond the energy-momentum conservation limits.

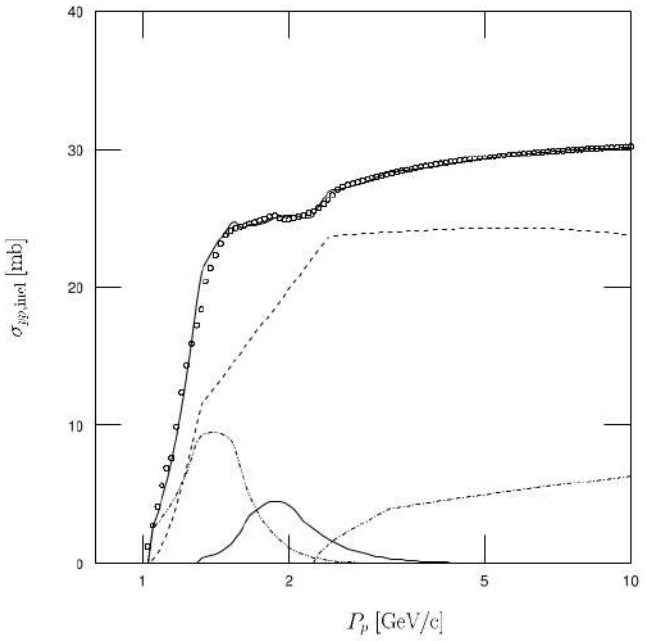

FIGURE 1.13: Empirical inelastic p-p cross sections (small circles), as a function of proton momentum, compared to the total inelastic p-p cross section evaluated with the model described in [21]. Lines are the same as in figure 1.12.

Hence, other functions were introduced to impose manually the kinematic limits. The total cross sections were obtained by summing the three contributions. The event generation was performed using some event simulators, such as Pythia 6.

Once the differential inclusive cross section for the γ-ray production $d\sigma(E)/d\ln(E)$ was parametrised, the γ-ray emissivity can be calculated:

$$Q_\gamma(E) = 4\pi n_H \int_{E_{p,th}} dE_p \frac{dN_p(E_p)}{dE_p} \frac{d\sigma(E|E_p)}{dE}, \tag{1.49}$$

where $E_{p,th}(E)$ is the minimum energy of the proton to be able to produce a γ-ray with energy E.

Figure 1.14 shows two examples of γ-ray spectra produced with this model, taken from [21], assuming a simple power-law for the proton spectrum with two different values of the spectral index. It can be noticed that the slope of the γ-ray spectrum is the same as the proton spectrum. A cut-off for energy below 100 MeV is observed in both cases, due to the threshold energy dictated by the mass of the π^0.

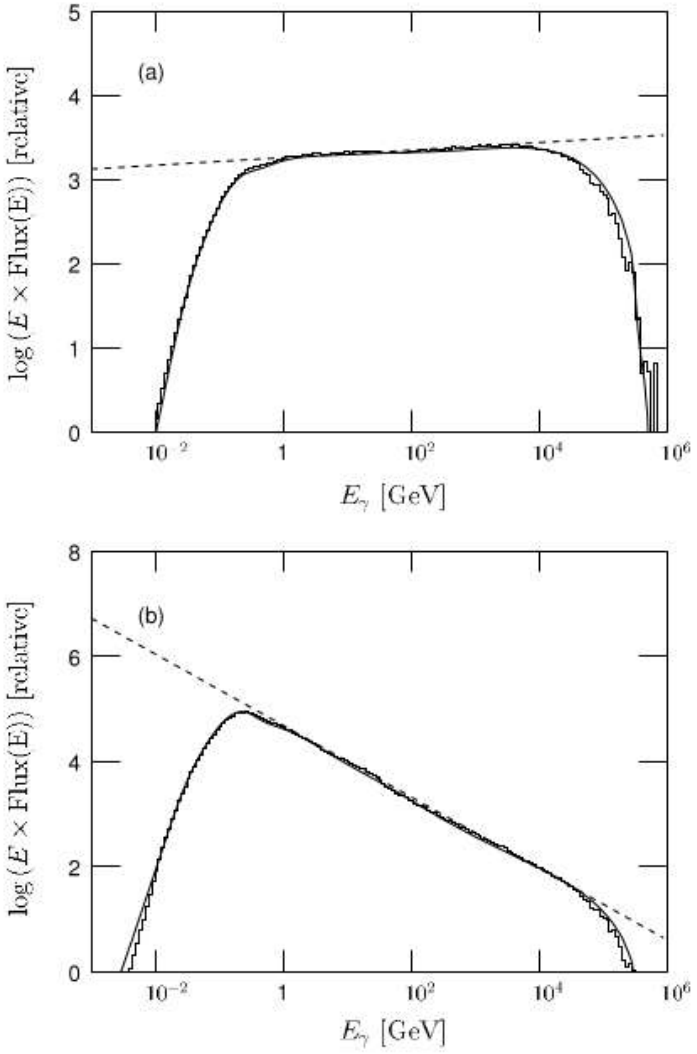

FIGURE 1.14: Gamma-ray spectra produced by protons with a power-law spectrum in kinetic energy with a cut-off at 512 TeV and an index of 2 in case (a) and 2.7 in case (b). Solid lines represent the model for the γ-ray production from π^0 decay. The dashed straight lines corresponds to a simple power-law with an index of 1.95 in case (a) and 2.68 in case (b). [21]

1.5.5 FLUKA

An alternative way to describe the hadronic interaction is provided by the code FLUKA [22], which is a general purpose Montecarlo code for simulation of particle interactions. In this code, hadronic interaction is modelled adopting different theoretical models describing the microscopic interactions between quarks and gluons, depending on the energy range under investigation. FLUKA allows the simulation of 60 different species of particles, including photons and electrons with energy from 1 keV to thousands of TeV, neutrinos, muons and hadrons (from

protons and neutrons to heavy ions) up to 20 TeV (which extends to 10 PeV when it is interfaced with the DPMJET code) and all corresponding antiparticles.

The results in [22] can be used to model the γ-ray emission deriving from the interaction of accelerated protons and helium with the protons and helium nuclei in the ISM, resulting in four possible interactions. Heavier elements can be neglected since their abundance is less than 0.1% of the total CR abundance. A kinetic energy from 0.1 keV/nucleon up to 10^5 GeV/nucleon in the laboratory frame of reference was assumed for each particle.

For each process the differential inclusive cross section is obtained as follows:

$$\frac{d\sigma(E|E_p)}{dE} = \sigma_{inel}(E_p) \times \frac{dn(E|E_p)}{dE}, \tag{1.50}$$

where E_p is the kinetic energy of the primary particle and E is the energy of the secondary photon. The term σ_{inel} represents the total inelatic cross section for the process considered, while dn/dE is the differential γ-ray multiplicity, i.e. the number of γ-rays produced in each interaction.

Figure 1.15 shows the differential inclusive cross sections for the four processes $p-p$, $p-{}^4He$, ${}^4He-p$ and ${}^4He-{}^4He$ as a function of the kinetic energy of the primary particle and of the energy of the secondary γ-ray. It can be noticed that all distributions peak at $E \sim 70$ MeV, which corresponds to half the mass of the neutral pion. This is expected, since the π^0 decay is the main process responsible for the γ-ray production and reflects in the γ-ray spectra, as already seen in figure 1.14.

Figure 1.16 shows the spectra of secondary particles produced by $p-p$ and ${}^4He-p$ interactions. A power-law distribution in momentum was assumed for high energy p and ${}^4He$ populations, with spectral index equal to 2.75 for protons and to 2.66 for Helium nuclei. The spectra are normalized to the target density n_{atoms}.

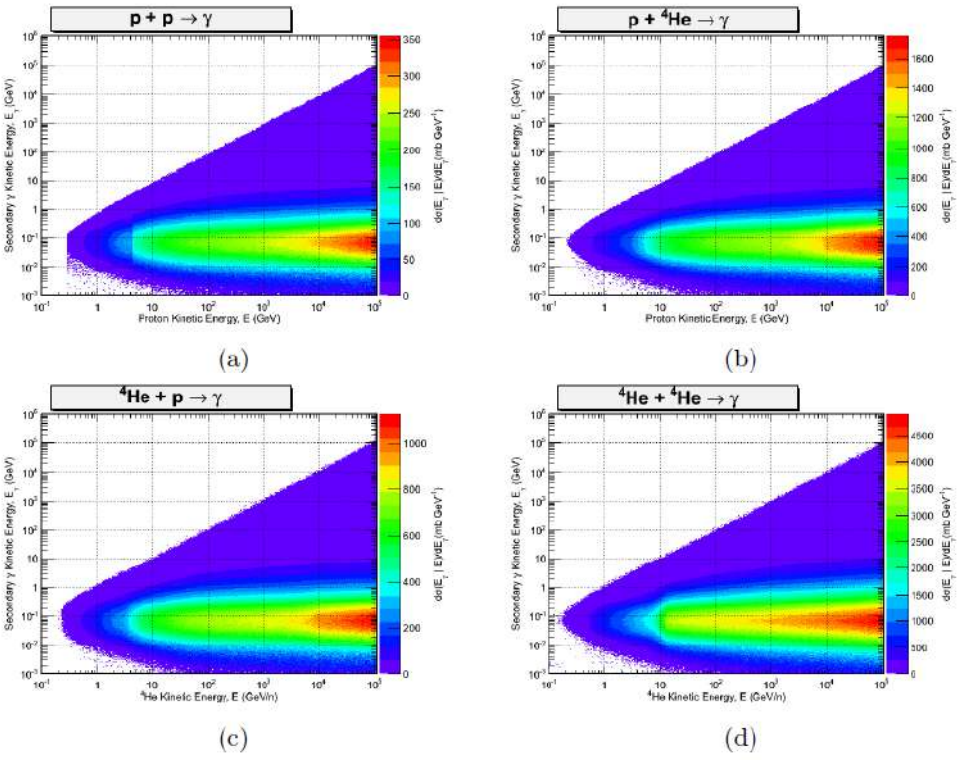

FIGURE 1.15: Differential inclusive cross sections for γ-ray production in $p-p$ (a), $p-^4He$ (b), ^4He-p (c) and $^4He-^4He$ (d) interactions [22].

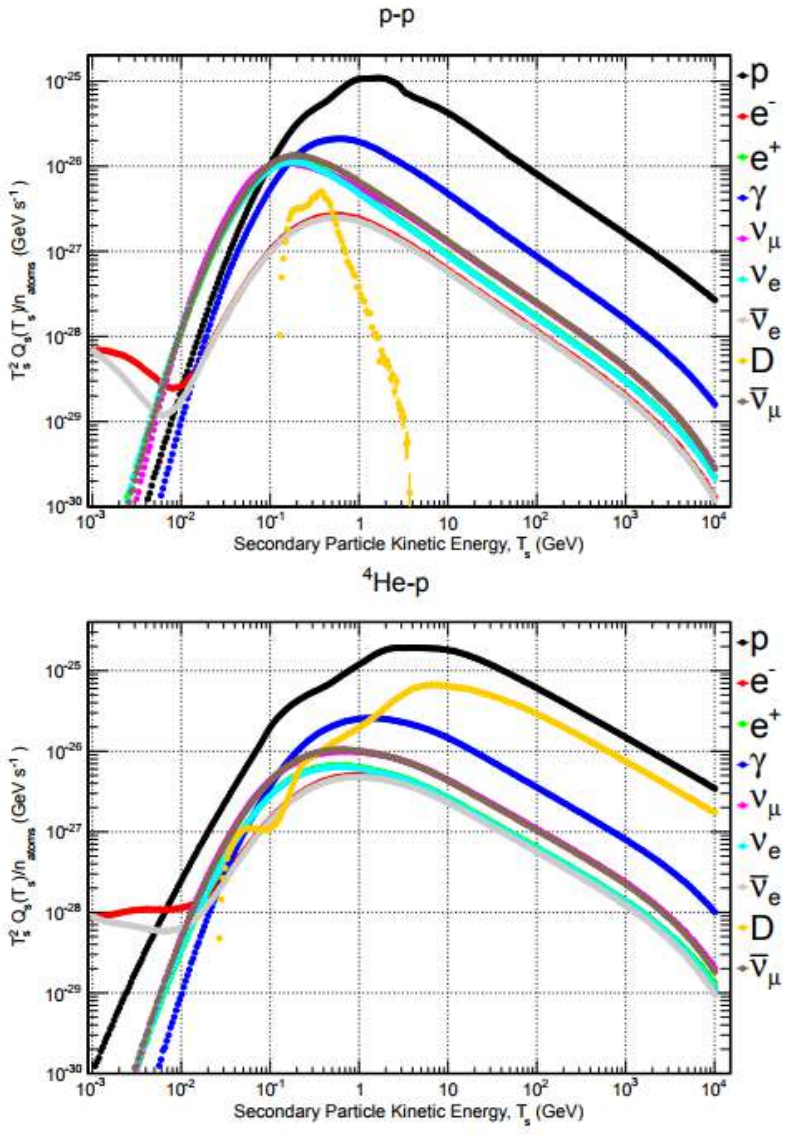

FIGURE 1.16: Spectra of secondary particles produced by $p-p$ (top) and ^4He-p (bottom) interactions, assuming a power-law distribution in momentum for p and ^4He populations, with spectral index equal to 2.75 for protons and to 2.66 for Helium nuclei. The spectra are normalized to the target density n_{atoms}. Secondary particles are: protons (black), electrons (red), positrons (green), γ-rays (blue), ν_e (cyan), $\bar{\nu}_e$ (grey), ν_μ (magenta), $\bar{\nu}_\mu$ (brown) and deuterons (orange) [22].

Chapter 2

Supernova Remnants: the sources of Galactic Cosmic Rays

2.1 Introduction

Supernova Remnants (SNRs) are strictly related to Cosmic Rays and are thought to be the main sources of the Galactic CRs. The diffusive shock acceleration theory predicts that a shock wave similar to the ones originating from a Supernova (SN) explosion can accelerate charged particles up to energies close to the "knee" of the CR spectrum, with a spectral shape compatible with the CR measurements. Furthermore, the expected number of SN explosion in our Galaxy is compatible with the CR energy density that we measure, as it will be shown later.

SNRs originate from the explosion of a sufficiently massive star, generating a shock wave which propagates in the interstellar medium. The expanding ejected material and the material shocked along the way constitute the Supernova Remnant.

Since supernovae are relatively rare (2-3 per century in a typical spiral galaxy like our own), SNRs also provide a good way to study the local population of supernovae and reveal details about the explosion mechanism that are difficult to obtain from studying supernovae directly.

2.2 Stellar evolution

The stellar evolution can be well described through the observation of the Hertzsprung-Russell (H-R) diagram, which represents the absolute magnitude[1] of a star versus its effective temperature, or equivalently its color or spectral type[2].

Most stars, after their formation, occupy a position in the so called *main sequence* of the H-R diagram and remain in that position for most of their life. This sequence includes stars from the upper left corner to the lower right corner of the diagram. This means that the higher the temperature, the higher the luminosity (or equivalently the lower the magnitude).

The position in the main sequence is mainly determined by the initial total mass of the star, which also affects its entire evolution. Massive stars have high luminosities and high temperatures (*blue* stars) and burn their fuel more rapidly than smaller, colder stars (*red* stars). At equilibrium the gravitational force of the mass of the star is balanced by the fusion reactions in the core of the star, which consist in the production of one helium nuclei from four protons. The fusion reaction can go through two possible cycles. The first one involves the production of hydrogen isotopes deuterium and tritium (pp cycle), while the second involves the production of carbon, nitrogen and oxygen nuclei (CNO cycle). In massive stars ($M > 5-8M_{\odot}$, being $M_{\odot}$ the mass of the Sun), when the hydrogen in the star core is not sufficient to balance the gravitational force any more, heavier elements are formed through nuclear fusion and the star expands (*red giant* stage) losing the outer layers of gas. The fusion processes end when the iron is synthesised, since the reactions of production of elements heavier than iron are not exothermic.

Finally, gravitational force prevails and the star collapses. If the final mass of the star is lower than the Chandrasekhar limit ($1.44M_{\odot}$), the degeneration pressure[3]

[1]The apparent magnitude is defined by the equation $m = m_0 - 2.5\log(L/L_0)$, where L is the luminosity of the star and m_0 and L_0 are the values of the magnitude and the luminosity of a reference star respectively. The absolute magnitude is defined as the magnitude that the star would have if its distance were 10 kpc. It must be noticed that, according to the definition of m, the higher the luminosity the lower the magnitude.

[2]Stars are classified according to their color, which corresponds to an average wavelength of the radiation emitted, and are divided in 7 spectral classes. Going from the lower (higher) temperature (wavelength) to the higher (lower), they are: M, K, G, F, A, B and O.

[3]The degeneration pressure is a quantum mechanical effect due to the Pauli exclusion principle. When fermions are compressed in a small space, their must occupy states with increasing energy, until electrons become relativistic, saturating the energy levels. The effect is that the compression cannot go further certain limits and a pressure is generated.

generated by the electrons balances the gravitational forces and the star becomes a *white dwarf*. If this condition is not satisfied, i.e. the final mass of the star exceeds the Chandrasekhar limit, the star will end its life as a Supernova. The electron degeneration pressure is not sufficient to balance the gravitational collapse and electrons and protons interact through the inverse beta decay, creating a hard core of neutrons. If the mass of the star is not too high ($M < 2.5M_{\odot}$), the degeneration pressure of neutrons will prevent the star from a further collapse and a *neutron star* will be formed. The collapsing star "bounces" on this hard neutron star and creates a shock wave that propagates far from the star (supernova explosion). For higher values of the mass of the star a black hole is created.

2.2.1 Supernovae

Supernovae are divided into two broad categories, depending on the explosion process: core collapse supernovae and thermonuclear supernovae. An old classification of supernovae, proposed by Minkowski in 1941, is based on the observed spectra: Type I supernovae do not show hydrogen absorption in their spectra, while Type II do. Type II supernovae are invariably core collapse supernovae, while Type I supernovae can be either core collapse or thermonuclear. The thermonuclear explosions are associated with spectroscopic class Type Ia, which have Si absorption lines in their spectra.

Core collapse supernovae mark the end of the lives of massive stars ($M > 8M_{\odot}$). In these stars different layers containing the products of the consecutive burning stages are expected, with heavier elements in the core. From the core to the outside one expects: iron-group elements in the core (silicon-burning products), then silicon-group elements (oxygen-burning products), oxygen (a neon burning product), neon and magnesium (carbon-burning products), carbon (a helium-burning product), helium (a hydrogen-burning product) and, finally, unprocessed hydrogen-rich material. The creation of the iron-group core, which lasts about a day, is the beginning of the end of the star, as no energy can be gained from nuclear fusion of iron. The core collapses into a neutron star, and for the most massive stars into a black hole. Most of the gravitational energy liberated ($E \approx GM^2/R_{ns} \approx 10^{53}$ erg, with R_{ns} the neutron star radius) is in the form of neutrinos. This has been confirmed with the detection of neutrinos from SN1987A by the Kamiokande [23] and Irvine-Michigan-Brookhaven [24] water Cherenkov

neutrino detectors. A fraction of about $2 \cdot 10^{51}$ erg is deposited in the outer layers which are expelled at a velocity of approximately 10^4 km/s (supernova explosion).

Thermonuclear supernovae (Type Ia) are thought to originate from the explosions of white dwarfs. In this case, the explosion energy originates from explosive nuclear burning, rather than from gravitational energy liberated during the collapse of a stellar core. It has been observed that Type Ia supernovae have almost the same brightness, which makes them excellent distance indicators.[4] This is in line with the idea that all Type Ia Supernovae are explosions of similar objects, i.e. white dwarfs with masses close to the Chandrasekhar limit. There is no direct observational evidence that Type Ia progenitors are white dwarfs. In old stellar populations only Type Ia Supernovae are observed, indicating that massive stars cannot be their progenitors. White dwarfs close to the Chandrasekhar mass limit are very likely Type Ia progenitors, since their high density is ideal for a "nuclear fusion bomb". Once a nuclear reaction in the core is triggered, it will result in an explosion. The transition from white dwarf to Supernova requires that the star increases its mass to reach (and overcome) the Chandrasekhar limit. This leads to the conclusion that thermonuclear Supernovae must occur in binary systems, for example a two-white dwarf system or a white dwarf plus either a main sequence star or an evolved companion.

2.3 Supernova Remnants

The Supernova explosion generates a shock wave which propagates in the surrounding interstellar medium. This shock wave hits the cold gas and transforms its directional kinetic energy into thermal energy.

In shock waves commonly observed on the Earth, the mechanism responsible for this energy transformation is due to the particle collisions. In this case the thickness of the shock is of the order of the mean free path of the particles $\lambda = 1/(n\sigma)$, where n is the particle density and σ is th cross section of the process. For typical shocks in the atmosphere, $n \sim 10^{23}\text{cm}^{-3}$ and $\sigma \sim \pi a_B^2$, being $a_B \sim 10^{-8}$cm the Bohr radius of an atom, which results in $\lambda \sim 10^{-7}$cm, sufficiently small to consider the shock infinitely thin. This type of shocks are called *collisional* shocks.

[4] This aspect was at the basis of the analysis of cosmological red-shift of distant objects, which proved that the Universe is accelerating (*dark energy*) (see for example [25]). For this discovery Riess, Perlmutter and Schmidt were awarded the Nobel Prize for Physics in 2011.

However, in the astrophysical situations, this approach is not consistent. First, the ISM is usually fully ionized, so the nuclear radius must be considered instead of the atom one ($\sim 10^{-13}$cm). Secondly, the typical ISM density is much smaller than the one of the atmosphere, with $n \sim 1\text{cm}^{-3}$. The previous calculation leads to the unreasonable value of $\lambda \sim 10^{26}\text{cm} \approx 10^{4}\text{kpc}$, well above the size of our Galaxy. The mechanism at the base of the shock wave is different in this case. Since particles in the ISM are ionized, electrons and ions are accelerated by the electric and magnetic fields in the ISM. In particular, electro-magnetic instabilities generated by the plasma allow the particle energy isotropization. In this case the typical size of the shock is of the order of the Larmor radius of a proton:

$$\lambda \sim r_L = \frac{mv}{eB} \approx 10^{10}\text{cm}\frac{v}{10^4\ \text{km s}^{-1}}\frac{10^{-6}\text{G}}{B}, \tag{2.1}$$

where $v \sim 10^4$ km s^{-1} and $B \sim 10^{-6}$G are typical values of the ejected particle velocity and of the Galactic magnetic field respectively.

2.3.1 Evolution

The mechanisms responsible for the creation of the shock wave is not completely understood for both thermonuclear and core collapse Supernovae. Most of numerical simulations assume istantaneous and point-like energy release and a symmetric propagation in the interstellar medium. Once the explosion is generated the evolution of the SNR can be studied and its evolution is divided in four phases.

At the beginning, the mass of the supernova ejecta, M_{ej}, is greater than the swept-up mass, M_{sw}, and the expansion proceeds freely (*free expansion* phase). Typically, $M_{ej} \sim 10M_\odot \approx 10 \times 2 \cdot 10^{30}$kg and the total energy of the explosion is $E = M_{ej}V^2/2 \approx 10^{51}$erg, with $V \approx 10^4$km/s. Since V is much larger than the typical sound speed in the intersterllar medium ($c_s \approx 10$ km/s), a collisionless shock wave is generated.

The free expansion proceeds until the swept mass becomes comparable to the ejected mass:

$$\frac{4\pi}{3}\rho_{ISM}R_s^3 = M_{ej}, \tag{2.2}$$

where $\rho_{ISM} = nm_p = 10^{-24}$g cm^{-3} is the density of the intersterllar medium. Inverting the equation one finds the radius of the SNR $R_s \sim 4$pc, corresponding

to a time $t_S = R_s/V \sim 300$yr. The exact values of R_s and t_S depend on the SNR type and on the environment in which the shock propagates. For example, if the environment around the shock were more dense, t_S would be smaller.

At this time the SNR enters in the second phase of its evolution, called *Sedov-Taylor* or *adiabatic* phase. In this phase the inertial mass of the swept material cannot be neglected. However, the gas is sufficiently hot to prevent any energy losses by radiation and the total energy is conserved. In fact, the electron temperature is given by $kT_e \approx m_e V^2/2$, giving $T_e \approx 10^7$K, which corresponds to a cooling time $t_c \approx 10^6$yr, much larger than the SNR age.

The SNR evolution in the adiabatic phase is described by the so called Sedov-Taylor solution, which gives $R_s \propto t^{2/5}$, $V_s = dR_s/dt \propto t^{-3/5}$ and $T_s \propto t^{-6/5}$. While expanding, the shock slows and cools down. The slowing down is mediated by a pressure wave which propagates towards the center of the SNR and might generate another shock if its amplitude is sufficiently high. This second shock wave is called *reverse shock* and separates the internal material which is still in the free expansion phase from the shocked material in the Sedov-Taylor phase (see figure 2.1). It must be noted that the *reverse shock* propagates backwards respect to the main shock, but not necessarily geometrically towards the center of the SNR, since it is partially dragged by the expanding material.

The Sedov-Taylor phase ends when the gas temperature drops below $\approx 10^6$ K, when electrons start recombining with ions and emit radiation. From the Sedov-Taylor solution, this transition happens at the time $t_{SP} \approx 2 \times 10^4$yr, when the radius of the SNR is $R_{SP} \approx 15pc$. This phase can be described imposing the conservation of the total momentum of the SNR:

$$MV_s = \frac{4\pi}{3}\rho_{ISM} R_s^3 V_s = cost \Rightarrow R_s \propto t^{1/4}, V_s \propto t^{-3/4}. \tag{2.3}$$

This phase is called *snowplough* phase, since material accumulates in a dense region outside the shock. A detailed description of this phase is much more complicated, since the pressure of the internal gas which changes the total momentum should be included. Numerical simulations have shown that the transition from the Sedov-Taylor to the snowplough phase is charaterized by a long intermediate phase when $R_s \propto t^{0.3}$.

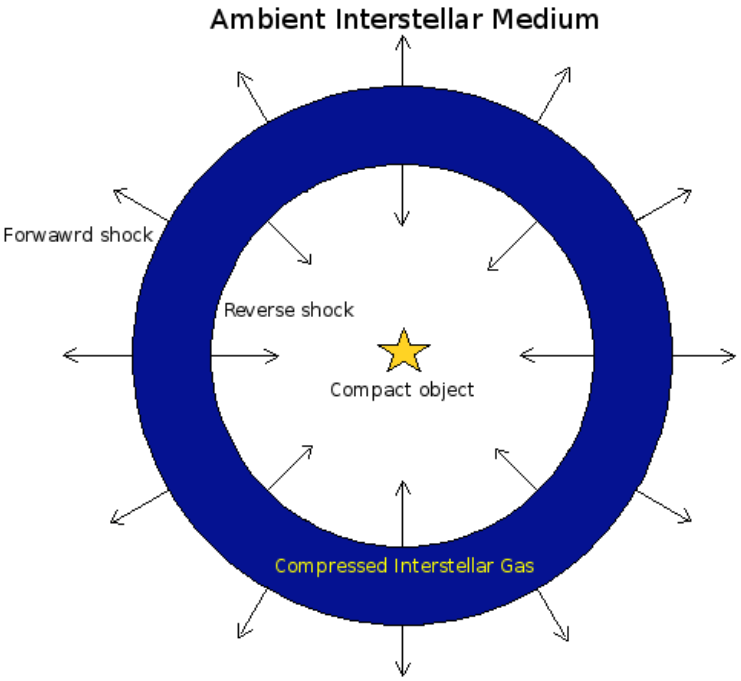

FIGURE 2.1: SNR evolution scheme.

Finally, when the shock velocity and temperature behind the shock become comparable to the turbulent velocity and temperature of the interstellar medium respectively, the SNR merges in the interstellar medium. This is the last step of the evolution and is called *merging phase*.

In real cases, the evolution stage of a SNR is not easily labeled. Since the shock often propagates in a non-uniform medium, different parts of the SNR might be in different phases. For example, the SNR RCW 86 has radiative shocks in the south-west (*snowplough* phase), whereas in the north-east it has very fast, non-radiative, shocks (*free expansion* phase). This is probably due to the complexity of the medium in which the SNR is developing.

In the literature one also often finds designations for SNRs like *young*, *mature* and *old*. These designations do not have a very precise meaning, but a general guideline is that young SNRs are less than 1000 - 2000 years old and are in the *free expansion* phase or in the early Sedov-Taylor phase, mature SNRs are in late Sedov-Taylor phase or early *snowplough* phase, whereas the label old SNRs is usually given to the very extended structures associated with SNRs in the last phase.

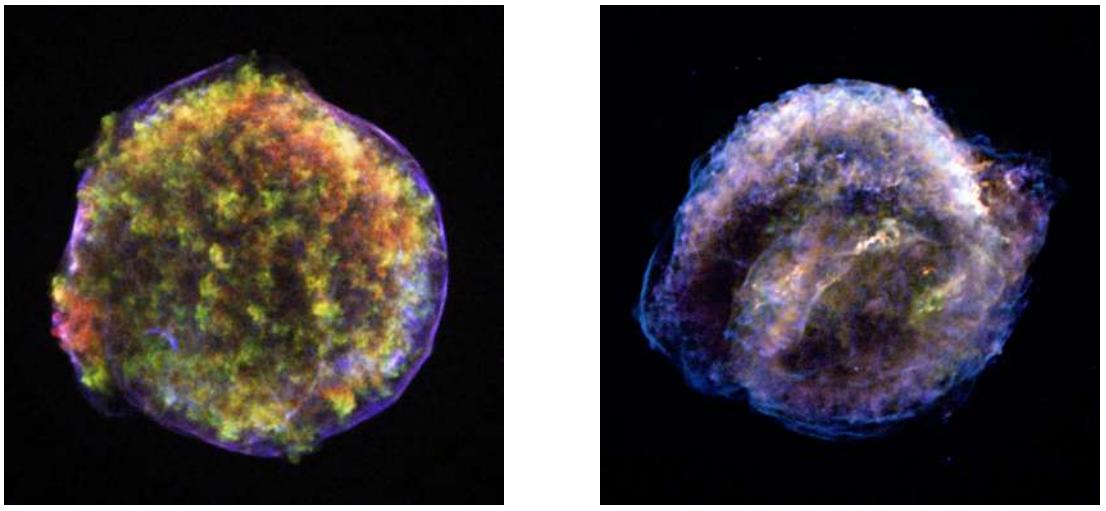

(A) (B)

FIGURE 2.2: Tycho and Kepler SNRs.

2.3.2 Classification

In principle, the classification of SNRs could follow the one adopted for Supernovae. However, it is often difficult to determine the Supernova origin of a given SNR. There are some indicators which give hints about their origin. For example, the presence of a neutron star at the center of the SNR is a clear sign that the SNR must have a core-collapse origin. The position of the SNR in the Galaxy gives other information. Since core-collapse SNe originate from massive stars which stay in the main sequence for a shorter period, they must be located in a star forming region. On the contrary, if the SNR is located high above the Galactic plane it will probably have a Type Ia origin. Such is the case, for example, of SN 1006.

Because the supernova origin of SNRs is often difficult to establish, SNRs have an own classification, mostly based on their morphology. Traditionally, this classification recognises three classes: *shell-type* SNRs, *plerions* and *composite* SNRs.

The *shell-type* SNRs are characterized by a limb brightened shell, which is created by a shell of shocked heated plasma originating from the interstellar medium swept by the shock wave. The shell is usually clearly visible in the radio and X-ray bands, due to the non-thermal synchrotron emission of relativistic electrons deflected by the magnetic field. Two of the most famous examples of these SNRs are Tycho and Kepler, originating from the supernova explosion of 1572 and 1604 respectively (figures 2.2).

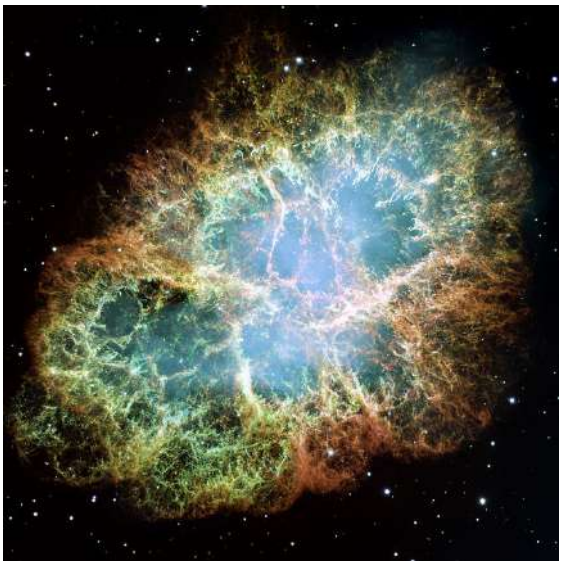

FIGURE 2.3: Crab nebula.

In the case of a core-collapse Supernova, a rapidly rotating neutron star, called *pulsar*, is expected at the center of SNR. The pulsar will lose energy according to its rotational period and will produce a wind of relativistic electrons and positrons, which terminates in a shock, where the electrons and positrons are accelerated to ultra-relativistic energies. These particles diffuse away from the shock creating a nebula of relativistic particles which emit synchrotron radiation from the radio to the soft X-ray bands, and inverse Compton scattering in the GeV - TeV band. Such a nebula is named *pulsar wind nebula*. The most famous pulsar wind nebula is the Crab Nebula, associated with the historical supernova of 1054 (figure 2.3). Since the nebula is bright at the center and does not show a shell, these SNRs are called *filled center* SNRs or *plerions*, with the name *plerion* deriving from the Greek word *pleres*, which means "full".

Finally, energetic pulsars with ages less than 20000 years are expected to have blown a pulsar nebula while they are still surrounded by the SNR shell. One expects then a radio and X-ray morphology that consists of a pulsar wind nebula surrounded by a shell and are classified as *composite* SNRs. In fact, it is still puzzling why a young object like the Crab Nebula does not show a SNR shell.

Most of the already classified SNRs are shell-type SNR, due to the fact that they are much easier to recognise. One of the most complete catalogs of SNRs was produced by Dave Green in 1984, in which he collected all the known SNRs, summarising their main features, such as the position in the sky, the extension, the characteristics of the spectrum in different energy bands and some possible

associations with objects observed at different wavelengths. Updated versions of this catalog are available at [26] and [27].

2.4 Cosmic ray acceleration in Supernova Remnants

Supernova Remnants are thought to be the main acceleration sites of Galactic Cosmic rays (*SNR paradigm*). Acceleration theories have been studied for long times in order to explain how CRs can be accelerated up to the high energies that we observe on the Earth, i.e. close to the "knee" of the CR spectrum.

The number of Supernova explosions in the Galaxy and the energy released in these explosions could in principle explain the measured CR density $\rho_{CR} \approx 1eV/cm^3$. In fact, if R_{SN} ∼3 SN/century is the SN explosion rate, $E_{SN} \sim 10^{51}$ erg is the SN explosion energy and $\tau_e \sim 10^7$ years is the CR escaping time, the CR energy density can be expressed as:

$$\rho_{CR} = R_{SN} E_{SN} \tau_e \epsilon, \tag{2.4}$$

where ϵ is the fraction of the SN explosion energy which is transferred to CRs. Inserting the previous values in equation (2.4), one gets the expected acceleration efficiency $\epsilon \sim 10\%$.

In chapter 1, it was shown that CR spectrum at the source should be described by a power-law with spectral index slightly softer than 2. The *Diffusive Shock Acceleration* (DSA) theory, also known as *First order Fermi mechanism*, is the most commonly accepted to explain the acceleration of CRs. The main ingredient of this mechanism is the presence of a strong shock wave propagating in the intersterllar medium, like the ones generated in a SN explosion.

2.4.1 Second order Fermi mechanism

The first formulation of the DSA is due to Enrico Fermi, whose original idea was actually different from the DSA and is known as *second order Fermi mechanism* [28, 29]. Particles are assumed to be accelerated thanks to stochastic collisions with

the clouds (and in particular with the magnetic field irregularities inside them, also called *magnetic mirrors*) moving isotropically in the interstellar medium.

Suppose that a particle with initial energy E and a magnetic mirror moving with velocity V collide forming an angle θ between the particle trajectory and the direction perpendicular to the mirror surface (see figure 2.4). The mirror is supposed to be infinitely massive, so that it does not change velocity during the collision. In the frame of reference of the mirror, which corresponds with the center of mass frame of reference, the particle has a total energy

$$E' = \gamma_V(E + Vp\cos\theta), \tag{2.5}$$

where $\gamma_V = (1 - V^2/c^2)^{-1/2}$ is the Lorentz factor of the mirror. The component of the momentum of the particle perpendicular to the mirror is given by

$$p'_x = p'\cos\theta' = \gamma_V(p\cos\theta + \frac{VE}{c^2}). \tag{2.6}$$

In this frame of reference the energy of the particle does not change during the collision $E'_{\text{in}} = E'_{\text{fin}}$, while p'_x changes sign, $p'_{x,\text{fin}} = -p'_{x,\text{in}}$.

Going back to the laboratory frame of reference and using equations (2.5) and (2.6):

$$E'' = \gamma_V(E'+Vp'\cos\theta') = \gamma_V(E'+Vp'_x) = \gamma_V^2 E\left[1 + \frac{2Vv\cos\theta}{c^2} + \left(\frac{V}{c}\right)^2\right], \tag{2.7}$$

where v is the initial velocity of the particle in the laboratory frame of reference, so that $p_x/E = v\cos\theta/c^2$.

Expanding to second order in $\beta_V = V/c$.

$$\Delta E = E'' - E = E\left(\frac{2\beta_V v\cos\theta}{c} + 2\beta_V^2\right). \tag{2.8}$$

The angular dependence can be eliminated taking an average over a random distribution of the pitch angle θ. The probability of encounters taking place at an angle θ is proportional to the relative velocity of approach of the particle and the cloud, namely, from figure 2.4, $V + v\cos\theta$ for a head-on collision and $V - v\cos\theta$ for a following collision. Therefore, the probability can be written as $V + v\cos\theta$

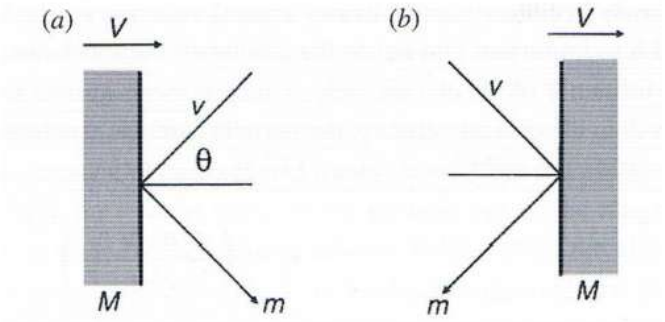

FIGURE 2.4: Second order Fermi acceleration mechanism.

with $0 < \theta < \pi$. Since the particles are relativistic, $v \approx c$ and the probability is proportional to $(1 + V/c\cos\theta) = (1 + \beta_V \cos\theta)$.

The energy gain becomes:

$$\left\langle \frac{\Delta E}{E} \right\rangle = 2\beta_V \frac{\int_{-1}^{1} x(1+\beta_V x)dx}{\int_{-1}^{1}(1+\beta_V x)dx} + 2\beta_V^2 = \frac{8}{3}\beta_V^2. \tag{2.9}$$

The calculation showed that the average increase in energy is *second-order* in β_V.

However, this mechanism proved to be unable to explain the CR acceleration. In fact, the velocities of the interstellar clouds are small compared to the speed of light ($\beta_V \leq 10^{-4}$) and the mean free path for the scattering of cosmic rays in the interstellar medium is of the order of 0.1 pc, resulting in a very slow gain of energy by the particles, which could not compensate for the energy lost by ionization between subsequent collisions.

2.4.2 First order Fermi mechanism

Unlike the second order Fermi mechanism, the DSA involves the interaction of the particles with a shock wave propagating in a diffuse medium. A flux of high energy particles is assumed to be present both in front of and behind the shock front. The particles are assumed to be propagating at speeds close to that of light and so the velocity of the shock is very much less than those of the high energy particles. The high energy particles scarcely notice the shock at all since its thickness is normally very much smaller than the gyroradius of the high energy particle. Because of scattering and turbulent motions on either side of the shock wave, when the particles pass through the shock in either direction, they are

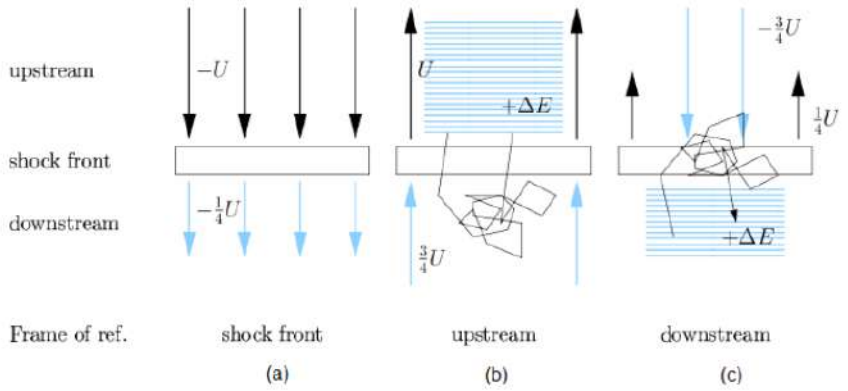

FIGURE 2.5: First order Fermi acceleration mechanism.

scattered and their velocity distribution rapidly becomes isotropic in the frame of reference of the moving fluid on either side of the shock.

A typical shock wave propagates with a velocity U of 10^4 km s^{-1}, much higher than the sound speed (≈ 10 km s^{-1}). Be ρ_1 and ρ_2 the gas densities in the upstream and the downstream respectively. It is often convenient to transform into the frame of reference in which the shock front is at rest, so that the upstream gas flows into the shock at velocity $v_1 = U$ and leaves the shock with a downstream velocity v_2. The equation of continuity requires that mass is conserved through the shock, so:

$$\rho_1 v_1 = \rho_1 U = \rho_2 v_2. \tag{2.10}$$

In the case of a strong shock, $\rho_1/\rho_2 = (\kappa+1)/(\kappa-1)$, where κ is the ratio of specific heat capacities of the gas. Taking $\kappa = 5/3$ for a monoatomic of fully ionised gas, $\rho_1/\rho_2 = 4$ and so $v_2 = v_1/4$ (figure 2.5a).

Consider the frame of reference in which particles in the upstream are at rest (figure 2.5b). The shock advances through the medium at velocity U but the gas behind the shock travels at a velocity $(3/4)U$ relative to the upstream gas. When a high energy particle crosses the shock front, it obtains a small increase of energy or order $\Delta E/E \propto U/c$. The particles are then scattered in the region behind the shock front so that their velocity distributions become isotropic with respect to that flow.

Now consider the opposite process of the particle diffusing from behind the shock to the upstream region (figure 2.5c). When the particles cross the shock front, they

encounter gas moving towards the shock front with the same velocity $(3/4)U$ as the previous case, which means that the particle receives the same small amount of energy ΔE.

This is the main difference with respect to the second-order mechanism. All collisions can be considered *head-on* collisions and particles increase their energy every time they cross the shock .

To evaluate the average increase in energy, consider a particle crossing the shock front from the upstream to the downstream. The gas on the downstream side approaches the particle at a velocity $V = (3/4)U$ and so, performing a Lorentz transformation, the particle's energy when it passes into the downstream region is

$$E' = \gamma_V (E + p_x V), \tag{2.11}$$

where the x-coordinate is taken perpendicular to the shock.

The shock is assumed to be non-relativistic, so $V \ll c$ and $\gamma_V \approx 1$, while the particles are relativistic, so $E = pc$ and $p_x = (E/c)\cos\theta$. Therefore,

$$\frac{\Delta E}{E} = \frac{V}{c}\cos\theta = \beta_V \cos\theta. \tag{2.12}$$

The probability that the particles which cross the shock arrive within the angles θ to $\theta + d\theta$ is proportional to $\sin\theta\ d\theta$ and the rate at which they approach the shock front is proportional to the x-component of their velocities, $c\cos\theta$. Therefore the probability of the particle crossing the shock is proportional to $\sin\theta\cos\theta\ d\theta = \cos\theta\ d\cos\theta$. So, defining $x = \cos\theta$ the average energy gain is

$$\left\langle \frac{\Delta E}{E} \right\rangle = \beta_V \frac{\int_0^1 x\ x dx}{\int_0^1 x dx} = \frac{2}{3}\beta_V. \tag{2.13}$$

The particle's velocity is then randomised without energy loss by scattering in the downstream region. Then, it recrosses the shock and gains another fractional increase in energy $(2/3)\beta_V$. Therefore, in a round trip across the shock and back again, the fractional energy increase is, on average,

$$\left\langle \frac{\Delta E}{E} \right\rangle = \frac{4}{3}\beta_V = \frac{4}{3}\frac{3}{4}\frac{U}{c} = \frac{U}{c}. \tag{2.14}$$

This mechanism is much more efficient than the previous one, since the energy gain is linear with the velocity of the shock. Another important implication of the DSA is that it can predict the shape of the particle spectrum, as it will be shown in the next section.

2.4.3 Particle spectrum

The particle spectrum can be easily estimated assuming that a particle has a certain probability of escaping from the acceleration region after each collision. Be $\Delta E = \xi E$ the energy earned by a particle after a collision and P_{esc} the escape probability. After n collisions, a particle with initial energy E_0 will have an energy $E_n = E_0(1+\xi)^n$, with a probability of being in the acceleration region equal to $(1-P_{\text{esc}})^n$. The number of collision necessary to reach an energy E is obtained inverting the first relation: $n = \ln(E/E_0)/\ln(1+\xi)$. The number of particles with energy greater than E will be proportional to the probability of having a particle with energy greater than E:

$$N(\geq E) \propto \sum_{m=n}^{\infty}(1-P_{\text{esc}})^m = \frac{(1-P_{\text{esc}})^n}{P_{\text{esc}}}. \tag{2.15}$$

Using the expression of n obtained previously:

$$N(\geq E) \propto \frac{1}{P_{\text{esc}}}\left(\frac{E}{E_0}\right)^{-s}, \tag{2.16}$$

where

$$s = \ln\left(\frac{1}{1-P_{\text{esc}}}\right)/\ln(1+\xi). \tag{2.17}$$

The differential energy spectrum in obtained differentiating equation (5.4):

$$N(E)dE \propto E^{-1-s}dE. \tag{2.18}$$

In the case of the DSA, the spectral index can be easily calculated. From equation (2.14), $\xi = U/c$. The escape probability P_{esc} can also be estimated. According to classical kinetic theory, the number of particles crossing the shock is $(1/4)Nc$ where N is the number density of particles. This is the average number of particles

crossing the shock in either direction. Downstream, however, because the particles are isotropic, they are swept away from the shock at a rate $NV = (1/4)NU$. Thus, the fraction of the particles lost per unit time is $(1/4)NU/(1/4)Nc = U/c$. Since the shock is assumed to be non-relativistic, only a very small fraction of the particles is lost per cycle. Thus,

$$P_{esc} = U/c. \tag{2.19}$$

Substituting (2.14) and (2.19) in (2.17) and taking into account that $U \ll c$,

$$s = -\frac{\ln(1 - P_{esc})}{\ln(1 + \xi)} = -\frac{\ln(1 - U/c)}{\ln(1 + U/c)} \approx -\frac{-U/c}{U/c} = 1. \tag{2.20}$$

Therefore, the differential energy spectrum from equation (2.18) becomes

$$N(E)dE \propto E^{-2}dE. \tag{2.21}$$

A more detailed description of the particle acceleration would include the study of the transport equation of CRs in the SNR. The solution of this equation gives the distribution function $f(x, p)$ of the accelerated particles. In the case of the DSA, one finds:

$$f(x, p) \propto \left(\frac{p}{p_0}\right)^{-\alpha}, \tag{2.22}$$

with $\alpha = 3r/(r + 1)$, where r is the compression factor of the shock. As already pointed out, for a strong shock the compression factor is $r = 4$, implying $\alpha = 4$. The differential energy spectrum is then easily recalled:

$$N(E)dE = 4\pi p^2 f(x, p)\frac{dp}{dE}\, dE \Rightarrow N(E)dE \propto E^{-2}dE, \tag{2.23}$$

where the last step is valid for relativistic particles.

2.4.4 Non-linear Diffusive Shock Acceleration

The DSA theory described in the previous section, also called test-particle theory, presents some limitations and approximations, leading to predictions incosistent with observations. First, the required spectral shape of the CR spectrum at the source is expected to be softer than -2, also confirmed by γ-ray observations

of SNRs. Secondly, the shape of the spectrum derived does not depend on the diffusion of particles in the shock region, implying that the result is valid for any particle energy. The spectral shape might then extend up to the infinite particle energy, resulting in a divergent energy content of particles.

One of the main problems in the test-particle theory is due to the dynamical reaction of accelerated CRs on the shock. As already pointed out, the DSA mechanism is supposed to transfer a fraction of $\sim 10\%$ of the explosion energy to CRs, implying that CRs contribute to the momentum and energy conservation equations. This theory is usually called Non-linear Diffusive Shock Acceleration (NLDSA).

The pressure generated by CRs is largest at the shock front and progressively decreases far upstream from it. This is due to the fact that fewer particles can reach larger distances, creating a *precursor*, i.e. a region close to the shock where the fluid density increases and its velocity decreases, creating a *subshock* discontinuity. The velocity profile is represented in figure 2.6. The compression factor r at the subshock is then reduced to values smaller than 4, while the overall compression factor may be much larger than 4. High energy particles may diffuse far from the shock and experience the large compression factor with a consequent flattening of the spectrum.

This causes the particle spectrum to deviate from the simple power-law, producing a concave shape which is steeper than 4 for low-energy particles and flatter for higher energies. The transition typically takes place at energies of a few GeV. Figure 2.7 represents an example of the particle distribution function for different shock parameters.

Magnetic field amplification

Another consequence of the NLDSA is the magnetic field amplification, which reaches values $\sim 10 - 100$ times larger than the average Galactic magnetic field. One of possible explanations of this phenomenon is related to the plasma instabilities driven by the CRs themselves, as they propagate through the upstream medium. When energetic particles reach a speed larger than the Alfvén velocity, which is the characteristic velocity of magnetic turbolences, Alfvén waves are amplified thanks to the collective effect of the streaming CRs [32].

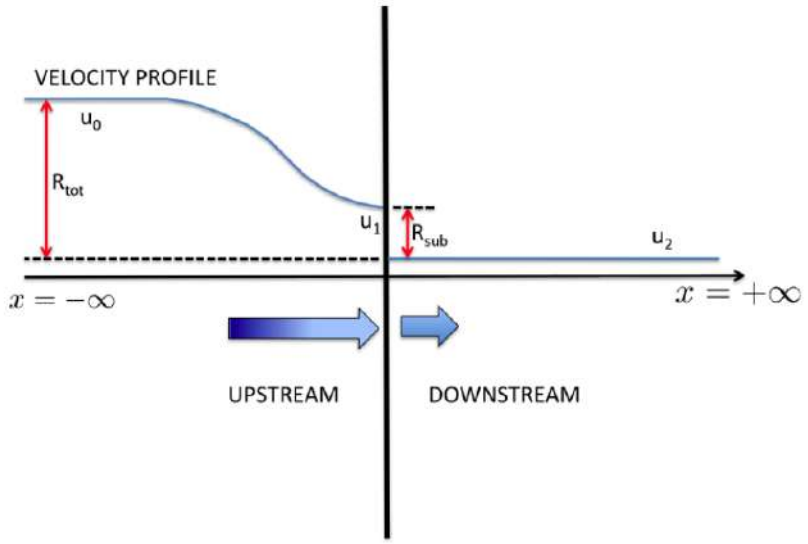

FIGURE 2.6: Velocity profile in the shock region in NLDSA [30].

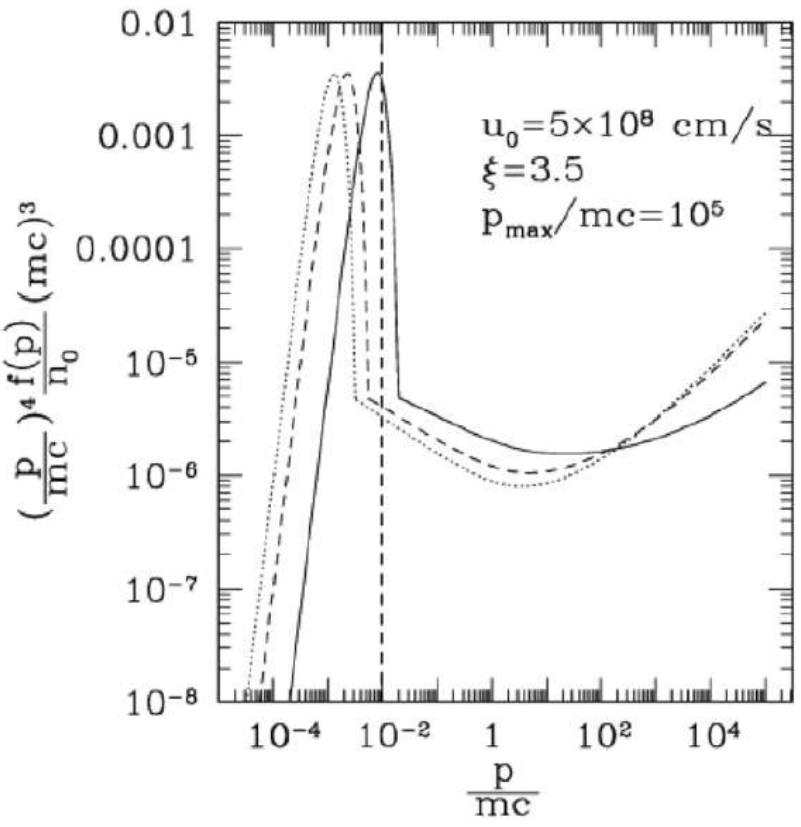

FIGURE 2.7: Particle spectra (thermal plus non-thermal) at a CR modified shock with Mach number 10 (solid line), 50 (dashed line) and 100 (dotted line) [31].

X-ray observations of SNRs have provided the experimental evidences of the magnetic field amplification. Narrow filaments of X-ray emission have been observed close to the shock in young SNRs, due to the synchrotron emission of accelerated electrons. The observed thickness of the order of 10^{-2} pc requires a magnetic field of several hundreds μG. Figure 2.2 shows the X-ray rims observed in Tycho and Kepler SNRs. These observations provide the most important evidence of the NLDSA theory.

The contribution of the magnetic field may also modify the particle spectra. The compression ratio is modified by the magnetic wave velocity and may result in a steeper spectrum also at high energies.

2.5 γ-rays from SNRs

Cosmic ray acceleration mechanisms described in previous sections cannot be studied through the direct observation of accelerated particles. In fact, these particles are deflected by the Galactic magnetic field and their spectrum is also modified during their propagation to the Earth, as already shown in chapter 1.

However, in the section 1.5, it was shown that high energy particles can produce non-thermal photons in a wide energy range, which travel straight to the Earth allowing the study of the source. For this reason the multi-wavelength study of the SNR spectrum can provide strong constraints on the SNR environment and on the populations of accelerated particles. The accelerated proton spectrum is the most interesting in order to have hints of the acceleration of cosmic rays in SNRs and therefore, the γ-ray spectrum acquires a key role in the search for evidences of the so called *SNR paradigm* for CRs. In fact, three of the four processes described in section 1.5 contribute to the γ-ray spectrum and usually one of them is expected to be the dominant one, even though models including different contribution are possible. The photon flux in general depends on many parameters characterising the SNR, such as the ambient density or the magnetic field. In most cases, these parameters are not known, but some constraints are dictated by multi-wavelength observations. Therefore, it might be difficult to discern among the different contributions at high energy.

One of the most convincing way of proving the hadronic origin of the γ-ray flux is the observation of the shape of the spectrum at energies below 100 MeV, where

the π^0-decay spectrum presents a break due to the threshold energy of the pion production, often called *pion bump*. In this frame, *Fermi*-LAT experiment, which is sensitive to an energy range from few tens of MeV to few TeV and will be widely described in the following chapters, does have an essential role.

2.5.1 SNRs with *Fermi*-LAT

The *Fermi*-LAT experiment has detected the *pion bump* signature in many SNRs. The first clear detection occurred in the observation of IC443 and W44 SNRs [33]. They are middle-aged SNRs interacting with a molecular cloud, i.e. with a dense cloud of target gas, allowing the production of a strong γ-ray flux. W51 provides another example of middle-aged interacting SNR, with the detection of the *pion bump* [34]. These SNRs are very bright objects in γ-rays, thanks to their interaction with the dense cloud, which enhances the γ-ray flux due to CR protons and highlights the *pion bump* signature. Figure 2.8 shows the Spectral Energy Distributions (SEDs) of these three SNRs, obtained as the differential photon flux multiplied by E^2. Data are compared to different models based on different contributions to the γ-ray spectrum. Solid lines are based on the π^0 decay (hadronic origin), while dotted lines are based on the bremsstrahlung emission of high energy electrons (leptonic origin). It can be noticed that in all cases the data points at energies around and below 100 MeV strongly support the π^0-decay hypothesis.

The spectra of IC 443 and W 44 SNRs show another important spectral feature. As described in [33], the γ-ray spectrum is well described by a model in which a broken power-law is assumed for accelerated protons. The existence of this break is not predicted by the acceleration mechanisms and its origin is probably related to their interaction with the molecular clouds. One of the possible explanations is that high energy particles might have escaped the acceleration regions, being the SNR in an advanced stage of its evolution, causing the steepening of the spectrum at high energies. On the other side, models of re-acceleration of Galactic CRs at the SNR shock can explain these spectral break in the γ-ray spectrum without introducing any spectral feature in the particle populations [35].

Due to their evolution stage and complex environment in which the shock is propagating, middle-aged SNRs are not the ideal cases to test and study the acceleration mechanisms. Young SNRs (less than a few thousand years old) are often preferred for this purpose. They often propagate in clean enviroments and the

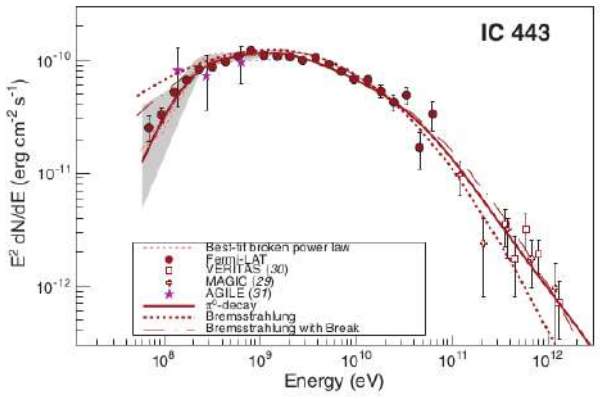

(A)

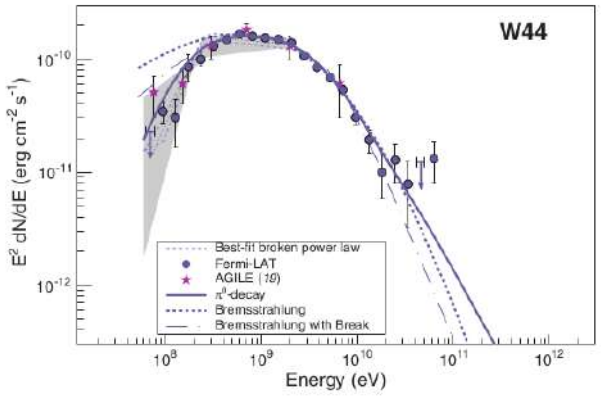

(B)

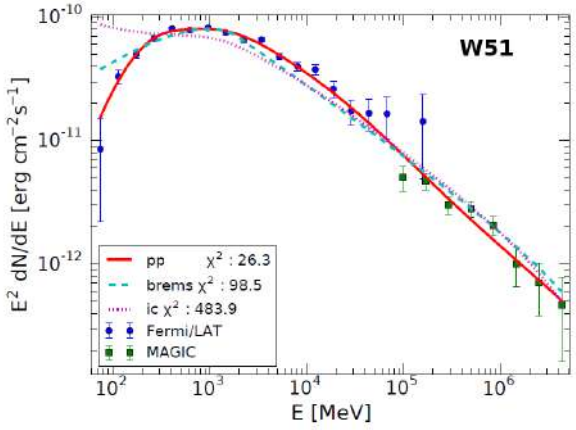

(C)

FIGURE 2.8: Gamma-ray spectra of IC 443 (A), W44 (B) and W51 (C) as measured with the *Fermi*-LAT. Figures (A) and (B) are taken from [33]. Gray-shaded bands show systematic errors below 2 GeV due mainly to imperfect modelling of the galactic diffuse emission. TeV spectral data points for IC 443 are from MAGIC and VERITAS experiments, while magenta stars denote measurements from the AGILE satellite. Solid lines denote the best-fit pion-decay gamma-ray spectra, dashed and dash-dotted lines denote the best-fit bremsstrahlung spectra without and with a low-energy break at 300 MeV/c in the electron spectrum. Figure (C) is taken from [34]. *Fermi*-LAT data include systematic uncertainties. TeV data are taken from MAGIC experiment. The solid line represents the best-fit hadronic model, while dotted and dashed lines are based on leptonic models.

detailed X-ray observations show evidence of non-thermal emission, as already pointed out for example in figure 2.2. Furthermore, SNRs which have just entered in the Sedov-Taylor phase are the ideal candidates to get information about the maximum energy of acceleration in SNRs, being the energy losses still negligible.

RX J1713.7-3946 [36] and RCW 86 [37] provide two examples of young SNRs. Their SEDs are represented in figure 2.9. The interpretation models overlaid to the measured spectra show that the leptonic interpretation is preferred in both cases, being the γ-ray spectrum well described by the Inverse Compton emission. The absence of the hadronic signature does not exclude the presence of accelerated protons at the source. The low density of the ambient in which the shock is propagating might be responsible for the non-detection of the contribution of accelerated protons. Indeed, recent detailed observations of RX J1713.7-3946 have shown the existence of a possible subdominant hadronic component.

Furthermore, recent upgrades in the *Fermi*-LAT instrument response (see chapter 3) allowed a detailed comparison of the GeV γ-ray emission with the spatial shapes observed at other wavelengths. For example, the study of RCW 86 has shown that the GeV emission is well correlated to the TeV emission observed by the H.E.S.S. experiment, suggesting that both emissions come from the same region of the SNR. These type of studies are also essential to correctly correlate the multi-wavelength information, since different regions of the SNR might be characterized by different emissions.

Other two examples of shell-type young SNRs Cassiopeia A (Cas A) and Tycho. Previous γ-ray observations of these two SNRs have provided indications of a hadronic emission of the spectrum. Both the SNRs have been deeply studied in this work and their cases will be discussed in chapters 5 and 6.

The first *Fermi*-LAT Supernova Remnant Catalog

A more systematic study of SNRs has been recently developed by the *Fermi*-LAT collaboration, producing the first *Fermi*-LAT Supernova Remnant catalog [38]. Three years of data between 1 and 100 GeV were analyzed to study the 279 radio SNRs in [39]. 102 candidates were detected with a significance above 5σ, 36 of which were successfully associated to the corresponding radio SNR. Four of these sources were identified as sources which are not SNRs, while 14 other sources did not pass the association threshold and were marginally classified. 17 SNRs

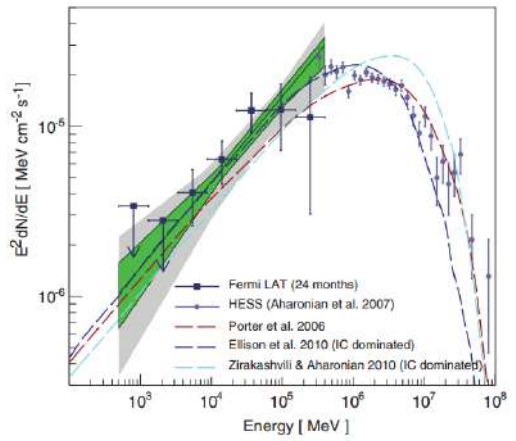

(A)

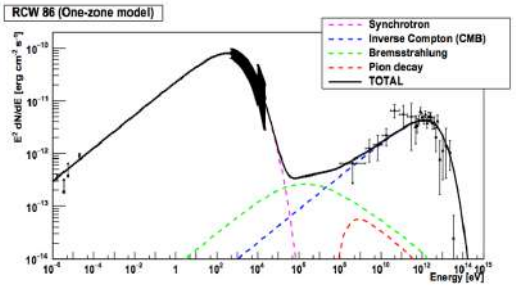

(B)

FIGURE 2.9: Spectral Energy Distribution of two young SNRs, overlaid with theoretical models based on a leptonic interpretation of the γ-ray emission. (a): RX J1713.7-3946. The lines represent different interpretation models in which the γ-ray emission (solid line) is dominated by the IC scattering [36]. (b): RCW 86. The lines represent the contribution of different emission mechanisms. The total γ-ray emission (solid line) is dominated by the IC scattering [37].

showed evidence for extension. 14 of the associated SNRs had not been detected before in the GeV energy range. A detailed analysis of the spatial and spectral characteristics of these sources was conducted.

Figure 2.10 summarizes the results of the catalog, showing the scatter plot between the γ-ray flux and spectral index of the detected sources. A multi-wavelength study was also done when possible, searching for possible correlations between γ-ray and radio or TeV spectral indices. Due to the limited sample of detected SNRs and to the relative large errors, no clear correlation was found. The main conclusion in this case is that the simple relations between radio and γ-ray index are not satisfied in the majority of the observations, implying that simple assumptions on the interpretation models are not enough.

Finally, in order to verify whether SNRs are capable of supplying the observed CR

energy density, an estimate of the CR energy content was derived from the measured 1 GeV - 100 GeV flux, under the hypothesis that γ-ray emission arises from the interaction of CR protons with the surrounding gas. Given that also the two other emission mechanisms involving accelerated electrons could also contribute to the γ-ray flux, the estimates derived must be considered as upper limits on the CR energy content in each SNR.

As seen in [38] and references therein the expected γ-ray flux is nearly independent of the CR maximal energy as long as $E_{CR,max} \gtrsim 200$ GeV and the CR spectral index $\Gamma_{CR} \gtrsim 2$. In this case, it can be conveniently approximated using the following expression:

$$F(1-100\mathrm{GeV}) \approx f(\Gamma_{CR}) \, \frac{\epsilon_{CR}}{0.01} \, \frac{E_{SN}}{10^{51}\mathrm{erg}} \, \frac{n}{1\mathrm{cm}^{-3}} \left(\frac{d}{1\mathrm{kpc}} \right)^{-2} 10^{-9}\mathrm{cm}^{-2}\mathrm{s}^{-1} \quad (2.24)$$

where $f(\Gamma_{CR})$ is such that $f(2.0) = 2.06$, $f(2.5) = 1.07$, and $f(3.0) = 0.34$.

The CR energy content expressed as a fraction of the Supernova explosion energy E_{SN} can be derived using the measured γ-ray flux. The distance d and the ambient densities n are not known for all SNRs, so some assumptions were made in the cases in which these information were not available (see figure 2.11). The canonical value of 10^{51} erg was assumed for E_{SN}.

As it is clearly visible in figure 2.11, the estimates and upper limits on the CR energy content span more than three orders of magnitude, from a few 10^{49} erg to several 10^{52} erg. For the interacting SNRs that lie above the $\epsilon_{CR} = E_{CR}/E_{SN} = 1$ dashed line, the densities experienced by the CR particles in the molecular cloud interaction region are likely much larger than those used for this calculation. Hence, it is also likely that they are sites of hadronic interaction in dense environments. In contrast, young SNRs lie at or below this luminosity limit, but it is already known that IC processes contribute to their γ-ray luminosity. New information about distances and densities will provide more precise estimates of the CR content.

As a bottom line, the usual assumption of $\epsilon_{CR} = 0.1$, required in order for the Galactic SNR population to supply the CR flux observed at Earth, is compatible with the results of the *Fermi*-LAT SNR catalog.

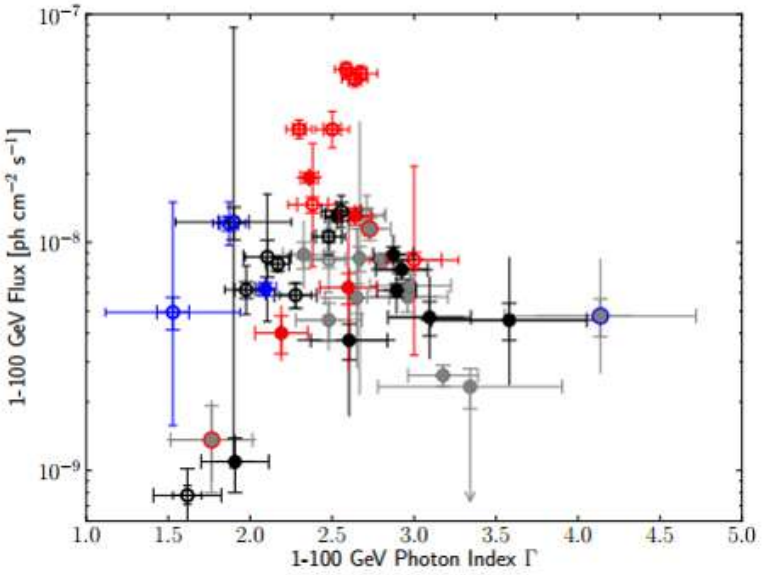

FIGURE 2.10: Scatter plot between γ-ray flux and spectral index of the SNRs detected in the first *Fermi*-LAT SNR catalog. Black: classified SNRs, grey: marginal candidates. Red: SNRs interacting with a molecular cloud, blue: young SNRs. Full circles: point-like sources, empty circles: extended sources. Error bars with caps: statistical error, without caps: systematic error [38].

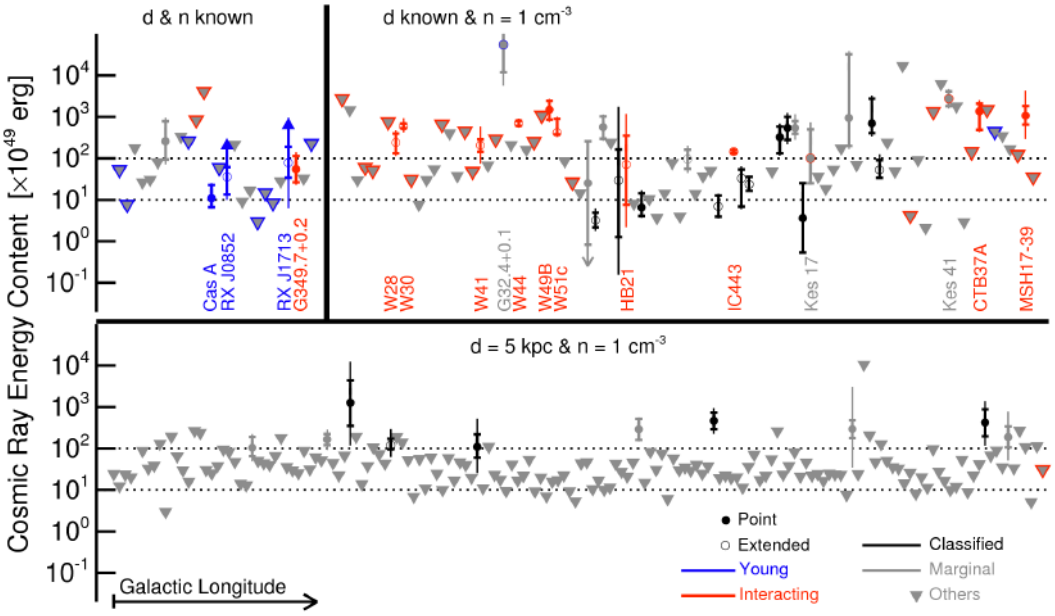

FIGURE 2.11: Estimates of the CR energy content for all Galactic SNRs studied in the first *Fermi*-LAT SNR catalog, divided into three categories each sorted by Galactic longitude: SNRs with known distance and density estimates (upper left panel); SNRs with known distances (upper right panel); and SNRs with unknown distance and density (lower panel). When the distance and the density were not known, they were fixed to the values of 5 kpc and 1 cm^{-3}, respectively. The two dashed lines indicate a CR energy content of 10 and 100% of the standard supernova (SN) explosion energy [38].

Chapter 3

γ-ray study of SNRs: the *Fermi* Large Area Telescope

3.1 The *Fermi*-LAT experiment

The Large Area Telescope (LAT) is the primary instrument onboard the *Fermi* Gamma-ray Space Telescope (or simply *Fermi*)[1], launched by NASA on June 11, 2008. The LAT is an imaging telescope detecting photons from a few tens of MeV up to a few TeV. The second instrument onboard *Fermi* is the γ-ray burst monitor (GBM), dedicated to the study of transient phenomena in the 8 keV - 40 MeV energy range, ensuring a good overlapping with the LAT sensitivity.

In this work, data from the LAT experiment were analyzed. In the next sections, details on the operating principles and performances of this instrument will be given.

3.1.1 The LAT on orbit

The *Fermi* satellite is on orbit around the Earth at an altitude of ≈ 565 km with an inclination of 25.6° with respect to the Equator. The *Fermi* observatory started the science operations on August 13, 2008.

[1] `http://fermi.gsfc.nasa.gov/`; formerly known as Gamma-ray Large Area Space Telescope (GLAST)

The primary observing strategy for *Fermi* is the scanning mode. Thanks to its large field of view, the LAT observes approximately the 20% of the sky at once and covers the whole sky every two orbits in approximately 3 hours. *Fermi* is occasionally operated in pointing mode to study interesting transient phenomena. Calibration runs are also periodically performed.

During its orbit, *Fermi* crosses a region known as South Atlantic Anomaly (SAA), which is an area in the southern hemisphere where the Van Allen radiation belt comes close to the Earth's surface at an altitude of about 200 km. This leads to a number of geomagnetically trapped energetic particles, increasing the particle flux of several orders of magnitude with respect to the rest of the orbit. This higher flux would cause the saturation of the instrument electronics and the exceedance of the safe operation limits, producing a rapid deterioration of the detector. For this reason, the LAT does not operate when crossing the SAA. The perimeter delimiting the SAA was conservatively defined prior to launch. As a result, the exposure time in the southern hemisphere is reduced with respect to the northern one and a fraction of about 13% of the total observation time is lost. [40]

3.1.2 The LAT detector

The LAT [41] is an imaging, pair-tracking γ-ray telescope, detecting photons from approximately 20 MeV up to a few TeV. It is made of a 4×4 array of towers, with a converter-tracker and a calorimeter module. A segmented anticoincidence detector (ACD) covers the array and a programmable trigger and the data acquisition system (DAQ) complete the instrument. Figure 3.1 provides a schematic illustration of the LAT.

Converter-tracker

High-energy γ-rays interact with matter mainly through production of e^+e^- pairs. The LAT converter-tracker modules (TKR) are made of 16 planes of high-Z material (tungsten) in order to promote the conversion of γ-rays into pairs, interleaved with 18 planes of silicon strip detectors revealing the charged particle trajectories. The last two silicon planes have no converter foils in order to accurately measure the entering point in the calorimeter. The thickness of the tungsten layers was optimized to maximize the conversion probability and minimise multiple scattering

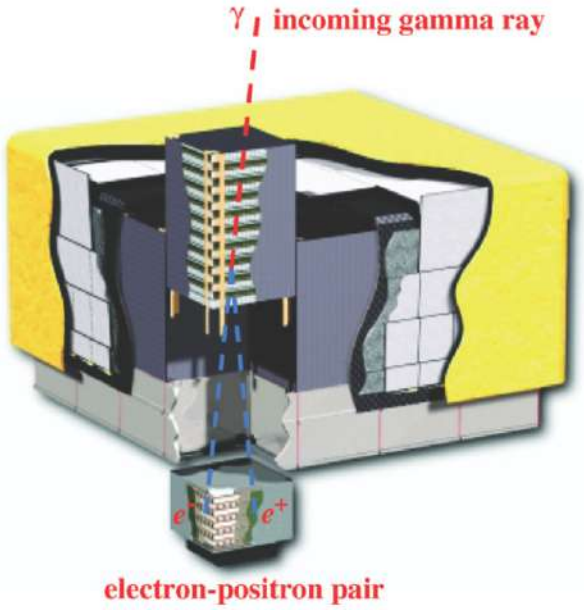

FIGURE 3.1: Schematic illustration of the Fermi-LAT apparatus. [41]

and bremsstrahlung energy losses of electrons and positrons. The first 12 layers have a thickness of 0.03 radiation lengths to maximize the angular resolution at low energies thanks to the limited Coulomb scattering (*front* section), while the last 4 layers have a thickness of 0.18 radiation lengths to maximize the conversion probability at high energies (*back* section). In order to obtain a two-dimensional reconstruction of the particle positions, each silicon plane is made of two layers (x and y) of single-sided silicon strip detectors. The aspect ratio of the tracker (height/width) is 0.4, allowing a large field of view (FoV) of 2.4 sr and ensuring that nearly all pair-conversion events will pass into the calorimeter. The choice of silicon-strip detectors gives the tracker a self-triggering capability, getting rid of the necessity of an external trigger. The self-triggering is given by the coincidence of signals coming from at least 3 consecutive silicon planes.

All LAT instrument subsystems employ technologies that do not use consumables, such as the gas of tracking spark chambers used in previous high-energy γ-ray telescopes. This allowed the LAT to work continuosly for more than 9 years without a significant drop in the performances.

Calorimeter

The main purpose of the calorimeter modules (CAL) is the reconstruction of the energy of the incoming γ-ray, by measuring the energy of the e^+e^- pair produced

in the TKR. Each CAL module is placed right below the corresponding TKR module and consists of 8 layers of 12 CsI(Tl), with a total depth of ~ 8.6 radiation lengths. Each crystal is read out by two photodiodes, one at each side, providing three spatial coordinates: two discrete coordinates from the location of the crystal in the array and the third coordinate given by measuring the light yield asymmetry at the ends of the crystal along its longitudinal dimension.

The segmentation gives both longitudinal and transverse information about the energy deposition pattern, allowing the electromagnetic shower imaging. This feature provides an important discriminator for the rejection of background cosmic-ray protons. In addition, it allows the estimate of the energy leakage and the reconstruction of the energy of photons up to a few TeV, whose cascades are not fully contained in the calorimeter and often lead to the saturation of some of the crystals.

Anti-coincidence Detector

The Anti-coincidence Detector (ACD) allows the discrimination of photons from the large background given by charged cosmic rays. It consists of plastic scintillators hermetically enclosing the tracker and the calorimeter, for a total active area of $8.3m^2$. The scintillators respond only to the passage of charged particles, allowing the photon identification. However, it is essential to avoid the "self-veto" effect, i.e. the rejection of γ-rays because of the *backsplash* on the ACD of secondary particles produced in the calorimeter, which becomes important for energies above ~ 10 GeV. For this purpose the ACD is segmented into 89 plastic scintillator tiles providing spatial information that can be correlated with the signal from tracker and calorimeter modules. Scintillation light from each tile is recorded by wavelength shifting fibers embedded in the scintillator and connected at their ends to two photomultiplier tubes (PMTs). A light micrometeoroid shield (0.39 g cm^2) protects the ACD from debris hitting the surface. A complete description of the ACD and its performance is given by [42].

An important remark is that the ACD system also permits the detection of charged particles, in particular electrons and positrons, allowing high precision measurements of the electron plus positron spectrum as already discussed in section 1.3.3 (see figure 1.7 and [9]). In this case, the ACD is used in coincidence with the TKR and CAL signals. Since *Fermi*-LAT experiment was not designed for the

detection of cosmic rays, it does not have a magnetic spectrometer and cannot directly measure the charge of the particles. Nevertheless, techniques based on the geomagnetic field have been developed to distinguish positrons and electrons (see [43]) in order to measure charge dependent quantities such as the positron fraction.

Data acquisition

The Data Acquisition System (DAQ) collects information and triggers from the subsystems (at a rate of 2-3 kHz) and provides the first onboard filter reducing the rate of downlinked events to approximately 500 Hz. In addition, an onboard data analysis pipeline is implemented to rapidly search for transient events. The DAQ connects the entire LAT instrument to the satellite through the spacecraft interface unit (SIU), which contains the control system of the spacecraft.

The tracker and calorimeter modules of each tower are interfaced by a Tower Electronics Module (TEM), generating tower-based triggers. A trigger occurs either if there is a coincidence of at least three silicon planes in a row or if the energy deposit in any of the calorimeter crystals exceeds a fixed threshold. Two different thresholds for low-energy and high-energy events are used.

At the entire instrument level a global unit collects signals from all the TEMs, provides an interface with the ACD and generates a global trigger. After triggering and building the events with the information received from the whole apparatus, it sends them to the two event processor units (EPUs).

The minimum read-out time per event is 26.5 μs, due to the transmission of the trigger signal between the different units. During the event read-out the different subsystems send a busy signal to the global unit, which generates the overall dead time and adds the information to the data stream transmitted to the ground.

Most of the events triggering the LAT are indeed background CRs. For this reason, the trigger is designed to minimise the dead time due to background events. The two EPUs implement the onboard filtering, reducing the background rate and maximising the efficiency for γ-ray detection. This allows the event rate within the bandwith available for the downlink. Nevertheless, all events exceeding a threshold of raw energy deposited in the calorimenter of 20 GeV are transmitted to the Earth for the off-line analysis, since their rate is low.

3.1.3 The LAT data

Event classification

Event classification aims at selecting the best estimates of the event direction and energy and determining their accuracy, as well as at drastically reducing the backgrounds in the final data sample. The background rejection is a fundamental task since the background events triggering the LAT exceed by 10^5 the celestial γ-ray flux. The onboard filter reduces the rate of triggered events to match the available bandwith for the downlink to the Earth, reaching a signal-to-noise ratio of 1:300. The background rejection performed with the offline analysis further reduces the background contamination.

Depending on the scientific objective of the data analysis, different performances in terms of background contamination and photon detection efficiency are required. For this reason different photon classes are defined. Nevertheless, all event classes have a residual background contamination. The reducible background is given by events which are erroneously classified as γ-rays and could be in principle identified and eliminated. The irreducible background is due to charged particles interacting with the dead materials surrounding the instrument and producing a real γ-ray, which is detected by the LAT. Irreducible events constitute the majority of residual backgrounds in the purest classes and cannot be completely eliminated.

After the event is analysed, a list of predefined quantities, such as energy and arrival direction, is associated with the photon event, as well as a flag indicating the event class. A full list of these quantities is shown in figure 3.2. *Fermi*-LAT photon data are publicly available through the Fermi Science Support Center (FSSC) [2], together with the orbital history of the telescope.

Instrument Response Functions (IRFs)

Data analysis cannot be performed without a detailed description of the instrument performances, which is fulfilled through the Instrument Response Functions (IRFs).

The IRFs are generated performing a full simulation of the instrument, using the software Geant4. A large number of γ-rays and background particles with

[2] `https://fermi.gsfc.nasa.gov/ssc/data/`

Col	Name	Format[Units](Range)	Comment
1	ENERGY	E [MeV] (0.:10000000.)	energy of event
2	RA	E [deg] (0.:360.)	right ascension (J2000) of event
3	DEC	E [deg] (-90.:90.)	declination (J2000) of event
4	L	E [deg] (0.:360.)	Galactic longitude of event
5	B	E [deg] (-90.:90.)	Galactic latitude of event
6	THETA	E [deg] (0.:180.)	inclination angle of event in instrument coordi
7	PHI	E [deg] (0.:360.)	azimuthal angle of event in instrument coordina
8	ZENITH_ANGLE	E [deg] (0.:180.)	zenith angle of event
9	EARTH_AZIMUTH_ANGLE	E [deg] (0.:360.)	Earth azimuth (from north to east) of event
10	TIME	D [s] (0.:10000000000.)	Mission Elapsed Time
11	EVENT_ID	J (0:2147483647)	ID number of orlginal event
12	RUN_ID	J (0:2147483647)	Run number of original event
13	RECON_VERSION	I (0:32767)	version of event reconstruction software
14	CALIB_VERSION	3I	versions of calibration tables for the ACD, CAL
15	EVENT_CLASS	32X (0:32767)	event class: 0, 1, 2,...
16	EVENT_TYPE	32X (0:32767)	event types encoded as bit array
17	CONVERSION_TYPE	I (0:32767)	type of conversion: 0=Front converting, 1=Back
18	LIVETIME	D [s] (0.:10000000000.)	Accumulated livetime since mission start
19	DIFRSP0	E (0.:1.0E+38)	Diffuse response component
20	DIFRSP1	E (0.:1.0E+38)	Diffuse response component
21	DIFRSP2	E (0.:1.0E+38)	Diffuse response component
22	DIFRSP3	E (0.:1.0E+38)	Diffuse response component
23	DIFRSP4	E (0.:1.0E+38)	Diffuse response component

FIGURE 3.2: Table summarising the predefined quantities associated to each photon event.

different energy and inclination angle with respect to the z-axis of the instrument are simulated. The background rejection and event reconstruction algorithms are then applied in order to quantify how many γ-rays are detected and how accurate the reconstructed direction and energy are.

The IRFs are defined as a function R of the true photon energy E' and direction $\hat{u}'$, the measured photon energy E and direction $\hat{u}$ and time t, so that the differential count rate measured by the instrument is given by the convolution of the true differential flux per unit area at the detector with the IRFs:

$$\frac{dN}{dtdEd\hat{u}}(E,\hat{u},t) = \int dE'd\hat{u}'R(E,\hat{u}|E',\hat{u}';t)\frac{dN}{dtdE'd\hat{u}'dS}(E',\hat{u}',t). \tag{3.1}$$

The function R can be factorized in three independent factors:

$$R(E,\hat{u}|E',\hat{u}';t) = A(E',\hat{u}') \times P(\hat{u}|E',\hat{u}') \times D(E|E',\hat{u}'), \tag{3.2}$$

where:

- $A(E',\hat{u}')$ is the effective area, which is the detection efficiency for photons of true energy E' and arrival direction $\hat{u}'$ expressed as an area;
- $P(\hat{u}|E',\hat{u}')$ is the Point Spread Function (PSF), which represents the probability that a photon with energy E' and arrival direction $\hat{u}'$ has a reconstructed direction $\hat{u}$;

- $D(E|E', \hat{u}')$ is the energy dispersion, which is the probability density that a photon with energy E' and arrival direction $\hat{u}'$ has a reconstructed energy E.

An additional scaling factor $T(t)$ can be added to the IRFs to account for temporal variations, such as instrument failures or the deterioration of instrument components. The lack of consumables makes the LAT performance very stable and therefore this term is negligible.

Data releases

Over the course of the mission, the event-level analysis has been periodically updated, taking advantage of the improvement in the understanding of the LAT performances and on-orbit operation. Since launch, four major data releases have been produced, called *Passes*, accompanied by the corresponding sets of IRFs.

The first release, called `Pass 6`, was built prior to launch using Monte Carlo simulation and calibration data taken on the LAT test units [41]. The first version of the IRFs (`P6_V1`) proved to be inaccurate, due to the presence of the so called *ghost* events, which were not expected and not included in the simulations. These events occur when a γ-ray hits the LAT immediately after a background event. The LAT is triggered while the energy released by the background particle in the sensitive volumes is still being collected. In this case the signals coming from both the photon and the background particle are transmitted to Earth and the reconstruction algorithm is likely to discard these perfectly good events, leading to a degradation of the LAT performances. A schematic representation of a ghost event is given in figure 3.3. In order to account for this effect and calculate the correct IRFs, the *ghost* events were included in the Monte Carlo simulations, without changing the event reconstruction algorithm and producing the `P6_V3` version of instrument response [44].

The second major release, known as `Pass 7`, took advantage of the first years of real data to study other on-orbit effects. These effects were included in the data reduction and in the Monte Carlo simulation to obtain corrected responses. Data released after 2011 August 1 were based on `Pass 7` [45].

In 2013, a revised version of `Pass 7` data, known as `Pass 7 Reprocessed` (`P7REP`), was produced adopting updated calibration constants, which took into account a

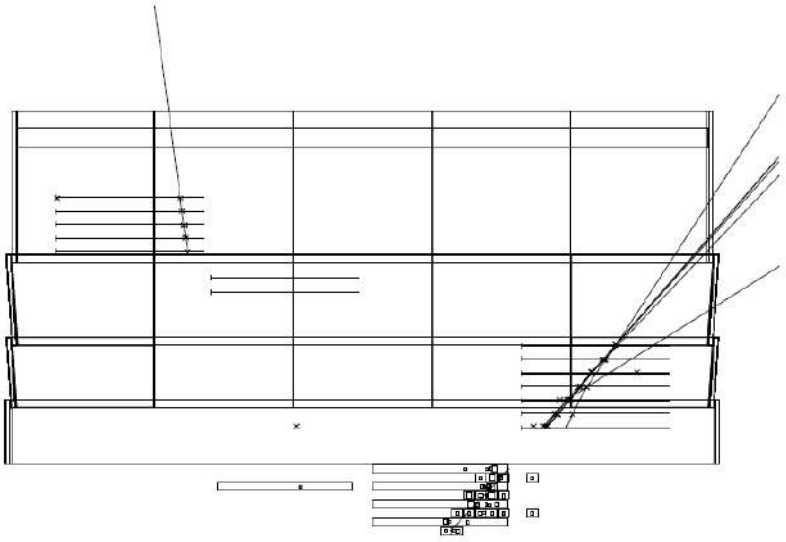

FIGURE 3.3: Example of a *ghost* event in the LAT. On the right a candidate γ-ray event, on the left a *ghost* track resulting from an accidental time coincident background event [44].

1% per year degradation in the calorimeter light yield. Furthermore, a significant improvement in the reconstruction of the calorimenter position resulted in a better angular resolution of the instrument, especially at high energies [46].

Finally, in June 2016 a new version of LAT data was made public, called `Pass 8` [47]. This event release is based on completely new event reconstruction algorithms and updated simulations, which significantly enhance the LAT performances. The major improvements are listed below.

- A deep study of *ghost* events was performed using the huge amount of data taken by the LAT in the first years of operation. These events were fully included in the instrument simulation by adding real background events to the Monte Carlo simulations. The event reconstruction was optimized to deal with this effect and avoid discarding the "good" γ-rays accompanied by a *ghost*, resulting in an increased effective area of the instrument.

- Simulation of the LAT apparatus was updated, adopting a new version of the Geant4 software used to simulate the instrument. This led to a modification of the event selection cuts which increased the LAT acceptance over the entire energy range.

- New pattern recognition algorithms were developed, allowing the track reconstruction to be independent on the calorimenter and reducing the track confusion due to the *backsplash*.
- The description of the energy leakage and crystal saturation in the calorimeter was improved, allowing a better energy reconstruction and increasing the effective area especially at high energy (above 1 TeV).
- Background rejection was also enhanced, thanks to the improvement of the association between tracks and ACD tiles and to new Boosted Decision Trees algorithms with better separation power between photons and charged particles.

Event classes and types

As already stated in the previous paragraph, photon events are divided in different classes, depending on the requested purity of the data set.

Prior to launch, three classes were defined for the first data release (`Pass 6`). The `TRANSIENT` class, suitable for studying localised, intense, transient phenomena, had the largest efficiency but a residual background at the level of the γ-ray detection rate (< 2 Hz). The `SOURCE` class had a better background rejection and was primarily intended for point-source analysis and diffuse analysis at galactic latitudes lower than 30°. It was optimized so that the background contamination was similar to the expected rate of extragalactic γ-rays in the entire field of view (< 0.4 Hz). The `DIFFUSE` class was the purest one, with a background-rejection factor of the order of 10^6. It was designed in particular for diffuse γ-ray emission studies.

In the most recent data release, `Pass 8`, many more photon classes were introduced (from `TRANSIENT` to `ULTRACLEANVETO`) with increasing quality of the reconstructed photon at the expenses of the photon efficiency. The `SOURCE` class is the one recommended for analysis of point sources, especially in the Galactic plane.

Within each photon class, events are divided in "event types". In previous releases, events were classified in `FRONT` and `BACK`, depending on the location of the tracker in which the photon conversion occurred. In the `Pass 8` release, two new event classification were introduced, based on the quality of the reconstruction of the

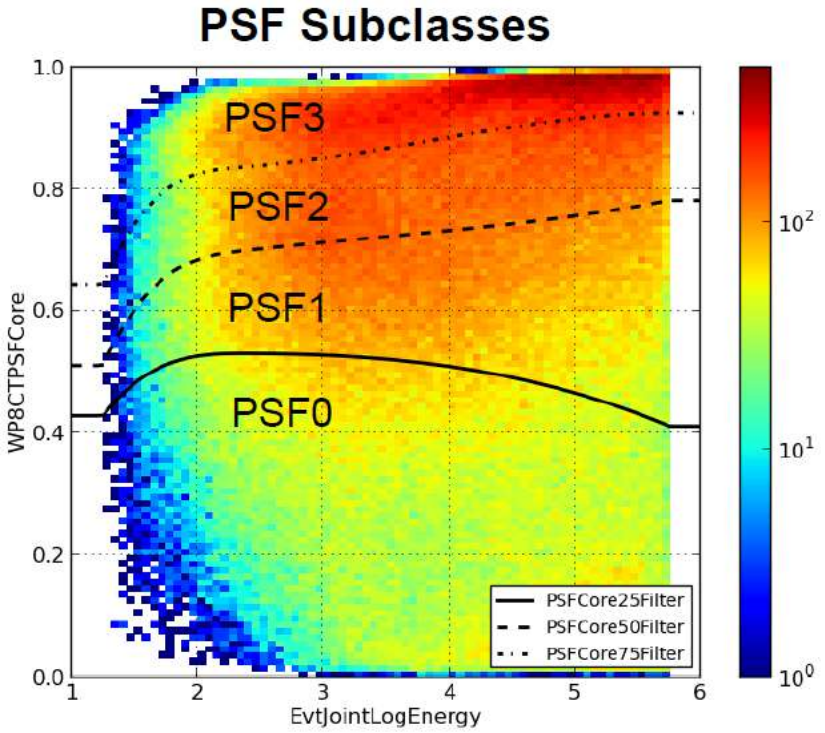

FIGURE 3.4: `WP8CTPSFCore` variable as a function of energy used to classify events in PSF event types. Black lines represent the energy dependent cuts applied to classify events. The image is for illustrative purpose only and does not correspond to the actual selection applied to the data. Image courtesy of Dr. Matthew Wood.

direction (`PSF` types) or energy (`EDISP` types). For each classification, an event-level variable representing the quality of the reconstructed direction or energy is used to divide the data in four types (named from 0 to 3) with increasing quality. The cuts are defined so that each event type has approximately the same effective area, i.e. each event type contains the 25% of the total statistics. As an example, figure 3.4 shows the event distribution for the variable `WP8CTPSFCore` as a function of energy, which is used to divide events in `PSF` types. The black lines represent the energy dependent cuts applied to classify the events. The cuts are optimized such that the fraction of events in each `PSF` type is the same, keeping the effective area of each event type approximately equal to the 25% of the total effective area at all energies.

`Pass 8` performances

Figures from 3.5 to 3.9 summarise the LAT `Pass 8` performances for the `SOURCE` event class, known as `P8R2_SOURCE_V6`, which is the latest version of IRFs publicly

available on the FSSC [3]. Figure 3.5 shows the effective area as a function of energy for normally incident photons and as a function of incidence angle (called *off-axis angle*) for 10 GeV photons. The relevant quantity is the effective area integrated over the FoV, called acceptance. Figure 3.6 shows the intrinsic acceptance, regardless of orbital characteristics. Since the effective area depends on the *off-axis angle*, as shown in figure 3.5b, the acceptance for a given dataset is obtained weighting the effective area with the time fraction that the LAT spends observing a given direction at a certain *off-axis angle*. This calculation is performed directly during the analysis procedure, since depends on the region of the sky observed and on the spacecraft orbital history.

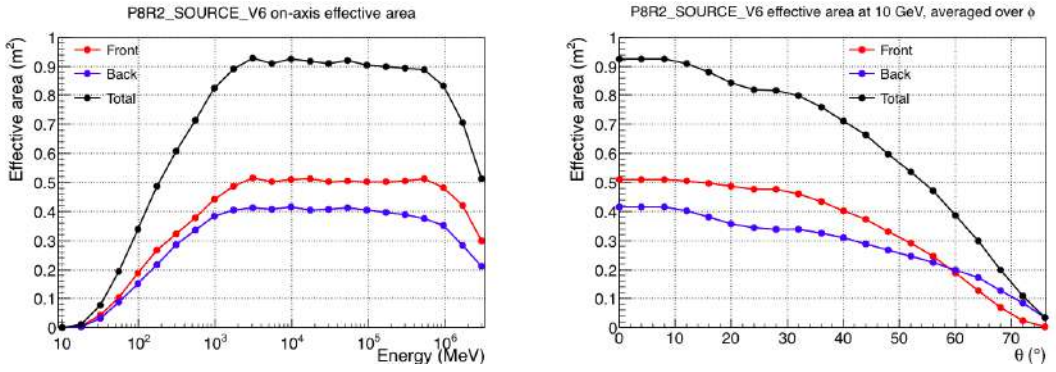

(A) (B)

FIGURE 3.5: The LAT effective area for the `P8R2_SOURCE_V6` IRFs as a function of energy for normally incident photons (a) and of the incidence angle for 10 GeV photons (b). The curves correspond to *front*-converting events (red), *back*-converting events (blue) and total (black).

Figure 3.7 shows the 68% and 95% containment angles of the acceptance-weighted PSF as a function of energy. The PSF strongly depends on energy, being much larger at low energy where the Coulomb scattering in the tracker significantly affects the particle trajectories. The PSF is a peaked distribution around the true position, as one would expect, but it has larger tails with respect to an ideal Gaussian distribution, especially at energies above 10 GeV. Figure 3.8 shows the 68% containment angle for the four `PSF` types, showing the improvement obtained for the best evet types (`PSF2` and `PSF3`). The functional form of the PSF is derived and adapted from XMM experiment, usually referred to as "King" function:

$$K(x,\sigma,\eta) = \frac{1}{2\pi\sigma^2}\left(1-\frac{1}{\eta}\right)\left[1+\frac{x^2}{2\eta\sigma^2}\right]. \tag{3.3}$$

[3] All performance plots are taken from `https://www.slac.stanford.edu/exp/glast/groups/canda/lat_Performance.htm`. For more details on the IRFs description see `https://fermi.gsfc.nasa.gov/ssc/data/analysis/documentation/Cicerone/Cicerone_LAT_IRFs`.

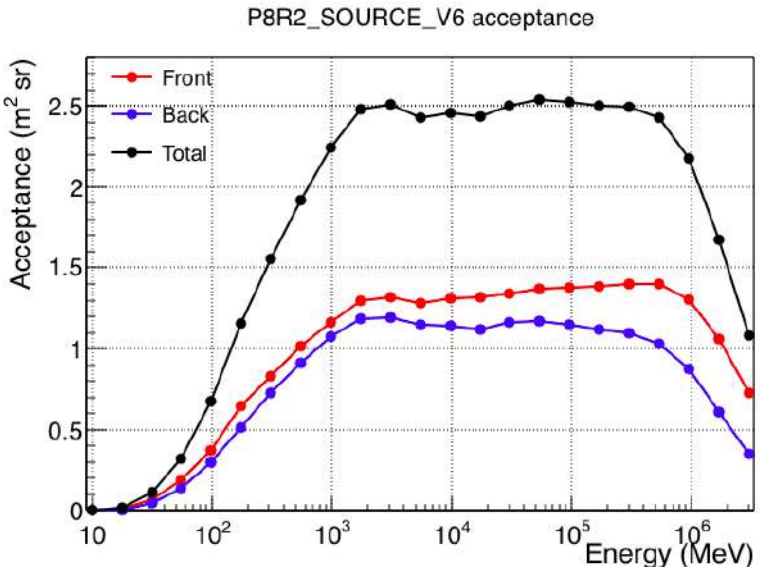

FIGURE 3.6: The LAT acceptance for the `P8R2_SOURCE_V6` IRFs as a function of energy. The curves correspond to *front*-converting events (red), *back*-converting events (blue) and total (black).

In order to allow for a tail in the distribution, the PSF is actually built as the sum of two King functions properly weigthed and with independent parameters, called K_{core} and K_{tail}. The parameters $\sigma_{core/tail}$ and $\eta_{core/tail}$ and the relative fraction of the two King functions are fitted from the Monte Carlo simulations of the instrument. The fit is performed independently in bins of energy and *off-axis angle*, deriving a set of parameters for each bin, which are then properly used in the data analysis. More details are available on the FSSC [4].

Finally, figure 3.9 shows the energy resolution $\Delta E/E$, defined as the 68% containment of the reconstructed photon energy, as a function of energy. It is better than 15% over most of the energy range in which the LAT is sensitive. At low energy it gets worse because of higher energy losses in the tracker, while at high energy a poor longitudinal containment of the electromagnetic shower in the calorimeter and the saturation of most of the crystals make difficult the energy reconstruction. Figure 3.10 shows the energy resolution for the four `EDISP` types, showing also in this case the improvement obtained for the best selections (`EDISP2` and `EDISP3`). More details on how the energy dispersion is parametrized in the LAT IRFs are available on the FSSC [5].

[4] `https://fermi.gsfc.nasa.gov/ssc/data/analysis/documentation/Cicerone/Cicerone_LAT_IRFs/IRF_PSF.html`

[5] `https://fermi.gsfc.nasa.gov/ssc/data/analysis/documentation/Cicerone/Cicerone_LAT_IRFs/IRF_E_dispersion.html`

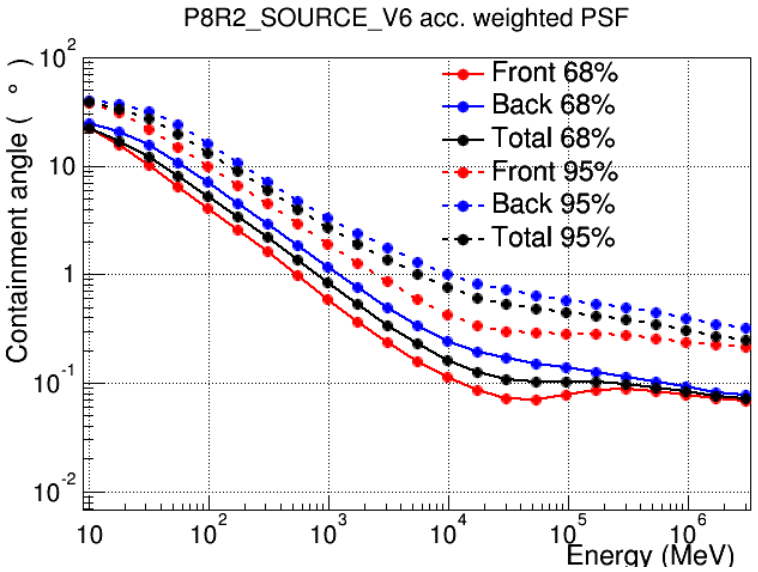

FIGURE 3.7: The 68% and 95% containment angles for `P8R2_SOURCE_V6` PSF as a function of energy. The curves correspond to *front*-converting events (red), *back*-converting events (blue).

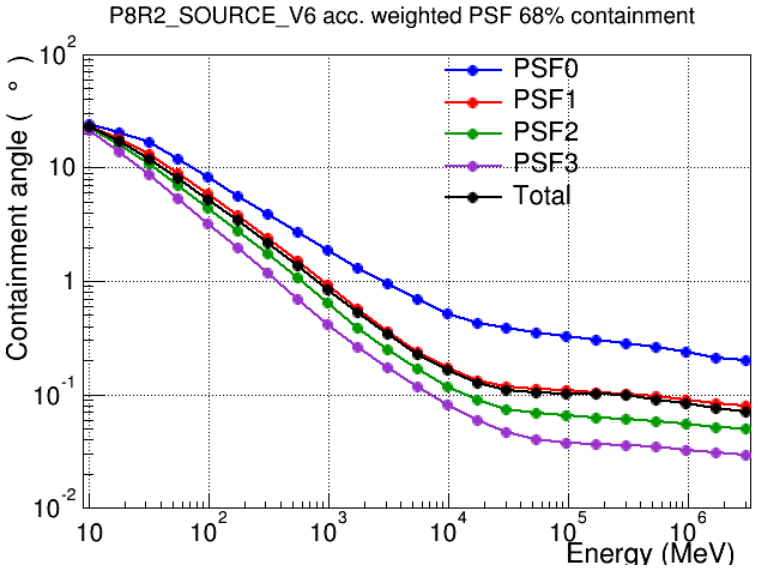

FIGURE 3.8: The 68% containment angle of `P8R2_SOURCE_V6` PSF as a function of energy for the four `PSF` types. The black line (total) is the same shown in figure 3.7.

Figure 3.11 shows a comparison of the latest `Pass 8` acceptance with respect to the previous `P7REP` reconstruction technique. At central energies, the acceptance is approximately 25% higher for `Pass 8`, while at low energy and high energy the improvement is even larger.

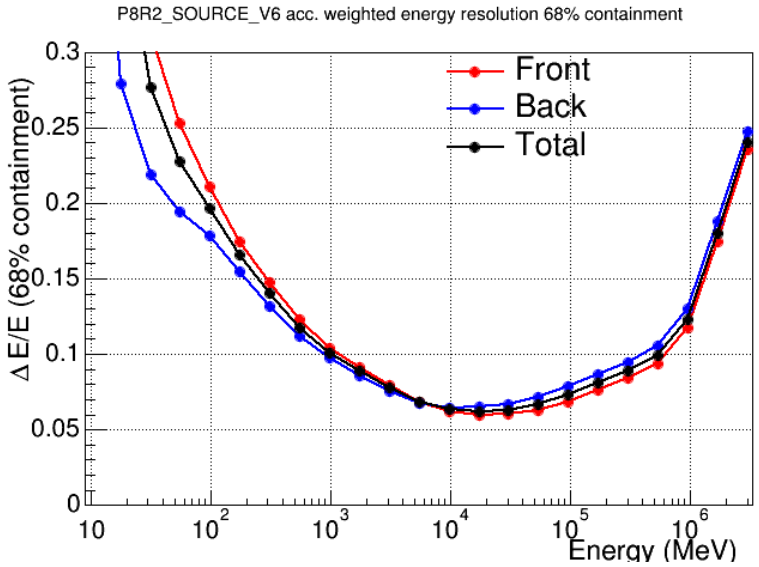

FIGURE 3.9: $\Delta E/E$, defined as the 68% containment of the reconstructed photon energy, for the `P8R2_SOURCE_V6` IRFs as a function of energy. The curves correspond to *front*-converting events (red), *back*-converting events (blue).

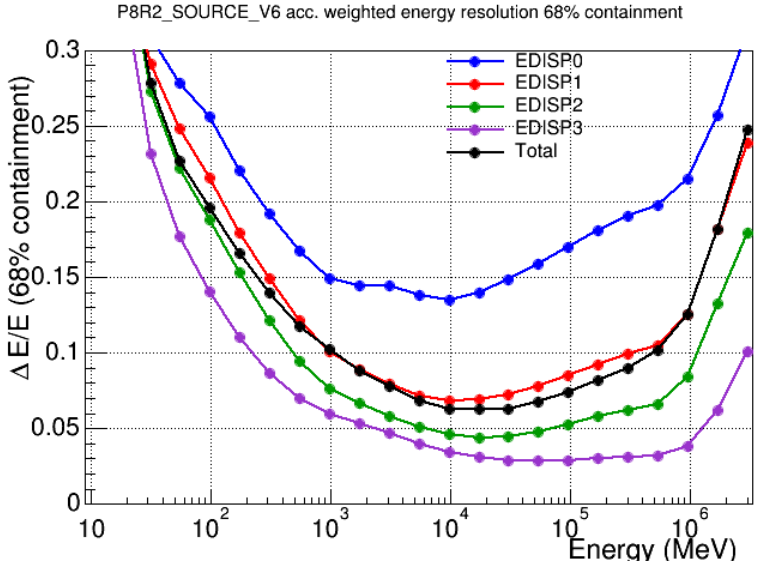

FIGURE 3.10: $\Delta E/E$, defined as the 68% containment of the reconstructed photon energy, for the `P8R2_SOURCE_V6` IRFs as a function of energy for the four `EDISP` types. The black line (total) is the same shown in figure 3.9.

3.2 *Fermi*-LAT analysis

Once data have been collected, a detailed analysis of their spatial and spectral distribution must be performed in order to obtain information of astrophysical interest. However, in most cases it is not possible to isolate a specific source in high-energy γ-rays, because of the presence of a bright and structured background

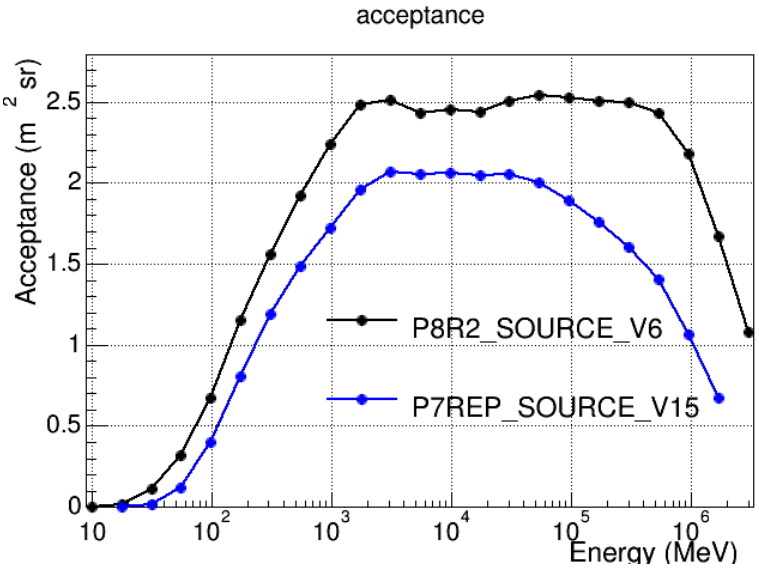

FIGURE 3.11: Comparison of the instrument acceptance of the `Pass 8` and `P7REP SOURCE` classes.

given by the interstellar emission. Furthermore, the angular resolution, strongly varying with energy, is often poor compared to other wavelengths and in most cases is not sufficient to observe the extension of the source, which appears as a point source. Therefore, statistical techniques have to be applied to study the γ-ray sky.

3.2.1 Likelihood analysis

The method adopted is the likelihood maximisation, based on the Poisson statistics used to describe the photon count distributions. Given the huge number of photons which are usually present in the entire ROI, the analysis is usually performed dividing the observed region of the sky in pixels and energy bins, performing a *binned* likelihood analysis. If the statistic is low an *unbinned* analysis can be performed, allowing each single photon to contribute directly to the likelihood.

Likelihood definition for binned analysis

In the case of a *binned* analysis, data are divided in bins and compared to the expected value of counts in the same bins. In general, the entries of a histogram

are distributed according to a multinomial probability density function:

$$f_{\text{hist}}(n_i;\nu_i) = \frac{n_{\text{tot}}!}{\prod_i n_i!}\left(\frac{\nu_i}{n_{\text{tot}}}\right)^{n_i}, \tag{3.4}$$

where n_i and ν_i are the observed and expected counts in bin i respectively and $n_{\text{tot}} = \sum_i n_i$ is the total number of events.

However, if n_{tot} is a random variable as well, following a Poisson distribution with mean value $\nu_{\text{tot}} = \sum_i \nu_i$, the joint p.d.f. is the product of a Poisson distribution and the multinomial distribution defined in previous equation:

$$f_{\text{hist}}(n_i;\nu_i) = \frac{\nu_{\text{tot}}^{n_{\text{tot}}} e^{-\nu_{\text{tot}}}}{n_{\text{tot}}!} \times \frac{n_{\text{tot}}!}{\prod_i n_i!}\left(\frac{\nu_i}{n_{\text{tot}}}\right)^{n_i}. \tag{3.5}$$

which gives, using the definition of ν_{tot} and n_{tot}:

$$f_{\text{hist}}(n_i;\nu_i) = \prod_i \frac{\nu_i^{n_i}}{n_i!} e^{-\nu_i}. \tag{3.6}$$

The p.d.f. derived is equivalent to the one of independent Poisson measurements (the bin counts in this case).

See [48, Chapter 6.10] for more details.

Maximum Likelihood for *Fermi*-LAT data

Let $M(E', \hat{u}', t; \alpha_k)$ be the differential flux per unit area describing the observed region of the sky as a function of the true energy of the photons E', their true arrival direction $\hat{u}'$ and the time of observation t. $\{\alpha_k\}_{k=1,..,m}$ are the parameters describing the model, whose best-fit values are determined through the likelihood maximisation. M usually includes the "known" (i.e. already detected in previous studies) sources in the region of the sky under investigation, plus possible additional new sources. When steady sources are considered, M can be considered constant in time.

Using the IRF definition in equation (3.2), the observed count rate J can be derived using the following expression:

$$J(E, \hat{u}; \alpha_k) = \int dE' d\hat{u}' R(E, \hat{u}|E', \hat{u}') M(E', \hat{u}'; \alpha_k). \tag{3.7}$$

J is a function of the reconstructed energy and arrival direction of the photon.

The total number of counts expected in a solid angle Ω, in the energy range (E_1, E_2) and the time of observation (t_1, t_2), is obtained by integration over E, $\hat{u}$ and t:

$$\Lambda(\alpha_k) = \int_{t_1}^{t_2} dt \int_{E_1}^{E_2} dE \int_{\Omega} d\hat{u}\ J(E, \hat{u}; \alpha_k). \tag{3.8}$$

Given a set of values of $\{\alpha_k\}_{k=1,\dots,m}$, $\Lambda(\alpha_k)$ represents the true value of counts, i.e. the expectation value of the Poisson distribution.

Using equation 3.6, the likelihood is the product of the probabilities of each pixel i and each energy bin j:

$$\mathcal{L} = \prod_{i,j} \mathcal{P}(N_{i,j}; \Lambda_{i,j}(\alpha_k)), \tag{3.9}$$

where $\mathcal{P}(n; \lambda)$ is a Poisson distribution with mean value λ.

The likelihood $\mathcal{L}$ has to be maximised with respect to the model parameters, in order to find the best estimates for $\{\alpha_k\}_{k=1,\dots,m}$.

It is convenient to consider the natural logarithm of the likelihood:

$$\ln \mathcal{L} = \sum_{i,j} N_{i,j} \ln \Lambda_{i,j}(\alpha_k) - \sum_{i,j} \Lambda_{i,j}(\alpha_k) - \sum_{i,j} \ln(N_{i,j}!). \tag{3.10}$$

Since the last term does not depend on the model parameters, it can be negleted and the log-likelihood becomes:

$$\ln \mathcal{L} = \sum_{i,j} N_{i,j} \ln \Lambda_{i,j}(\alpha_k) - \sum_{i,j} \Lambda_{i,j}(\alpha_k) = \sum_{i,j} N_{i,j} \ln \Lambda_{i,j}(\alpha_k) - \Lambda_{\rm tot}(\alpha_k), \tag{3.11}$$

where $\Lambda_{\rm tot}(\alpha_k)$ is the total expected counts.

The likelihood profile around the maximum gives information about the errors on the best-fit values. The statistical error on the parameters is defined as the variations of the parameters that causes a drop of the log-likelihood maximum value of 0.5:

$$\ln \mathcal{L}(\alpha_k \pm \sigma_{\alpha_k}) = \ln \mathcal{L}(\bar{\alpha}_k) - 0.5, \tag{3.12}$$

where $\bar{\alpha}_k$ is the best-fit value that maximise the log-likelihood.

If the statistics is sufficiently high, the log-likelihood around the maximum is well described by a parabola (and the likelihood by a Gaussian distribution), resulting in equal positive and negative errors (*symmetric* errors). In this case, the error can be evaluated with good approximation using the second derivative of the log-likelihood with respect to the parameters. This method is computationally faster than building the profile of the log-likelihood, which is an m dimensional hyper-ellipsoid in the general case.

However, in case of low statistics or faint sources, the symmetric approximation might be wrong. For this reason, an estimate of the *asymmetric* errors on a given parameter α_k is obtained by changing the value of this parameter around the best-fit value and re-fitting the others. This method is in most cases computationally intensive. See [48, Chapter 9.6-9.7] for more details.

Significance of a source

In order to estimate if a source is significant, the likelihood ratio test (LRT) can be used to quantitatively compare the model adopted with the one in which the source is removed.

Let $M_0(\{\alpha_k\}_{k=1,..,h})$ be a simpler model than the one considered in the previous section, that means $h < m$. For example, M_0 can be obtained fixing the values of $m - h$ parameters of M. The *test statistics* is defined as:

$$\mathrm{TS} = 2(\ln \bar{\mathcal{L}} - \ln \bar{\mathcal{L}}_0), \tag{3.13}$$

where $\ln \bar{\mathcal{L}}$ and $\ln \bar{\mathcal{L}}_0$ are the maximum values of the log-likelihood found using the model M and M_0, respectively. The Wilk's theorem [49] states that the TS-value is distributed asymptotically as a χ^2 with $m-h$ degrees of freedom. When the TS is large the M_0 hypothesis is rejected and the complete model M is adopted. The confidence level at which the full model M describes data better than the simpler model M_0 is

$$\text{c.l.} = \int_0^{\mathrm{TS}} \chi^2_{m-h}(s)ds, \tag{3.14}$$

being $\int_{\mathrm{TS}}^{+\infty} \chi^2_{m-h}(s)ds$ the chance probability that the test statistics is larger than the obtained value.

If M_0 is a model obtained removing a given source from M, the TS value provides the level of significance at which that source is observed. If $m - h = 1$, one finds that $\sqrt{TS}$ is approximately the significance expressed in σ units.

In an analogue way, the same method can be used to compare different spatial or spectral models for a given source. In the former case, the quantity TS_{ext} is used, such that the source is described as extended in M and as point-like in M_0. In the latter, the TS_{curv} is defined comparing a spectral model which includes a spectral curvature M with a simpler one M_0, as it will be explained in the next sections.

Upper limits

If a source proves to be below the detection threshold, an upper limit can be calculated on its flux, according to the likelihood profile. A likelihood scan is perfomed varying the normalization parameter of the investigated source, until an increase in log-likelihood corresponding to the desired confidence level is reached. For example, an increase in log-likelihood of 1.35 corresponds to a 95% confidence level upper limit. See [5] for more details on the likelihood profile upper limit estimate.

3.2.2 Data format and data preparation

The online data analysis and the event reconstruction process produce tables of events containing a list of predefined quantities for each event (see figure 3.2), stored in files in FITS format [6].

The LAT collaboration developed a set of tools, called *Fermi Science Tools*, to perform high level data analysis. They are publicly available through the FSSC [7]. The *Science Tools* include tools to rapidly simulate LAT observations, perform temporal analysis of pulsars, select and explore LAT data and perform the likelihood analysis described in section 3.2.1.

The data selection tools allow the user to select events according to one or more of the quantities describing the events. In order to study a specific source in the sky, photons from a region surrounding the position of this source must be selected.

[6] FITS stands for Flexible Image Transport System. See `https://fits.gsfc.nasa.gov`.
[7] `https://fermi.gsfc.nasa.gov/ssc/data/analysis/documentation/Cicerone/`

Cuts on the energy range and time interval can also be performed. As already discussed above, events are divided in classes and types. Therefore, events from a specific class and/or type can be selected. Another type of selection regards the contamination coming from γ-rays produced in the interaction of cosmic rays with the Earth's atmosphere, called *Earth's limb*. This background is very bright, but such photons can be easily discarded thanks to their arrival direction. For this purpose a cut on the zenith angle, which is the angle between the incoming photon direction and the direction perpendicular to the Earth's surface, is applied, eliminating all photons having a too large zenith angle. This cut is usually performed according to specific studies developed by the LAT collaboration, which resulted in the definition of energy-dependent cuts that mantain the Earth's limb contamination below a given threshold. The tool which is used to perform all these cuts is called `gtselect`.

Once data have been selected, the correct time intervals must be calculated. The `gtmktime` tool performs the calculation of the so called *good time intervals* (GTIs), which are the time ranges when the LAT was actually able to collect data. Only data taken in these GTIs can be considered valid. GTIs are used by other tools to correctly calculate the exposure of the LAT. The `gtmktime` tool performs cuts based on the spacecraft position, for example selecting times when the spacecraft is not in the Southern Atlantic Anomaly (SAA). For this purpose, it needs the spacecraft file as input, containing all the information about the LAT navigation, such as position and orientation as a function of time.

3.2.3 Fitting procedure

The likelihood analysis is implemented through a series of subsequent steps.

The first step consists of the evaluation of the livetime of the LAT, which is the time that the detector spent observing each position of the sky. The tool that performs this calculation is `gtltcube`, which calculates the livetime as a function of the sky direction and of the off-axis angle. The off-axis angle dependence is important since the LAT IRFs depend on this angle, as already seen in section 3.1.3.

The next step is the evaluation of the exposure for the region of the sky under investigation, which has to be divided in pixels of arbitrary dimensions. The exposure is obtained multiplying the livetime calculated using `gtltcube` by the

effective area of the instrument parametrised in the IRFs. Given its dependence on the off-axis angle, the exposure is obtained weighting the effective area with the livetime calculated at each value of the off-axis angle:

$$\epsilon_{\rm pix}(E) = \int {\rm lt}_{\rm pix}(\theta) A_{\rm eff}(E) d\theta, \tag{3.15}$$

where θ is the off-axis angle. The tool performing this calculation is called `gtexpcube2`.

The last step before the fit is the evaluation of the expected and observed counts for each pixel and energy bin. The observed counts are evaluated using the `gtbin` tool, which creates a 3-D map (two spatial coordinates plus one dimension for the energy binning) of the observed photons.

The expected counts, according to equation (3.7) and (3.8), are evaluated through the convolution of the model flux of the region of the sky analysed with the IRFs. The model is defined as the sum of different sources, described in a file in the XML (eXtensible Markup Language) format. Each source is factorized in a spatial and a spectral shape:

$$M(\hat{u}, E) = M_{\rm spat}(\hat{u}) M_{\rm spec}(E). \tag{3.16}$$

The spatial models allow the definition of point-like sources, i.e. sources whose size is too small to be resolved by the LAT, as well as extended sources, which can be described by simple geometrical models (for example disk or Gaussian shapes) or by more complex structures usually derived with the help of multi-wavelength data. This last case is for example what happens for the diffuse background definition. Spectral models are mostly based on the power-law spectrum, which describes the typical energy dependence of non-thermal emission processes. Models that allow the presence of spectral features are also included. Some examples are the broken power-law, the log-parabola[8], the power-law with exponential cut-off. A complete list of spatial and spectral models and their functional definition is available in the *Science Tools* documentation on the FSSC [9].

[8]Log-parabola is a functional form introduced to describe curved spectra which cannot be reproduced with an exponential cut-off. The functional form is given by:

$$N(E) = N_0 \left(E/E_b\right)^{\alpha + \beta \ln(E/E_b)}, \tag{3.17}$$

where α is the spectral index, β is the index of the curvature and E_b is the energy break.

[9]`https://fermi.gsfc.nasa.gov/ssc/data/analysis/scitools/source_models.html`

The factorization of the source models allows a two-step integration for equation (3.7). In the first step, the spatial integration is performed. The spatial part of the model is multiplied by the exposure previously calculated and convolved with the LAT PSF. This is performed at different values of energy, in particular at the energy boundaries defined for the data binning. For each pixel and energy:

$$S_{\rm pix}(E) = \int PSF(\hat{u}|\hat{u}', E)\epsilon(\hat{u}, E)M_{\rm spat}(\hat{u}', E)d\hat{u}', \tag{3.18}$$

where $M_{\rm spat}$ defines the spatial shape of the sources and ϵ is given by equation 3.15.

This integration is perfomed only once, especially for sources whose spatial parameters are not fitted. This task is fulfilled by the tool `gtsrcmaps` independently for each source in the model. The different contributions are then added together during the fit.

The second step involves integration over energy. The quantity defined in equation (3.19) is multiplied by the spectral part of the model and convolved with energy dispersion matrix:

$$\Lambda_{\rm pix}(E) = \int D(E|E')S_{\rm pix}(E)M_{\rm spec}(E)dE'. \tag{3.19}$$

This integration is perfomed during the fit procedure, since spectral parameters are usually fitted.

The likelihood fit is performed by the tool `gtlike`, which defines the log-likelihood using the observed and model counts and finds the maximum using minimisation algorithms, such as MINUIT [50]. The tool `gtlike` returns as output the best-fit values of the model parameters and their statistical uncertainties derived from the likelihood profile. Other methods are available through the python interface of `gtlike`, called `pyLikelihood`. These methods allow the computation of the source TS, asymmetric errors or upper limits, as described in section 3.2.1.

Finally, the results of the fit can be compared to the data by generating spectral or spatial residuals. A model map can be generated from the best-fit parameters, using the tool `gtmodel`, and then compared to the observed count map.

Another useful instrument to check the goodness of the fit is the TS map. This map is obtained by adding a point-like test source to the model and performing a likelihood fit. The fit is repeated moving the test source in all the pixels of the

map. The map is filled with the TS values of the test source in each position. A bright spot in the TS map suggests the presence of a significant excess in the data with respect to the model.

3.2.4 Summed likelihood

The `pyLikelihood` interface allows the possibility of performing a summed-likelihood analysis. This procedure is useful when different datasets are used or different cuts applied. A typical example is the usage of multiple event types in a combined analysis. Events from different event types are selected, as long as they belong to the same group (`FRONT/BACK`, `PSF` or `EDISP`), and the relative quantities for the likelihood definition are calculated separately, adopting IRFs specific for each type. The sky model adopted is usually the same for all the types. The total log-likelihood used for the model fitting is defined as the sum of the log-likelihoods of each type. Another example is the definition of different data cuts for different energy or time ranges. Also in this case, the log-likelihood is calculated separately for each data sample and then the values are summed together before the fitting.

The summed likelihood method is often useful to increase the significance of the results, since cuts and/or IRFs are optimized for each data sample. However, the computation time of the likelihood is usually increased and the fitting procedure becomes slower.

3.2.5 Source localization and extension

An important aspect of the study of a source is its spatial shape. The tool `gtlike` does not allow the fitting of spatial parameters of sources. In fact, an iterative procedure can be used to study the extension of a source, by performing independent fits with different fixed spatial models and comparing the results to extract the best model. In [51], it was shown that the maximum of the likelihood profile obtained varying the radius of an extended source correctly reproduces the extension of a simulated extended source, assuming that the true position is known. A similar approach can be also adopted to compare spatial models obtained from other wavelengths.

However, this procedure requires a high computing time and is quite limited, since it is difficult to apply when the true position of a source is not known. Furthermore, in order to maximise the statistical significance of the detection, the position, the extension and the spectrum of the source should be simultaneously fit.

For this reason, other tools have been developed inside the *Fermi*-LAT collaboration to perform spatial fits. The `pointlike` package provides methods to fit position and extension of sources, allowing different spatial shapes such as disk and 2D Gaussian shape. The main advantage in `pointlike` is that the spatial binning of data scales with the PSF, i.e. a coarse binning is adopted where the PSF is large. This technique allows better performances at low energy, where the PSF is large, keeping a good accuracy at high energy. The approximations are performed maintaining an accuracy level of 1% [52, 53]. *pointlike* has been extensively used within the *Fermi*-LAT collaboration, especially in the development of source catalogs [54–56].

The `fermipy` package is a python software toolkit that facilitates the data analysis using the *Fermi Science Tools*. It also provides methods for high level analysis, such as the localization and extension fitting, which are based on a sampling of the likelihood varying the spatial parameters of a specific source. It also provides simple ways of configuring a summed likelihood analysis, in which multiple data selections can be provided and fitted together [57].

Chapter 4

The interstellar emission model

4.1 The "standard" diffuse model

The source analysis of *Fermi*-LAT data is strongly based on the good description of the γ-ray background coming from the cosmic ray diffusion in the Galaxy, which is largely dominant at GeV energies. It is mainly due to the interaction of CR protons and electrons with the interstellar medium (ISM). The main γ-ray production processes are the π^0 decay originating from CR proton interaction with gas in the ISM, the bremsstrahlung radiation of CR electrons interacting with the gas and the Inverse Compton scattering of CR electron on the interstellar radiation field (mostly made of the cosmic microwave background, the infrared dust emission and the visible star light), which have been already described in chapter 1.

Since the first γ-ray observations of the Galaxy, a correlation between the large scale emission and the gas distribution was evident [58–60].

The *Fermi*-LAT collaboration has developed a model describing this diffuse emission, called Galactic Interstellar Emission Model (GIEM), which includes the γ-ray emissions coming from all the large scale structures in the Galaxy. It is then suitable to describe the background for point-like or small extended sources [61]. The model is obtained as linear combination of different maps describing the emissions coming from the different processes and the different structures in the Galaxy, which are directly fitted to the data in many energy bins, in order to recover the spectral shape of each component from the data.

This "data-driven" approach is preferred to a model based approach, which makes assumptions on the CR distribution in the Galaxy and calculates the γ-ray emissions. Simulation codes such as GALPROP [13] [1] and DRAGON [14] [2] calculate the CR distribution in the Galaxy assuming a certain CR source distribution and CR spectrum at the source and making prescriptions for the CR diffusion in the Galaxy. The γ-ray flux is then obtained using the γ-ray production cross sections of the different processes. This approach is affected by many uncertainties, since most of the parameters describing the CR production and diffusion are not known with good accuracy.

Nevertheless, simulation codes are essential to understand the mechanisms involving CR origin and propagation in the Galaxy. Many works have been developed adopting these codes. In [62, 63], the authors adopted the GALPROP code to perform simulations of the Galaxy with different input parameters, obtaining models which are broadly consistent with the *Fermi*-LAT data, with some under-prediction towards the inner Galaxy. In [64], the code DRAGON was used, adopting a non-isotropic diffusion of CR, obtaining also in this case a good modeling of the diffuse γ-ray emission of the Galaxy.

In the development of the GIEM, the code GALPROP was used to obtain a template for the Inverse Compton scattering, since no spatial template is available for this mechanism from other wavelength observations. This component is usually very smooth and it is sub-dominant with respect to the gas-related component for energies above $\sim$ 100 MeV in regions close to the Galactic plane.

4.1.1 Emission components

As already said, the main emission is correlated to the interstellar gas. A template for the gas distribution is obtained from observations in the radio band. The main assumption is that the CRs uniformly penetrate the Galaxy, so that the γ-ray intensity is proportional to the gas density. This assumption is not completely true, since CR density and spectrum change with the distance from the center of the Galaxy. For this reason, the gas templates is divided in galactocentric rings, each one fitted independently. Furthermore, the CR density may be modified in

[1] See `https://galprop.stanford.edu/publications.php?option=overview` for more details.

[2] See `https://github.com/cosmicrays` for more details.

magnetized molecular clouds due to small-scale diffusion effects, which may lead to an exclusion or a concentration of CRs in the cloud. These effects should change the γ-ray flux at energies relevant for gas ionization, i.e. below few GeV.

4.1.2 Gas column densities

Approximately the 99% of the ISM mass is gas and 70% of this mass is hydrogen. The hydrogen exists mostly in the form of neutral atoms (HI) and neutral molecules (H_2). Heavier elements are assumed to be uniformly mixed with the hydrogen and γ-ray production cross-sections are scaled accordingly.

Atomic Hydrogen

HI column density is traced by the 21 cm line radiation, due to the transition between the levels of the hyperfine structure of the Hydrogen [3]. Radio observations of the 21 cm provide the brightness temperature T_B, which is defined as the temperature that a black body would have to duplicate the observed intensity of a grey body object at a given wavelength. The quantity T_B is derived as a function of the velocity v of the gas relative to the Earth, which is measured thanks to the Doppler shift of the 21 cm line. This velocity can be converted into a Galactocentric distance as it will be explained below. The 21 cm all-sky Leiden-Argentine-Bonn (LAB) survey was used to derive the HI column density in this case [65].

The column density is obtained using the following equation:

$$N_{HI} = -1.82 \times 10^{18}\ T_S \int \ln\left[1 - \frac{T_B(v)}{T_S - T_0}\right] dv\ [cm^{-2}], \tag{4.1}$$

where $T_0 = 2.66K$ is the background brightness temperature in this frequency range and T_S is the excitation (spin) temperature of the gas. The integral is perfomed on the velocity range of interest to select a specific Galactocentric distance.

T_S is not uniform in the Galaxy, going from a value of around 100 K for the cold gas up to several tens of degrees for the warm gas. Its value can be derived from

[3] For the 1s ground state of the Hydrogen, the coupling of the electron and proton spin splits the energetic level in two hyperfine levels. The transition from the higher level (parallel spins) to the lower one (anti-parallel spins) corresponds to the emission of a photon with a wavelength of approximately 21.106 cm. The transition is called *spin-flip transition*.

the observation of HI absorption against background radio sources. However, this information is available in small regions of the sky only. For this reason, a uniform value for T_S was assumed and it was fixed to the one that best fits to the *Fermi*-LAT data. Changes in T_S indeed modify the spatial distribution of gas, which can be probed using the γ-rays produced by CRs. The fit was limited to the anticenter region ($90^\circ \leq l \leq 270^\circ$ and $-70^\circ \leq b \leq 70^\circ$), which is less affected by the unknown IC emission and is free from large extended structures unrelated to the gas, such as the Loop I and the *Fermi* Bubbles. The best-fit value obtained is $T_S = 140K$.

Molecular Hydrogen

Contrary to the atomic Hydrogen, the molecule H_2 cannot be observed through a direct emission. Its observation relies on other molecules, which are homogeneously mixed to the H_2. In particular, the carbon monoxide (CO), which is the second most abundant molecule in the ISM, can be observed through the 2.6 mm J=1→0 line, originating from the CO excitation due to the collisions with the H_2 molecule.

The velocity integrated brightness temperature W(CO) is proportional to the H_2 column density. This relation is observed experimentally comparing the virial masses of several molecular clouds to the CO luminosities. The H_2 to CO conversion factor is expressed as $X_{\rm CO} = N_{\rm H_2}/{\rm W(CO)}$.

The W(CO) values was obtained using the composite CO survey by [66].

Galactocentric rings

In order to allow a variation of the CR density with the distance from the center of the Galaxy, both the HI and H_2 column densities are divided in rings. This is perfomed calculating the integral column densities over specific velocity ranges, corresponding to particular distances. Nine rings have been defined with the following limits, expressed in kpc: 0.0, 1.5, 4.5, 5.5, 6.5, 7.0, 8.0, 10.0, 16.5, 50.0.

Dark Neutral Medium

The methods used to derive the gas column densities of HI and H_2 are affected by some approximations, which result in imperfections in the description of the gas-realted γ-ray emission. In the case of HI, the assumed constant spin temperature

T_S underestimates the gas density in some regions. Also the CO emission is not a perfect tracer of cold H_2. First, metallicity variations across the Galaxy may result in different $X_{\rm CO}$ values. Secondly, the CO molecule is strongly affected by UV photo-dissociation in the outer regions of molecular clouds where H_2 may exist without CO or where CO is only weakly excited. Finally, $X_{\rm CO}$ is also affected by the dynamical characteristics of the molecular cloud, resulting in variations by about a factor of 2 [67]. These limitations lead to large underestimates of the gas density in some regions, as well as some overpredictions in other regions. This missing gas is referred to Dark Neutral Medium (DNM).

This dark component can be obtained using dust column density. Dust grains are known to coexist with the gas. Observations have shown that the gas-to-dust ratio is approximately 100. Dust observation may directly trace the total gas column density.

Dust is observed thanks to its infrared emission. The dust map in [68] was used to correct the HI and H_2 column densities in the GIEM. More recently, high resolution dust maps have been provided by the Planck satellite [69]. This correction was based on the comparison of the dust column densities with the HI+H_2 ones derived before. Away from some regions were dust is strongly affected by star activity (star forming regions), most of the dust is well spatially correlated with the N_{HI} plus W(CO) distribution. Regions where this correlation is not present and dust is well correlated with γ-ray emission exceeding the one coming from HI plus W(CO) expectations are considered DNM-rich regions.

A template for dark gas was obtained by subtracting from the dust map the regions which spatially correlate with HI and W(CO). The resulting residual map reveals coherent structures in both positive and negative residuals.

The positive residuals suggest an under-estimate of the gas distribution and are used as template for the additional DNM. Since there is no velocity information associated with the IR dust emission, the map cannot be divided in rings. One single template is used for the entire sky, which corresponds to assuming a uniform CR flux across the sky for this template. It must be noted that the dust residual map also incorporates ionized hydrogen (H^+), which is not traceable with other direct observations. This component is anyway small compared to the DNM mass, which in some dense clouds is known to be comparable or exceed the CO-bright molecular component.

The negative residual map is also important to bring corrections to the gas distribution. Especially in the HI maps, the assumption of the uniform T_S value may lead to over-prediction of the gas column density (a too low TS corresponds to a too high gas density). The negative residual map is used to correct the N_{HI} map. It was found that these corrections do improve the goodness of the fit and were therefore included in the model.

4.1.3 Galactic Inverse Compton Radiation

Another important diffuse γ-ray component is due to the interaction of CR electrons with the interstellar radiation field, mainly made of the Cosmic Microwave Background (CMB), the infrared dust emission and the visible star light. The spatial distribution of this component is related to the radial distribution of CRs and to the intensity of the radiation field. It is generally peaked towards the Galactic center, where the CR density is higher and the stellar radiation is also stronger.

Since there is no direct observational template for this component, its spatial and spectral shape was predicted using the GALPROP code. Under the assumption of a certain CR source distribution and propagation parameters, GALPROP predicts the CR density in the Galaxy and calculates the γ-ray intensity.

4.1.4 Other templates

Other templates were added to the fit in order to model other point-like and extended structures in the γ-ray sky. First a template for the point-like and small-extended sources was derived from a preliminary version of the 3FGL [56]. The contribution of unresolved sources to the diffuse model was estimated to be between 2.5% and 8% above 10 GeV. These sources are likely absorbed by the IC or the inner HI templates.

Models for moving sources such as the Sun and the Moon were also added to the model. γ-rays are produced by the interaction of CRs with the Sun and Moon surfaces, which makes them appear as bright moving sources in the sky. The overall spectrum and the template describing their movement in the sky was derived in [70, 71].

An isotropic component was added, in order to take into account the possible extragalactic γ-ray emission and the residual CR background which contaminates the LAT data, in particular the irreducible background already discussed in chapter 3.

Finally, a template for the Earth's limb contribution was derived. This contribution comes from the interaction of CRs with the Earth's atmosphere. The *Fermi*-LAT observing strategy is such that the Earth is not directly in the field of view. Nevertheless, a large number of Earth's limb photons hit the LAT. They are usually cut selecting events with low zenith angle θ. Events with $\theta < 100°$ were selected in this case, cutting most of the Earth's limb. However, especially at low energy, there is still a residual contribution. A template for this contribution was derived by comparing count maps obtained with a more stringent zenith angle cut ($\theta < 80°$).

4.1.5 Residual extended excess emissions

After having included all previous components, large scales structures appear in the residual γ-ray data. Some of them are well known, such as the Loop I, one of the bright radio Galactic loops, and the *Fermi* bubbles, so called from the typical bubble shape above and below the Galactic plane. In other cases, extended residuals appear along the Galactic plane and their origin is not known. For these structures a template was derived from the residuals obtained from a first iteration of the diffuse model fitting. These templates were then included in the fit in order not to bias the normalization of the other components. Figure 4.1 shows the distribution of these residual extended excess emissions, taken from [61].

4.1.6 γ-ray model

Summing all components, the predicted counts of the γ-ray diffuse model are expressed as follows:

$$\begin{aligned} N_{\rm pred}(l,b,E) = & \sum_{i=annulus} q_{HI_i}(E)\widetilde{N}_{HI_i}(l,b) + \sum_{i=annulus} q_{CO_i}(E)\widetilde{W}_{CO_i}(l,b) + \\ & + q_{DNM}(E)\widetilde{N}_{DNM}(l,b) + C_{IC}(E)\widetilde{I}_{IC}(l,b,E) + C_{iso}(E)\widetilde{I}_{iso} + \\ & + C_{limb}(E)\widetilde{I}_{limb}(l,b) + \widetilde{I}_{sun+moon}(l,b,E) + \sum_{i=source} C_{src_i}(E)\widetilde{I}_{src_i}(l,b). \end{aligned} \tag{4.2}$$

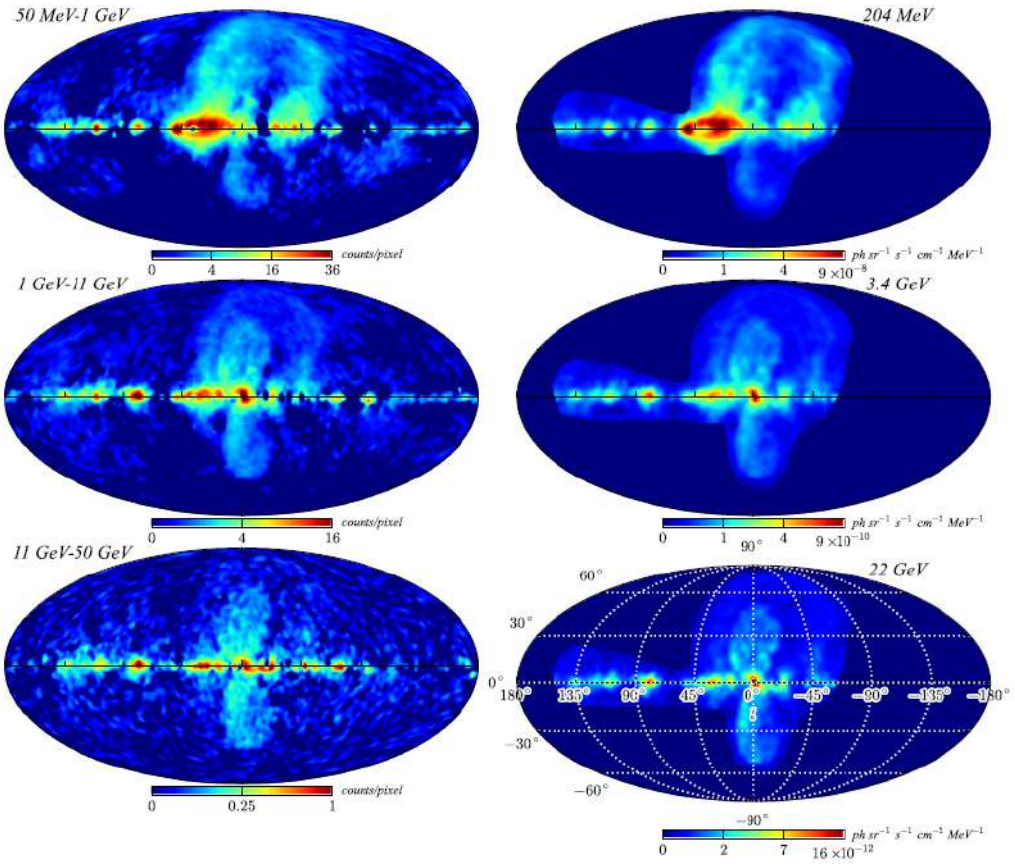

FIGURE 4.1: All-sky residuals from the Galactic diffuse model fitting. Left column: residual counts in three energy bands 50 MeV–1 GeV (top), 1–11 GeV (middle), and 11–50 GeV (bottom), smoothed with a two-dimensional symmetric Gaussian of 3° FWHM. Right column: photon specific intensity, at energies 204 MeV (top), 3.4 GeV (middle), and 22 GeV (bottom) of the residual emissions [61].

The q parameters represent the γ-ray emissivity of the gas-related components in the associated column density. The C parameters are the normalization factors of the other components. The Sun and Moon templates are not fitted to the data. The tilde notation denotes the maps after the convolution with the LAT PSF.

The residual excess emission described in the previous section was then added as a separate component, deriving the spatial template from the residual map. The residual map was filtered using a wavelet decomposition, in order to retain only structures larger than 2°. This aspect is crucial when studying large extended sources, since all sources with an angular scale comparable or larger than 2° might be absorbed partially or totally in the diffuse model.

The predicted counts derived with the previous equation are then fitted to the data using MINUIT. The fit is performed iteratively and separately in different regions

of the sky, in order to better constrain some of the parameters before performing an all-sky fit.

The best-fit parameters are used to derive the diffuse model expressed in flux units. The model was not corrected for the energy dispersion. This information is important to correctly calculate the predicted counts from this model during the source analysis, when this template is used to describe the background emission.

The GIEM is provided by the *Fermi*-LAT collaboration as a single model, meaning that the relative normalizations of all the components are kept fixed to their all-sky best-fit values. This aspect inevitably creates regions where the diffuse model under-predicts or over-predicts the data, which may affect the source spectra.

The latest version of the GIEM was derived using the `P7REP` data. In order to use the same model with `Pass 8` data, it has been scaled using an energy dependent factor, in order to match the different acceptances and energy dispersion of the data selections [4].

4.1.7 Cosmic ray distribution in the Galaxy

The best fit parameters of the different components were used to derive the diffuse model expressed in flux units. The flux corresponding to each template was studied in order to derive information on the CR protons and electrons. In particular, the gas templates in the different rings were interpreted with a model based on the hadronic interaction of CR protons with the gas and on the bremsstrahlung radiation from CR electrons. The proton-proton cross section was taken from [21], while the bremsstrahlung emission was based on [72]. In order to take into account the contribution of heavier nuclei in CRs and in the ISM, the proton-proton cross section was scaled to the nucleus-nucleus one, taking into account the abundance of heavier nuclei in the ISM and in the CRs.

The following spectra were assumed for the proton and electron populations:

$$\begin{aligned} N_p &= A_p \beta^{p_1} R^{p_2} \\ N_e &= A_e (E_k/E_0 + ((E_k - E_4)/E_0)^{-0.5})^{p_3}, \end{aligned} \tag{4.3}$$

[4] More details are available at `https://fermi.gsfc.nasa.gov/ssc/data/access/lat/Model_details/Pass8_rescaled_model.html`

where R is the proton rigidity, $\beta = v/c$ is proton velocity over the light velocity and E_k is the electron kinetic energy. A_p and A_e are the normalization parameters of the two spectra. p_2 represents the proton spectral index, while p_1 controls the low-energy spectral curvature [73]. The fit proved to be almost insensitive to p_1 variations. p_3 is the electron spectral index. E_0 is fixed to the value of 1 GeV, while E_4 is a free scaling energy.

The best-fit parameters in each galactocentric ring allow the reconstruction of the CR spectra as a function of the distance from the center of the Galaxy. Figure 4.2 shows different quantities as a fuction of the Galactocentric radius.

It was found that the CR proton density follows the radial distribution of the γ-ray emissivity (figure 4.2a). It increases rapidly from the Galactic center, it is maximum at a distance of approximately 3 kpc and then smoothly decreases for larger distances (figure 4.2b). This pattern is probably related to the CR source distribution in the Galaxy. Actually, it is well correlated with the star formation rate, which is traced by sources such as Supernova Remnants and pulsars (figure 4.2d).

Another interesting feature is the dependence of the spectral index with the Galactocentric distance (figure 4.2c). It ws found that the spectrum is harder towards the Galactic center with respect to larger distances. This is known as "CR gradient problem". This behaviour is not predicted by propagation codes like GALPROP, which assumes constant diffusion parameters across the Galaxy, derived from the local measurements. A solution was proposed by [64], in which a radial dependency of the diffusion coeffient was introduced, specifically by linearly decreasing the rigidity index of the diffusion coefficient. This was implemented in the DRAGON propagation code.

4.2 Systematic uncertainties from the diffuse model for source analysis

Due to the approximations made and to the uncertainties in the templates adopted, the GIEM is affected by some systematic uncertainties.

The main source of these errors is the model incompleteness for the inner annuli, which was corrected with the introduction of the patches derived from residuals.

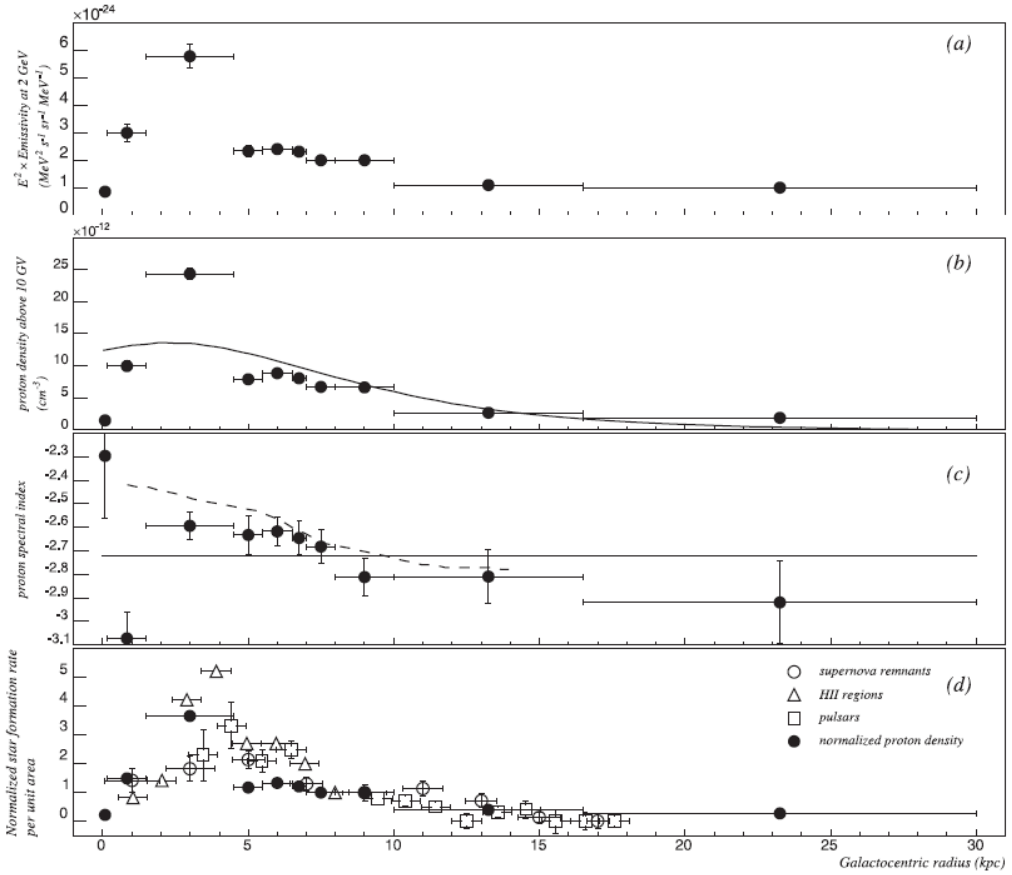

FIGURE 4.2: Radial distribution across the Galaxy of (a) the γ-ray emissivity per H atom measured at 2 GeV; (b) the proton flux integrated above 10 GV, with the prediction from the GALPROP model ${}^{S}Y^{Z}6^{R}30^{T}150^{C}2$ (solid curve); (c) the proton spectral index, p_2, with statistical error bars and the prediction for proton rigidities above 1 TV from the same GALPROP model (solid line) and from [64] (dashed line); (d) the proton flux integrated above 10 GV, normalized to its value at the Sun Galactocentric radius, with the star formation rate traced by supernova remnants, H II regions, and pulsar. Figure taken from [61].

In particular, for rings 2 and 4, the flux of the gas components increases approximately by the 40% if the patches are removed from the template. Another source of uncertainty is the amount of dense cold HI in the spiral arms, whose variations are estimated to be around 20%. Also, the variations of spin temperature T_S in the Galaxy affects the modeling. In fact, a change in T_S from the best-fit value of 140 K to a value of 400 K results in a 30% variation of the HI column density in the inner annuli. Finally, the poor angular resolution of the dust map adopted affects the DNM corrections especially along the Galactic plane.

For these reasons, systematic uncertainties from the diffuse model must be taken carefully into account when doing source analysis, since their flux and shape may be strongly affected by the model imperfections.

Since the standard GIEM is provided as a single model, the individual components cannot be adjusted separately. The overall normalization is usually fitted to the data, together with an energy dependent shape, which is usually a simple power-law.

A widespread method in the literature to estimate the systematics uncertainty consists in manually modify the diffuse normalization by a certain scaling factor (usually fixed to 6%) with respect to the best-fit value. This method gives the overall flux variations of the sources, since the diffuse model flux is rigidly scaled. So, it is not well suited to study possible variations in spatial or spectral shape of the source under investigation.

4.2.1 Alternative IEMs

An alternative way of estimating the systematic uncertainty from the diffuse model was developed in the first Supernova Remnant catalog (1SC) [38]. In this work, the source spatial shapes and spectra were tested adopting different diffuse models, based on a different approach with respect to the standard GIEM.

Eight different alternative Intersterllar Emission Models (aIEMs) were created using the GALPROP propagation code, by varying three important input parameters:

- the CR source distribution in the Galaxy, for which two models were adopted, respectively based on the spatial distribution of SNRs [74] and pulsars [75];
- the height of the CR halo, fixed to the values of 4 kpc and 10 kpc, which affects the CR propagation in the Galaxy;
- the uniform spin temperature used to derive the HI column density maps, fixed to the values of 150 K and 100000 K.

The values adopted for the three parameters were chosen to be reasonably extreme.

For each combination of the parameters, a model was obtained using GALPROP, divided in different components. The gas (HI and CO) components were divided in 4 Galactocentric rings (0-4 kpc, 4-8 kpc, 8-10 kpc, 10-30 kpc). Separate templates for the IC, the isotropic and Earth's limb emissions as well as for the large scales

structures of the Loop I and the *Fermi* bubbles were provided. Contrary to the standard GIEM, these components were not summed together, but were fitted separately, provided that their contribution was relevant to the region of the sky under investigation.

This approach allows more degrees of freedom in the fit, which may compensate for possible large scale residuals due to imperfection in the model. Furthermore, since the fit is performed in a specific region around the source of interest, the individual components are fitted much better to the emission of that region. On the other side, the aIEMs are based are much less refined compared to the stardard GIEM and may result in large over- or under-prediction in some regions.

Chapter 5

γ-ray emission from young Supernova Remnants Cassiopeia A and Tycho

5.1 Introduction

As already discussed in chapter 2, young SNRs are ideal candidates to search for CR sources and to test the acceleration theories. Cassiopeia A (Cas A) and Tycho represent two cases of young SNR. They have been widely studied at all wavelengths as it will be seen in chapter 6. The have already been studied with the *Fermi*-LAT data [76–78] and in both cases the observed spectral shapes seem to favor a hadronic scenario. For this reason a deep investigation of these source was performed in this work, with a particular focus on the energy range around and below 100 MeV, which is essential to disentangle between hadronic and leptonic models.

5.2 *Fermi*-LAT observations and data analysis

5.2.1 Data setup

The analysis procedure is based on the Poisson maximum likelihood method described in chapter 3 and it was performed using the *Fermi Science Tools*, also

described in chapter 3. The analysis was conducted separately for each of the two sources. However, since their angular separation is approximately 9°, the results found for one source do influence the analysis of the other, as it will be explained in next sections.

For each source, 106 months (nearly 9 years) of `Pass 8` data (`P302`) were selected in a 15° circular region of interest (ROI) centered on the nominal position of the source and in the energy range from 60 MeV to 300 GeV. The `SOURCE` photon class was used, which is the one recommended for source study.

Standard cuts were applied to the data with `gtselect` and `gtmktime`. A cut on the zenith angle was applied in order to reduce the contamination from the Earth's Limb. Following the cuts recommended by the *Fermi*-LAT collaboration, the cut was adapted to the energy range analyzed. At lower energies the Earth's Limb flux is higher and its contamination in the LAT field of view is larger due the larger PSF of the instrument. For this reason a tighter cut is necessary at low energy. In particular, three different zenith angle cuts $\theta < \theta_{max}$ were applied: $\theta < 100°$ for energies above 300 MeV, $\theta < 90°$ for energies between 100 MeV and 300 MeV and $\theta < 80°$ for energies below 100 MeV. For each θ-cut the livetime cube and the exposure were evaluated using the tools `gtltcube` and `gtexpcube2`.

Each ROI was described with a spatial-spectral model containing the diffuse emissions and the known point-like sources, as listed below:

- The standard Galactic diffuse model described in chapter 4. The spectrum was fitted with a power-law model, allowing for possible different scaling of the model between low and high energy.
- The isotropic model derived for the `SOURCE` photon class. The normalization of this model was fitted.
- Point-like sources in each ROI taken from the LAT catalog 3FGL [56]. Since sources outside the 15-degree ROI might still contribute especially at low energy, given the large PSF of the instrument, all sources within 20° from the ROI center were included. Normalizations of sources within 7° from the ROI center were fitted, while other parameters were kept fixed to the 3FGL values.

The sources under investigation, Cas A and Tycho, were centered at their nominal positions:

- Cas A: (RA, DEC) = (350.85°, 58.82°)
- Tycho: (RA, DEC) = (6.34°, 64.14°)

Even though they have been previously detected by the *Fermi*-LAT and they are both present in the 3FGL, no assumptions was made for their spectrum and a simple power-law was adopted at the beginning. The power-law model is defined as follows:

$$\frac{dN}{dE} = N_0 \left(\frac{E}{E_0} \right)^{-\alpha} . \tag{5.1}$$

Data were binned using `gtbin` in a squared region with a side of 21° and pixel size of 0.1°, so that the square is inscribed in the ROI selected. Data were binned in energy adopting 10 bins/decade. Figure 5.1 shows a count map of Cas A ROI in the energy range 60 MeV - 300 GeV.

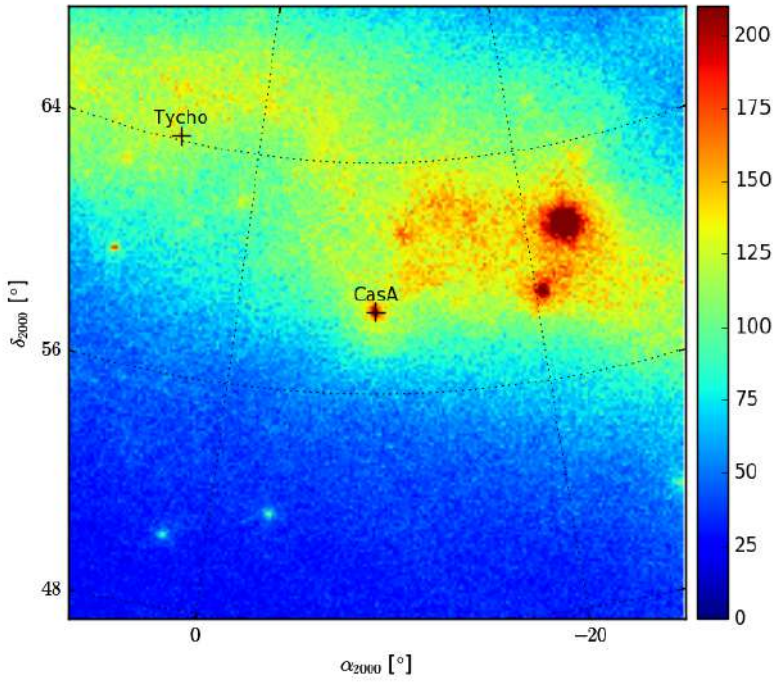

FIGURE 5.1: Count map of Cas A ROI in the energy range 60 MeV - 300 GeV.

The fit was performed using the `pyLikelihood` framework and energy dispersion was taken into account by enabling the corresponding `edisp` flag. As also pointed

out in chapter 4, the background diffuse models are not corrected for energy dispersion, so the flag was disabled for these models. A summed likelihood approach was adopted. Data were divided according to the four PSF event types defined within `Pass 8` data, as described in section 3.1.3. For each event type the data counts and the exposure were evaluated, so that the binned likelihood can be defined and evaluated. The sum of the log-likelihoods of the four event types is then used for fitting. The same binning was adopted for the four event types. The only exception is the pixel size of the `PSF0` type, which was 0.3° instead of 0.1°. This choice is driven by the fact that `PSF0` events have a larger PSF than other event types and the smaller number of total pixels speeds up the likelihood evaluation. The other difference among the four event types regards the choice of the isotropic model, since each event type has its own model describing the residual background in the data.

The summed likelihood approach is computationally more intensive than the classical binned likelihood, since the likelihood must be evaluated on four different data sets. However, this procedure allows a better usage of the instrument performances and mantains the full statistics. As a result, the significance of the results is increased if compared to the standard binned likelihood approach and to data selections in which worse event types are excluded.

5.2.2 Diffuse residuals in Cas A region

In the first step of the analysis, Cas A region was investigated. Previous studies [77] have pointed out that negative residuals were present close to Cas A. Authors in [77] concluded that, given the statistics available, the residuals did not affect the measured Cas A spectrum. However, in this work the enlarged dataset and the new `Pass 8` data release have increased the statistics and these residuals might influence the spectrum of the sources. For this reason their origin must be deeply investigated.

The ROI was fitted adopting the standard GIEM in four different energy ranges, in which the lower threshold of the energy range was progressively decreased: 1 GeV - 300 GeV, 300 MeV - 300 GeV, 100 MeV - 300 GeV, 60 MeV - 300 GeV.

Figures 5.2 represent the residual maps obtained from the best-fit model in each energy range. The residuals are defined in units of sigma:

$$R_i = \frac{C_i - M_i}{\sqrt{M_i}}, \tag{5.2}$$

where C_i and M_i represent the observed and the best-fit expected counts in the pixel i respectively. The theoretical distribution of these residuals in the hypotehsis of large statistics is a normal distribution. The maps were smoothed with a Gaussian 2D kernel with 0.2° radius. The convolution kernel was normalized such that the pixel distribution does not change, adopting the following definition:

$$\widetilde{w}_{ij} = w_{ij} \frac{1}{\sqrt{\sum_{ij} w_{ij}^2}}, \tag{5.3}$$

where w_{ij} are the weights of a kernel normalized to 1, i.e. such that $\sum_{ij} w_{ij} = 1$.

The maps present a significant negative excess (more than -5σ) close to the center of the ROI. The significance of the residuals increases when the energy range is enlarged, suggesting that the main contribution comes from the energies below 1 GeV. The extended negative excess is approximately few degrees large and it is located at $\sim 2°$ from Cas A. Since no point-like source is seen in this region, it is probably related to one of the components included in the galactic diffuse model, whose emission was over-predicted during the all-sky GIEM fitting procedure. Grey contours in the maps are taken from one of the CO maps from [66] (DHT14) and spatially overlap with the negative residuals, confirming that the excess might originate from this component.

It is not surprising that the GIEM contains regions with positive and negative residuals, since the fitting procedure was based on maps covering wide parts of the sky and the local emissions are not tuned directly to the data. Furthermore, the GIEM was derived with a much lower statistics, suggesting that possible negative residuals were not visible or not significant when the GIEM was derived.

It is particularly difficult to deal with negative residuals, since the *Fermi Science Tools* do not allow the fit of "negative" sources. For this reason a template for the γ-ray emission of the CO map was derived, it was then subtracted from the standard GIEM and added to the model as a separate source, so that it can be fitted independently from the overall model.

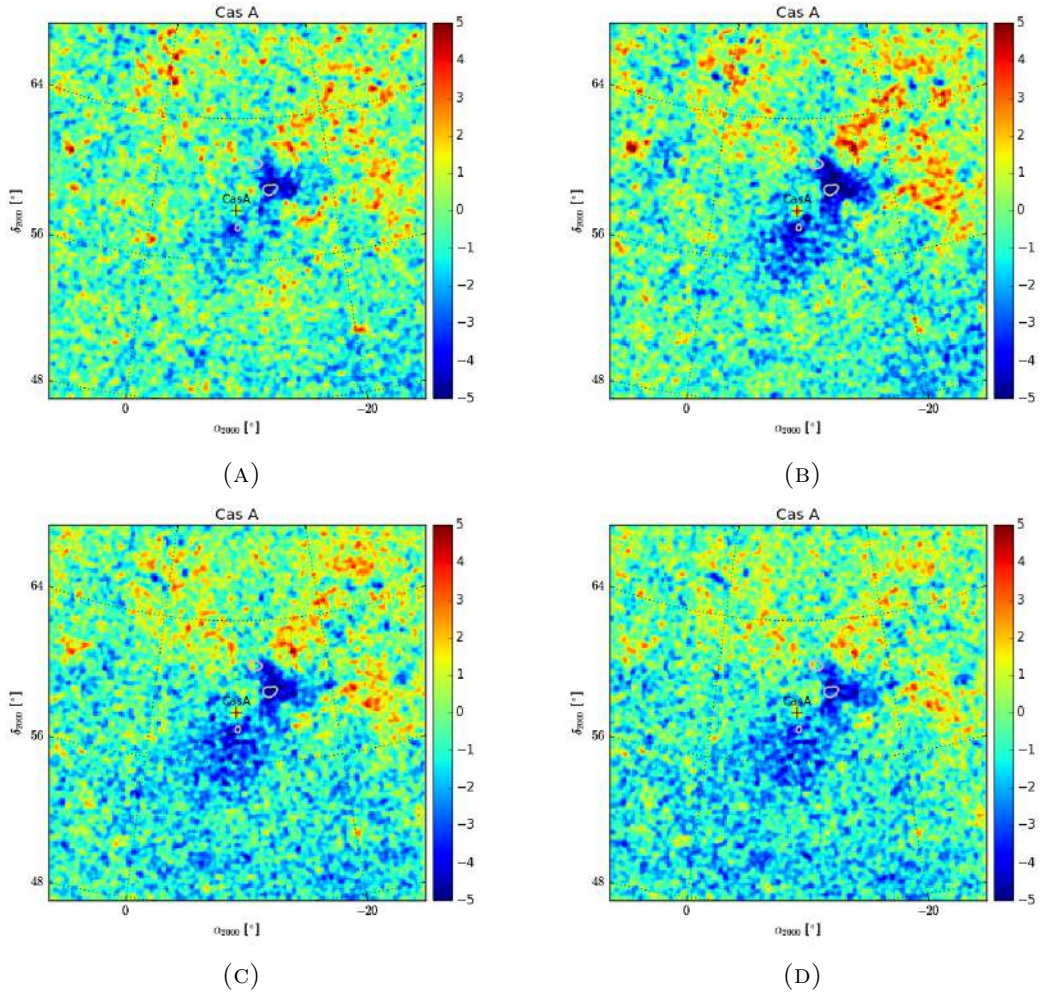

(A) (B)

(C) (D)

FIGURE 5.2: Residual maps of Cas A ROI obtained with the standard Galactic diffuse model. Grey contours represent the CO distribution taken from [66]. The four maps are obtained in four different energy ranges: (a): 1 GeV - 300 GeV; (b): 300 MeV - 300 GeV; (c): 100 MeV - 300 GeV; (d): 60 MeV - 300 GeV.

CO template

The CO template of the extended emission coincident with the negative residuals was derived adopting the first version of the standard GIEM. This version, labeled `rev0` hereafter, did not include the emission coming from the molecular gas in the outer Galaxy, which incorporates the CO template in the Cas A region, and was replaced by the complete version of the model, labelled `rev1` [1]. Figure 5.3 shows the ratio between `rev1` and `rev0` models in Cas A region.

[1]See `https://fermi.gsfc.nasa.gov/ssc/data/access/lat/BackgroundModels.html` for more details.

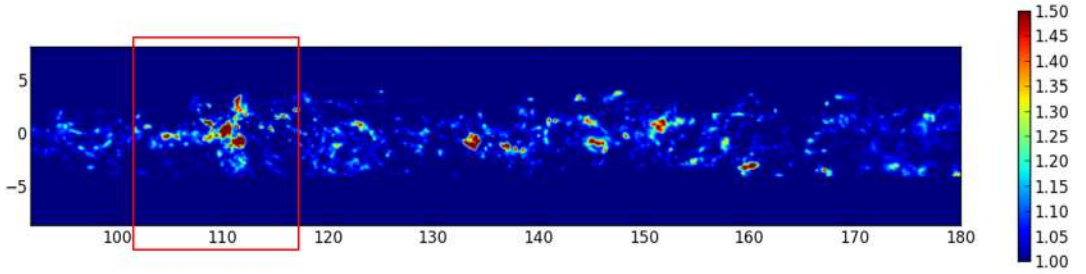

FIGURE 5.3: Ratio of `rev1` version of the GIEM over the `rev0` version. The red box highlights the region around Cas A.

As already pointed out in section 4.1.6, the GIEM was originally derived for `Pass 7` data and was then rescaled to `Pass 8` to match the different energy dispersion of the two data sets. The re-scaling procedure consists in defining an energy dependent scaling factor which takes into account the ratio of the energy resolutions of the two data processing. The procedure is described on the *Fermi*-LAT documentation on the FSSC [2]. The official `Pass 8` diffuse model (referred as "standard" hereafter) was derived re-scaling the `rev1 Pass 7` version of the GIEM.

In order to derive a template for the CO emission in Cas A region, the `rev0` diffuse model was first scaled to the `Pass 8` responses, following the same procedure used for the "standard" diffuse. Then, the scaled `rev0` model was subtracted from the "standard" one to obtain a template for the CO emission in flux units. All negative values in this template were manually forced to zero to avoid computational errors.

The diffuse Galactic γ-ray background was then described with an alternative model, which includes the `rev0` version of the GIEM scaled to the `Pass 8` data plus the template for the CO emission. This model will be referred as "*model 1*" hereafter. This model was intensively tested and compared to the "standard" model in terms of log-likelihood of the fit and of significance of the residuals.

As a further step, the CO template was splitted in two parts in order to allow for a better description of the region. The cut was applied at galactic latitude of $-1.5°$, dividing the template in a Northern and a Southern component. This model will be referred as "*model 2*" hereafter.

[2] `https://fermi.gsfc.nasa.gov/ssc/data/access/lat/Model_details/Pass8_rescaled_model.html`.

5.2.3 Cas A results

The "*model 1*" and "*model 2*" just defined were tested together with the "standard" model in the four energy ranges defined in section 5.2.2. The fitting procedure is described below and was repeated for each background model.

In order to better describe the ROI, a residual TS map (see sections 3.2.1 and 3.2.3) was generated in the energy range 1 GeV - 300 GeV. The residual emissions in this map were modelled out by adding additional point sources, whose position and spectrum were fitted using the package `fermipy`. In particular, the `find_source` method was used to add sources in the ROI with TS larger than 25, following the prescription in [56] [3]. The spectrum was described with a simple power-law for all the new sources and the flux and the spectral index were fitted to the data. The spectra of the point-like sources added to the model were fitted also in the other energy ranges analysed.

The position of Cas A SNR was fitted in the energy range 1 GeV - 300 GeV in order to take advantage of the better PSF of the instrument at high energy, using the package `fermipy`. The best-fit positions are reported in table 5.1 for the three background models. The best-fit position is separated from the starting position of less than 0.01° for all models. A test for the extension of the source was also performed, by fitting Cas A with an extended disk. The size of the disk was fitted to the data. The value of the TS_{ext} (see section 3.2.1) was very small for all the background diffuse models adopted, meaning that the extension was not significant and confirming that the point-like source hypothesis is preferred to describe Cas A. The 95% confidence level upper limit on the extension was also estimated. Results are reported in table 5.1.

Adopting the Cas A best-fit position and the additional point-like sources, the spectral fit was performed on the four energy ranges defined in section 5.2.2. Table 5.2 reports the $2\Delta \log \mathcal{L} = 2(\log \mathcal{L}_i - \log \mathcal{L}_0)$ values for "*model 1*" and "*model 2*" ($\mathcal{L}_i$) compared to the "standard" model ($\mathcal{L}_0$). The large values obtained suggest that the modified models are strongly favoured (with a significance larger than 5σ) with respect to the standard one, even though they have more degrees of freedom. Furthermore, the difference in log-likelihood between "*model 1*" and

[3] For each source 4 parameters are fitted (two coordinates for the position and two parameters for the spectrum), hence a TS value of 25 corresponds approximately to a significance of the source of 4σ.

TABLE 5.1: Results of localization and extension fit for Cas A SNR with three different background models.

Model	RA(°)	DEC(°)	Rad(°)	TS_{ext}	$\mathrm{UL}_{\mathrm{rad}}$(°)
"standard"	350.862 ±0.003	58.821 ± 0.003	0.003 ± 0.02	0.1	0.03
"model 1"	350.862 ±0.003	58.820 ± 0.003	0.004 ± 0.02	-0.1	0.04
"model 2"	350.862 ±0.003	58.819 ± 0.003	0.018 ± 0.02	-0.3	0.05

TABLE 5.2: Log-likelihood values of the fit of Cas A ROI over the four energy ranges 1 GeV - 300 GeV, 300 MeV - 300 GeV, 100 MeV - 300 GeV, 60 MeV - 300 GeV obtained with the "standard" diffuse model and the modified models. The values reported represent the $2\Delta \log \mathcal{L} = \log \mathcal{L}_i - \log \mathcal{L}_0$, where $\mathcal{L}_0$ refers to the "standard" diffuse model. The $\Delta\nu$ value represents the difference in degrees of freedom between the model i and the "standard" model.

Model ($\Delta\nu$)	1 GeV - 300 GeV	300 MeV - 300 GeV	100 MeV - 300 GeV	60 MeV - 300 GeV
"standard" (0)	-	-	-	-
"model 1" (2)	351.8	880.6	835.4	509.5
"model 2" (4)	445.2	1171.2	1214.6	758.5
"model 2" with BPL (6)	466.6	1350.83	2235.7	1563.7

"*model 2*" is larger than 90 in all energy ranges, suggesting that the second one provides a better description of the ROI, despite having two additional degrees of freedom. This result is indeed expected given the results in the previous section.

In order to allow for a better spectral description of the diffuse model, a broken power-law was used to describe the GIEM component in "*model 2*", defined as follows:

$$\frac{dN}{dE} = N_0 \begin{cases} \left(\frac{E}{E_{br}}\right)^{-\alpha_1} & \text{if } E < E_{br} \\ \left(\frac{E}{E_{br}}\right)^{-\alpha_2} & \text{if } E > E_{br}. \end{cases} \tag{5.4}$$

This test was driven by the fact that the spectral correction applied to the `rev0` version of the GIEM has not been tested on the overall all-sky model and might be affected by imperfections. In the last row of table 5.2 the log-likehood values of the broken power-law models are reported. The comparison with the results obtained with the power-law model (third row in table 5.2) shows that the broken power-law is preferred to describe the diffuse model. The difference in log-likelihood is small only when the analysis starts at 1 GeV. In fact, the best-fit value of the energy break in the broken power-law is smaller than 1 GeV when the fit is extended

at lower energies. So, the improvement in the fit at energies above 1 GeV is not so important. The best-fit parameters of the broken power-law obtained in the energy range 60 MeV - 300 GeV are:

- $N_0 = 0.9889 \pm 0.0003$
- $\alpha_1 = -0.156 \pm 0.001$
- $\alpha_2 = 0.0037 \pm 0.0003$
- $E_{br} = (185.7 \pm 0.8) MeV.$

In conclusion, the "*model 2*" together with a broken power-law to modulate the GIEM spectrum provides the best representation of the background of the ROI and will be adopted from now on to study the spectrum of Cas A and Tycho.

Up to now, Cas A spectrum was described by a simple power-law. In order to test the curvature of the spectrum at low energy, a broken power-law was adopted and the log-likelihood value was compared to the model in which a simple power-law was used. The curvature test was performed on the full energy range only (60 MeV - 300 GeV). Spectral results and the TS of the source obtained for the power-law and the broken power-law hypothesis are reported in table 5.3. The TS difference between the two models is $\Delta TS = TS_{BPL} - TS_{PL} = 2(\log \mathcal{L}_{BPL} - \log \mathcal{L}_{PL}) = 86$, with a difference of 2 degrees of freedom. This difference favours the broken power-law model with a significance larger than 5σ.

TABLE 5.3: Spectral results for Cas A SNR analyzed in the energy range 60 MeV - 300 GeV, adopting the best diffuse background model.

Model	Flux (ph./cm^2/s)	Index 1	Index 2	E_{break} (MeV)	TS
Power-law	$(9.2 \pm 0.1)10^{-8}$	-1.932±0.004	-	-	3299
Broken power-law	$(6.2 \pm 2.9)10^{-8}$	-1.64±0.06	-2.18±0.04	1844 ± 394	3385

Figures 5.4 reports the residual map obtained in the enegy range 60 MeV - 300 GeV using the best-fit model. It can be noticed that the region of the CO emission is now much better described. The negative residuals are not completely modelled out, suggesting that the model adopted to describe this emission might be improved. Ayway, their significance is strongly reduced. The independent fit of the

CO template has shown that its contribution is approximately equal to the 60% of what was introduced in the "standard" model.

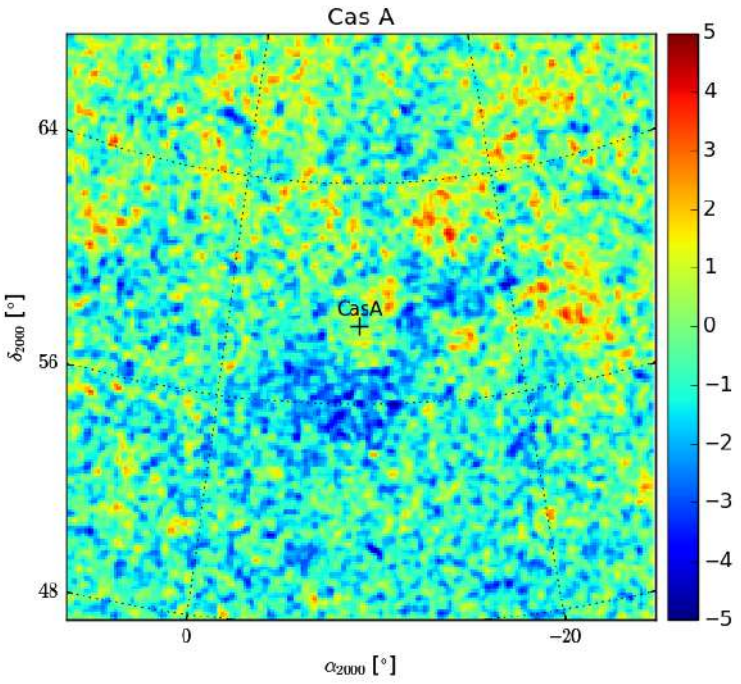

FIGURE 5.4: Residual map of Cas A ROI obtained with the modified Galactic diffuse model defined as "*model 2*" in the energy range 60 MeV - 300 GeV.

Spectral Energy Distribution (SED)

The spectral shape was studied in more detail fitting the spectrum independently in small energy bands, with equal width in logarithmic scale. The interval [300 MeV - 30 GeV] was divided in 16 bins (8 bins/decade), while for the intervals [60 MeV - 300 MeV] and [30 GeV - 300 GeV] a binning of 4 bins/decade was used. Larger bins proved to be necessary both at low and high energy due to the low significance of the source in these intervals.

In each energy band a summed binned likelihood analysis was performed, adopting the same pixelization as in the broad energy range analysis and a spectral binning of 3 bins in each energy band [4]. The source was fitted with a simple power-law spectral model, with spectral index fixed to the value of -2. The differential flux

[4]The choice of 3 bins in each energy bands assures that the width of each bin is still larger than the LAT energy dispersion at all energies, in order to avoid instrumental effects on the spectrum.

in the band is then obtained as the integral flux divided by the band width:

$$\frac{dN}{dE}(\bar{E}_i) = \frac{1}{E_{i+1} - E_i} \int_{E_i}^{E_{i+1}} F_i(E) dE, \tag{5.5}$$

where $F_i(E)$ is the best-fit power-law in band i and $\bar{E}_i$ is the mean energy in band i defined as:

$$\bar{E}_i = \frac{\int_{E_i}^{E_{i+1}} E F_i(E) dE}{\int_{E_i}^{E_{i+1}} F_i(E) dE}. \tag{5.6}$$

Figure 5.5 shows the results obtained both adopting the "standard" GIEM and the "*model 2*" defined above. The differential flux is multiplied by E^2 in order to better display spectral features. The best-fit broken power-law is also overlaid. Error bars and the shaded area represent the statistical uncertainty on the SED points and on the broadband fit. In each energy band the TS of the source was evaluated. Following the prescriptions in [56], in bands with $TS < 1$, a 95% confidence level upper limit was evaluated. The solid line and the shaded area represent the best-fit broken power-law model over the full energy range and its statistical uncertainty.

It can be noticed that the "standard" model (blue points) results in a very steep spectrum at low energy, in particular for $E < 500$ MeV. This cutoff has also been detected in past analysis [77] and it was attributed to the physical cutoff in the π^0-decay spectrum. However, the observed shape is steeper than the expected cutoff, suggesting that these data points are probably influenced by the negative residuals close to Cas A. On the other side, the SED obtained adopting the "*model 2*" is much smoother, still presenting a cutoff at low energy, which is probably related to the physical process of the pion decay, as it will be shown in chapter 6. It cannot be excluded that the close residuals are still affecting the spectral shape of Cas A, hence a careful estimate of the systematic uncertainty deriving from the diffuse model is necessary.

5.2.4 Tycho results

The analysis conducted on Cas A was repeated for Tycho SNR. Since the CO emission described in previous section is contained in Tycho's ROI, the results obtained before were used also for Tycho analysis. In particular, the fit was performed on the 60 MeV - 300 GeV energy range adopting the "standard" model

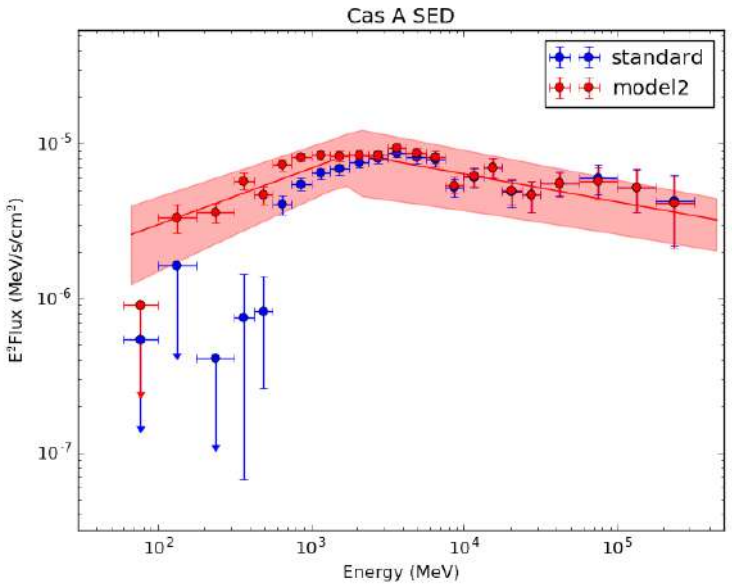

FIGURE 5.5: Spectral energy distribution of Cas A SNR obtained with the "standard" diffuse model (blue) and the diffuse "*model 2*" (red). Data points in the energy range [60 MeV - 100 MeV], [100 MeV - 300 MeV] and [300 MeV - 300 GeV] are obtained with a maximum zenith angle of 80°, 90° and 100° respectively. The red solid line and the shaded area represent the best-fit broken power-law model over the full energy range and its statistical uncertainty.

and the "*model 2*". The Galactic diffuse model was in both cases described with a broken power-law, according to the results found above.

Additional point-like sources were added to the model following the procedure described above in the energy range 1 GeV - 300 GeV. The position of Tycho SNR was fitted using `fermipy` and an extension test was performed also in this case. Results of the spatial fit are reported in table 5.4.

Tycho spectrum was described by a simple power-law. The curvature test was conducted on the broad energy range 60 MeV - 300 GeV, as described in previous section. No significant curvature was detected in this case ($TS_{ext} = 9$). Table 5.5 summarises Tycho spectral best-fit parameters, together with the TS value of the source.

Figure 5.6 shows the residual map obtained from the best-fit model. Also in this case the map does not show strong residuals. Blue spots in the bottom right part of the map correspond to the residuals described above for Cas A.

TABLE 5.4: Results of localization and extension fit for Tycho SNR with three different background models.

Model	RA(°)	DEC(°)	Rad(°)	TS_{ext}	UL_{rad}(°)
"model2"	6.3289 ±0.02	64.1627 ± 0.02	0.08 ± 0.03	3.1	0.12

TABLE 5.5: Spectral results for Tycho SNR analyzed in the energy range 60 MeV - 300 GeV, adopting the best diffuse background model.

Model	Flux (ph./cm^2/s)	Index	TS
Power-law	$(2.2 \pm 0.4)10^{-8}$	-2.10±0.06	160

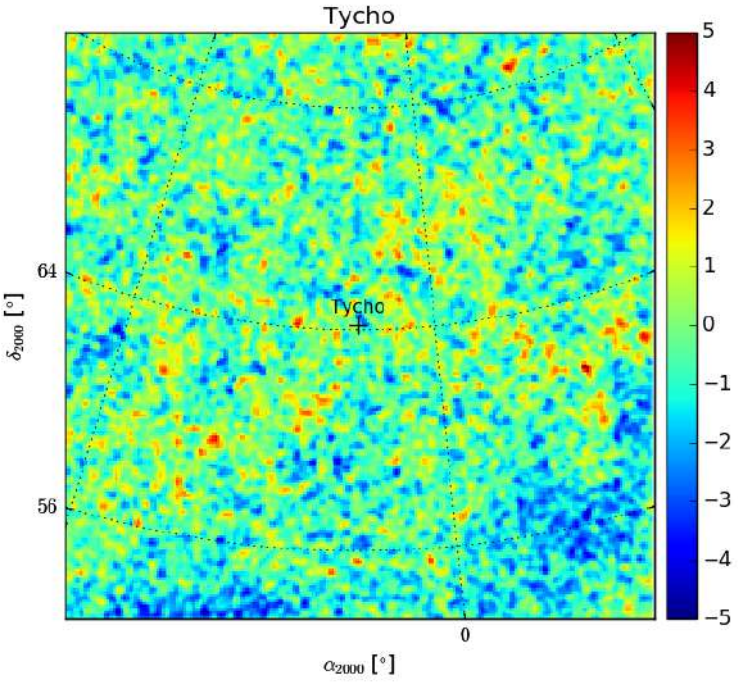

FIGURE 5.6: Residual map of Tycho ROI obtained with the modified Galactic diffuse model defined as "*model 2*" in the energy range 60 MeV - 300 GeV.

Spectral Energy Distribution (SED)

The spectral shape was studied following the same procedure adopted for Cas A. In this case, a logarithmic binning of 4 bins/decade was adopted in the energy range [300 MeV - 30 GeV], while 2 bins/decade were used at higher and lower energies. The TS of the source was evaluated in each band and 95% confidence level upper limits were evaluated in bands where TS was lower than 1. In figure 5.7, Tycho SED is shown, obtained adopting the background "*model 2*". Error bars represent the statistical uncertainty. The solid line and the shaded area represent the best-fit power-law model over the full energy range and its statistical uncertainty.

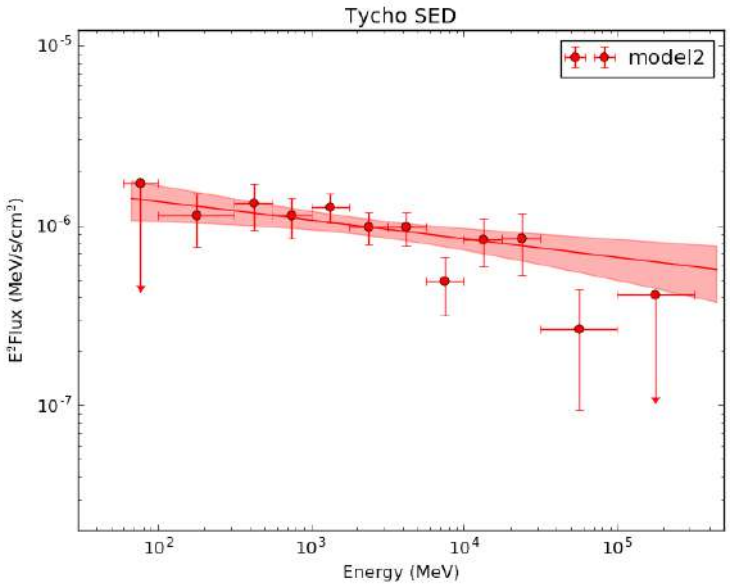

FIGURE 5.7: Spectral energy distribution of Tycho SNR obtained with the background diffuse "*model 2*". Data points in the energy range [60 MeV - 100 MeV], [100 MeV - 300 MeV] and [300 MeV - 300 GeV] are obtained with a maximum zenith angle of 80°, 90° and 100° respectively. The solid line and the shaded area represent the best-fit power-law model over the full energy range and its statistical uncertainty.

5.3 Systematic uncertainties

The study of systematic uncertainties is important to have an accurate measurement of the source spectra, especially at lower energies where the high number of photon counts reduces the statistical error. A wide discussion on possible sources of systematic error is available on the FSSC [5].

For the study of steady sources on long datasets, the main sources of systematics are related to the instrument response functions and to the background diffuse model. Other instrumental effects related for example to the orbit of the LAT or to the dependence of the IRFs on the azimuthal angle in the LAT instrument reference frame are weighted out when considering long exposures and must be taken into account only for the study of variable and transient sources.

The IRF systematic uncertainty arises from the differences in selection efficiencies between data and the IRFs predictions. The uncertainty band brackets the minimum and maximum deviation of the effective area from its nominal value in the IRFs. This uncertainty depends also on the data selection. No difference is

[5] see `https://fermi.gsfc.nasa.gov/ssc/data/analysis/LAT_caveats.html`

seen among photon classes, but the uncertainty increases when individual PSF or EDISP event types are used. Another important aspect is related to the energy dispersion. When energy dispersion is not enabled in the analysis, the agreement between data and IRF predictions worsens at all energies. The usage of energy dispersion is then necessary to reduce systematic uncertainties.

Figure 5.8a shows the energy dependent scaling functions that bracket the LAT effective area. Blue curves refer to individual PSF and EDISP event types, while the others refer to data selections including all events, `FRONT`-only or `BACK`-only events or joint analysis encompassing all events. Red and black curves are obtained with or without energy dispersion respectively. Figure 5.8b shows the energy dependent scaling functions for the PSF of the instrument.

In order to calculate the effect on the spectral parameters of the source under investigation, the analysis performed above with "*model 2*" was performed adding the energy dependent scaling functions (lower and upper bound) to the source model. The best-fit parameters obtained in these cases bracket the ones found without any scaling correction and provide an estimate of the systematic uncertainty from the IRFs.

The other source of systematic errors resides in the knowledge of the diffuse background model. In chapter 4 it was shown that the GIEM is derived taking into account multi-wavelength information and fitting the model to the data. However, several approximations were made in the template derivations and the presence of large diffuse residuals have already shown that the model is not perfect. In previous sections, it was also shown that the imperfections of the model might strongly influence the spectrum of a source, especially at low energy. For this reason a dedicated study of the systematic uncertainties from the diffuse model has been performed in this work and is described in next sections.

5.3.1 Systematics from the aIEMs

One way of estimating the uncertainty from the diffuse model consists in studying how the fitted parameters change when another diffuse model is adopted. This approach was derived and adopted in the first Supernova Remnant catalog developed by the *Fermi*-LAT collaboration [38], as already described in section 4.2.1.

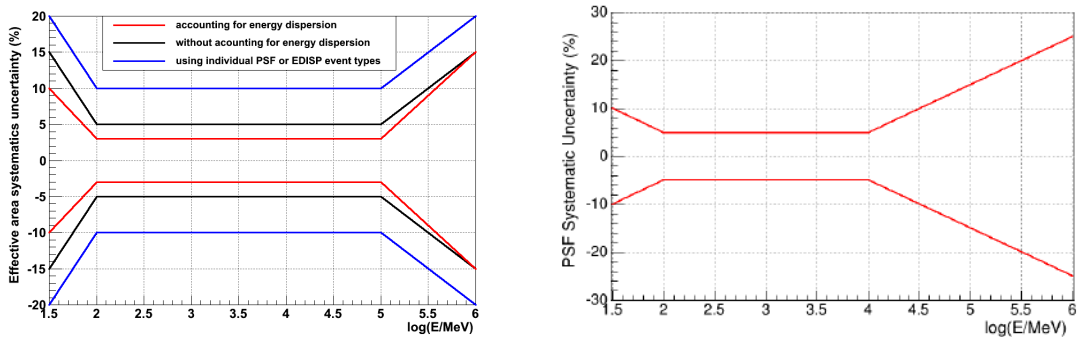

(A) (B)

FIGURE 5.8: Scaling functions to evaluate the systematic uncertainties from the IRFs. (a): energy dependent scaling functions that bracket the effective area. Blue: individual PSF and EDISP event types; black: all events, `FRONT`-only or `BACK`-only events or joint analysis encompassing all events without including energy dispersion; red:all events, `FRONT`-only or `BACK`-only events or joint analysis encompassing all events without including energy dispersion. (b): energy dependent scaling functions that bracket the PSF.

This method was applied to the two sources under investigation. The binned analysis was repeated adopting the eight aIEMs instead of the standard GIEM. Since these models were originally derived for `Pass 7` LAT data, they were rescaled to `Pass 8` data to correct for the different energy dispersion of the datasets, as described in section 5.2.2.

The eight models are provided as separate templates describing the HI and CO components in four Galactocentric rings plus templates for the IC emission and for the large scale structures (Loop I and Fermi Bubbles). Each component could be in principle fitted separately. However, in a particular ROI most of them will have a negligible contribution to the total emission and the good (and fast) convergence fit could be influenced by these components. For this reason, only components which contribute to at least the 3% of the total counts of the ROI are kept free in the model. The others are summed together and fixed to their original value. This procedure follows what authors did in [38]. One exception was made for the CO component in the outer Galaxy, which contains the CO template derived in section 5.2.2 and adopted in the "*model1*" and "*model2*". This component was kept free in the fit in spite of being below the 3% threshold.

The eight best fit values of a given parameter P were used to derive the systematic uncertainty, following [38]:

$$\sigma_{sys} = \sqrt{\frac{1}{\sum_i w_i} \sum_i w_i (P_i - P_{STD})^2}, \quad \text{with} \quad w_i = 1/\sigma_i^2, \tag{5.7}$$

where P_i and σ_i are the best-fit value and its statistical error obtained adopting the model i and P_{STD} is the value of the parameter obtained with the standard diffuse.

This equation defines conservatively a symmetric systematic error and may result in error bands on the flux which fall to negative values, even though the flux is naturally positive definite. In those cases, the error in logarithmic space was considered, adopting the following formula:

$$\Delta \log_{10} P = \left| \log_{10} \frac{P_{STD} + \sigma_{sign}\sigma_{sys}}{P_{STD}} \right|, \tag{5.8}$$

where

$$\sigma_{sign} = \text{sign} \left(\frac{\sum_i w_i P_i}{\sum_i w_i} - P_{STD} \right). \tag{5.9}$$

The extrema of the error bars are therefore defined by:

$$P_{\pm} = 10^{\log_{10} P_{STD} \pm \Delta \log_{10} P}. \tag{5.10}$$

5.3.2 Results

The two sources of systematic uncertainties (IRFs and background model) were studied following the methods described above to obtain the systematic errors on the spectral points.

The methods were applied separately in each energy band defined for the two sources in section 5.2 and then summed in quadrature:

$$\sigma_{syst,tot} = \sqrt{\sigma^2_{syst,IRFs} + \sigma^2_{syst,aIEMs}}. \tag{5.11}$$

The definition of $\sigma_{syst,aIEMs}$ given in previous section was applied adopting only the results of the aIEMs in which the source significance was above the TS threshold defined in section 5.2, in order to prevent possible bias due to parameters at their

lower limits. This was the cases of energy bands in which the significance of the source was close to threshold also for the standard diffuse model. As regards upper limits, the minimum and maximum upper limit values were used to define the systematic error band.

In figures 5.9 and 5.10 the SEDs of Cas A and Tycho obtained in section 5.2 are represented. Error bars represent the statistical uncertainty, while shaded boxes include the systematic errors summed in quadrature to the statistical errors. It can be noticed that the systematic bands are large for Cas A especially at low energy, in the energy range in which the negative residuals studied in previous sections were affecting the source flux, reducing the significance of the spectral features.

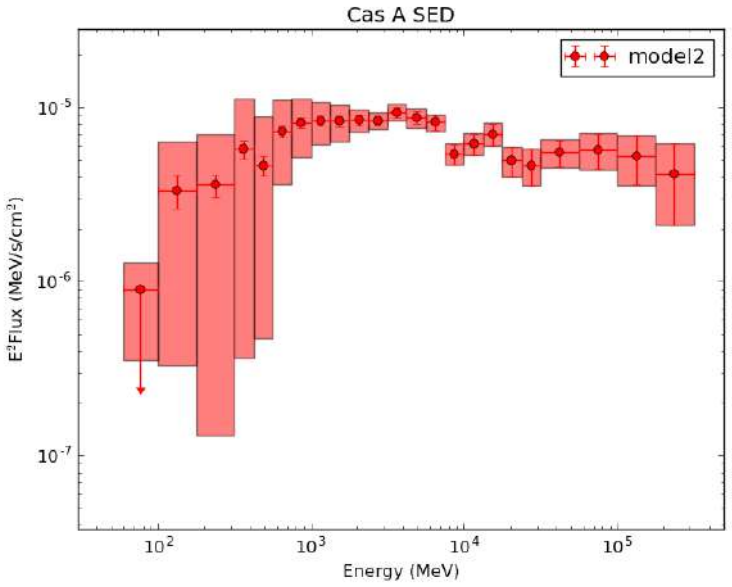

FIGURE 5.9: Spectral energy distribution of Cas A SNR with systematic errors. The error bars represent the statistical uncertainty only, while the shaded bands include the systematic uncertainties.

5.4 Systematics from the GIEM

In this work another approach was also developed and applied to the two sources under investigation. This method was developed under the supervision of Prof. Stefan Funk and Dr. Dmitry Malyshev at the Erlangen Centre for Astroparticle Physics, Erlangen, Germany.

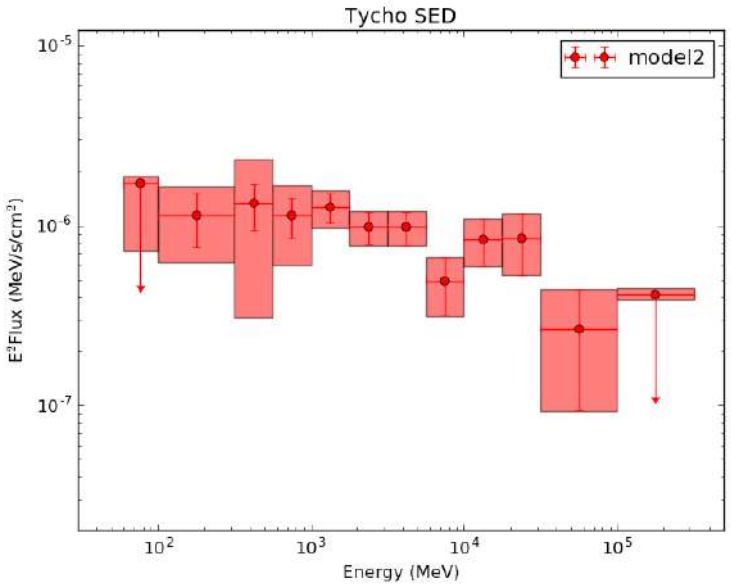

FIGURE 5.10: Spectral energy distribution of Tycho SNR with systematic errors. The error bars represent the statistical uncertainty only, while the shaded bands include the systematic uncertainties.

The method is based on the study of the fluctuations of the positive and negative residuals deriving from the standard GIEM in different positions of the sky. In this way an estimate of the systematic error is derived from the GIEM itself.

The procedure consists in the fitting of a test source placed at different positions along the Galactic plane, allowing both positive and negative values. The best-fit values obtained for the test source flux are then used to derive an average fluctuation and the estimate of the systematic error, as it will be described below.

The dataset adopted is based on 7.5 years of all-sky `SOURCE` class data in the energy range 50 MeV - 1 TeV divided in 31 bins equally spaced in logarithmic scale. A zenith angle cut of 90° was applied. The pixelization was based on the *HEALPix* (Hierarchical Equal Area isoLatitude Pixelation) scheme [6], with a $N_{side} = 256$, corresponding to a resolution of approximately 0.2°.

The test source was placed at the positions of a grid with a step of 1°, with the Galactic latitude varied between −2° and 2° and the Galactic longitude between 60° and 300°. The inner Galaxy was excluded from the analysis since fluctuations

[6]The HEALPix scheme produces a subdivision of a spherical surface in which each pixel covers the same surface area as every other pixel. The number of pixels is given by the relation $N_{pix} = 12N_{side}^2$, with $N_{side} = 2^k$ and k a positive integer. More information on HEALPix are available at `http://healpix.sourceforge.net/`.

are expected to be larger compared to the outer Galaxy and may over-estimate the systematic uncertainty for a source which is far from the Galactic center.

In each position, events from a 30°-radius circular ROI were selected. The fitting model included the standard GIEM, the isotropic emission, the known point-like and extended sources in the 3FGL and the test source placed at the ROI center. Sources from the 3FGL were described as a single template and its normalization was kept free in the fit. In this way the relative normalizations of sources is fixed and the degeneracy of the test source with the already known point sources is avoided. The flux value was fitted independently in each energy bin adopting the same fitting procedure adopted in [79] based on a χ^2 fit. The likelihood fit could not be used in this case since negative fluctuations are not allowed in *Fermi Science Tools*. Furthermore, the χ^2 fit allows a faster convergence and does provide a good approximation of the likelihood for a sufficiently large statistics, a condition which is satisfied at low energies where the systematic uncertainty usually dominates over the statistical error.

In figure 5.11 the best-fit value of the test source flux is shown as a function of the Galactic longitude for a fixed value of Galactic latitude $B = -2°$ (which is approximately the Galactic latitude of Cas A), for three different energy bins. It can be noticed that large fluctuations are visible in some regions of the sky and that they are much larger at lower energies, suggesting that residuals are mostly significant at low energies.

The best-fit flux values were used to estimate the average fluctuation along the Galactic plane, by calculating the standard deviation of the flux values f_i of the test source at the i-th position:

$$\sigma^2_{TOT} = \frac{1}{N_{ROI} - 1} \sum_{ROI(i)} (f_i - \bar{f})^2, \tag{5.12}$$

where $\bar{f}$ is the mean value of f_i. The quantity in equation (5.12) provides an estimate of the total uncertainty, since it includes both the statistical and the systematic uncertainties.

In order to estimate the statistical uncertainty, a Monte Carlo simulation was performed. For each ROI, the best-fit model was used to create 10 Poisson realizations of simulated data. The test source was not included in the simulated data. The 10 realizations were then analyzed with the model itself plus the test source. The

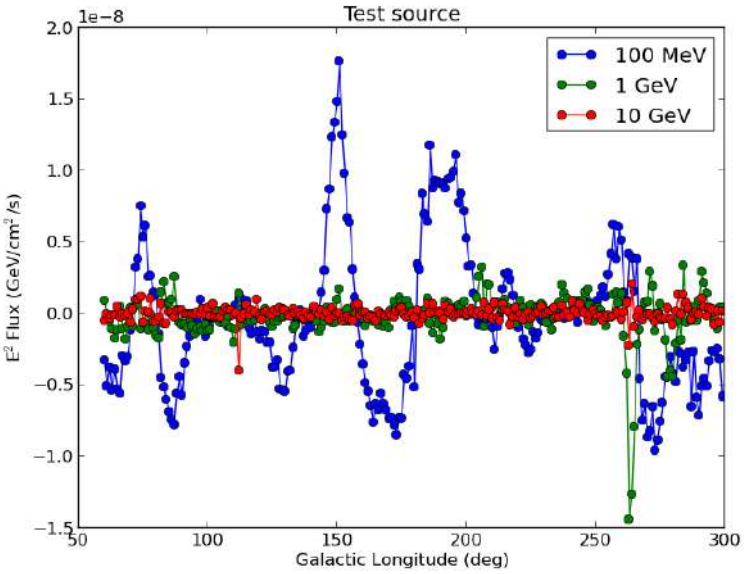

FIGURE 5.11: Differential E^2 flux of the test source along the Galactic plane as a function of the Galactic longitude for a fixed value of Galactic latitude $B = -2°$. The three lines correspond to three different energy bins: 100 MeV (blue), 1 GeV (green), 10 GeV (red).

fitted flux values of the test source provide an estimate of the statistical uncertainty:

$$\sigma^2_{stat} = \frac{1}{N_{ROI}} \sum_{ROI(i)} \sigma^2_{i,MC}, \tag{5.13}$$

with

$$\sigma^2_{i,MC} = \frac{1}{N_{MC} - 1} \sum_{MC(j)} (f_{i,j;MC} - \bar{f}_{i;MC})^2, \tag{5.14}$$

where $f_{i,j;MC}$ is the flux value of the test source in the i-th ROI and for the j-th Monte Carlo realization and $\bar{f}_{i,MC}$ is the mean value of $f_{i,j;MC}$ over index j. The average performed over the positions in the Galaxy in the estimate of the statistical uncertainty implicitly assumes that the flux along the Galactic plane is approximately the same. This approximation is not valid for the entire Galactic plane, hence regions with similar γ-ray fluxes should be selected. For this reason the Galactic center has been excluded from this analysis.

Finally, combining equations (5.12) and (5.13):

$$\sigma^2_{syst} = \sigma^2_{TOT} - \sigma^2_{stat}. \tag{5.15}$$

Equation (5.15) was applied independently to each energy bin, obtaining the estimate of the systematic uncertainty as a function of energy.

5.4.1 Results

The method was first applied to the Monte Carlo simulation. In this case σ_{stat} is obtained from equation (5.13), while σ_{TOT} was derived using one of the Monte Carlo simulation as data, i.e. setting $f_i = f_{i,0;MC}$ in equation (5.12). The results are plotted in figure 5.12. Blue, red and green points represent the total, statistical and systematic uncertainties from equations (5.12), (5.13) and (5.15) respectively. It can be noticed that in this case no systematic uncertainty is found, since the simulated data do not contain residuals beyond the statistical fluctuations.

The method was then applied to the real data. Results are presented in figure 5.13 with the same color code of figure 5.12. In this case, the statistical uncertainty is the same as in figure 5.13. It is evident that the total uncertainty is significantly different from the statistical error, especially at energies below 10 GeV. Systematics dominate for energies below 1 GeV, hence limiting the precision of measurements of source fluxes at lower energies, while for energies above 10 GeV the statistical errors are the main source of uncertainty due to the reduced statistics.

5.4.2 Remarks and future developments

The method derived in this work provides an alternative way of estimating the systematic uncertainty from the background diffuse model.

The results presented are still preliminary and might be improved in order to obtain more reliable systematic errors. For example, many point-like sources which were not resolved in the 3FGL are now detectable thanks to the larger statistics. These sources are not included in the model and might contribute to the (positive) residual emission assigned to the test sources. A similar argument is valid for other large scale emissions, such as the Earth's limb, which should be cutted out thanks to the zenith angle cut of 90°, but might still contribute especially at energies below 100 MeV.

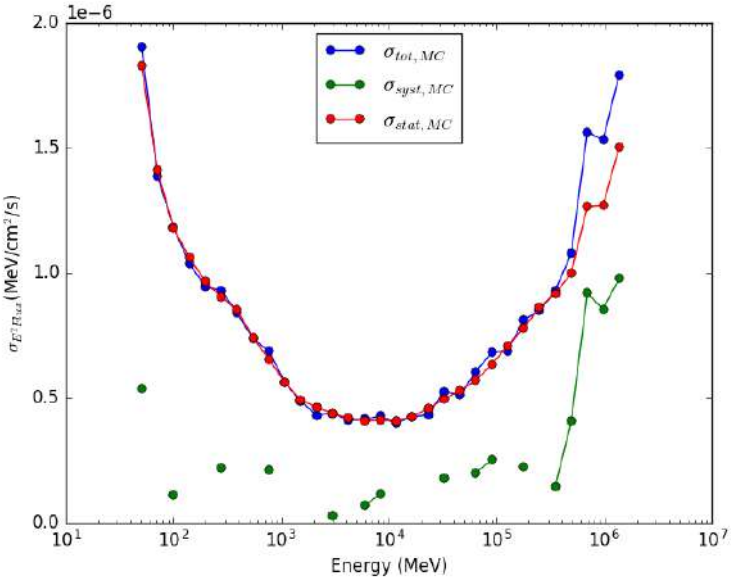

FIGURE 5.12: Systematic uncertainty (green) on the differential E^2 flux as a function of energy based on Monte Carlo simulation. The total (blue) and the statistical (red) uncertainty are also plotted as a function of energy.

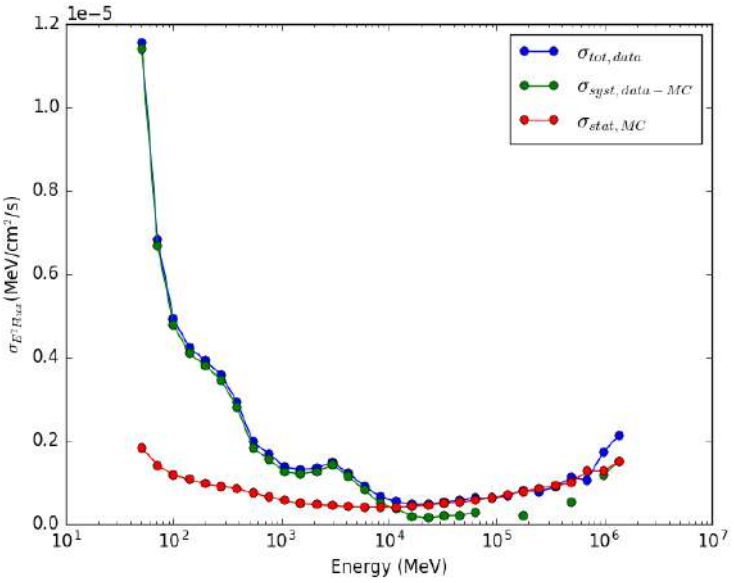

FIGURE 5.13: Systematic uncertainty (green) on the differential E^2 flux as a function of energy derived from the data. The total (blue) and the statistical (red) uncertainty are also plotted as a function of energy.

The method can be also easily generalized to study the systematics on extended sources. If the angular size of the test source is increased, fluctuations on a given angular scale can be studied.

A possible alternative to the procedure proposed in equations (5.12)- (5.13) would be the study of the fractional systematic errors, obtained comparing the test source flux to the total flux in each position. Possible differences between the two procedures should be investigated.

As a comparison, figure 5.14 shows the systematic errors derived with this method and those obtained adopting the aIEMs for Cas A SNR, as described in section 5.3.1. The results show similar behaviour for energies above few hundreds MeV, even though the systematics obtained from the aIEMs are larger. At lower energies the results obtained with the aIEMs do not raise smoothly, probably influenced by the low TS of the source in those energy bins.

The method developed in this work is different from the standard methods of estimating the systematic errors. Standard methods aim to study the systematics on a specific source, focusing on the specific ROI. From one side, this approach gives a more reliable estimate of the systematics of the source under investigation, but from the other it strongly depends on how well the background diffuse model is accurate in that specific region.

The new method developed gives a more general view on how accurate the background diffuse model is in the entire region analysed (the Galactic plane in this case) and gives an estimate of the systematic error for a putative source placed at any point in this region. As shown in figure 5.14, the results are comparable to those obtained with the standard approach on a bright source such as Cas A, but might over-estimate the systematic error for fainter sources and should be deeply investigated.

In conclusion, future developments of this method can provide a useful way of estimating the systematics from a given diffuse model and might result also useful for catalog analysis.

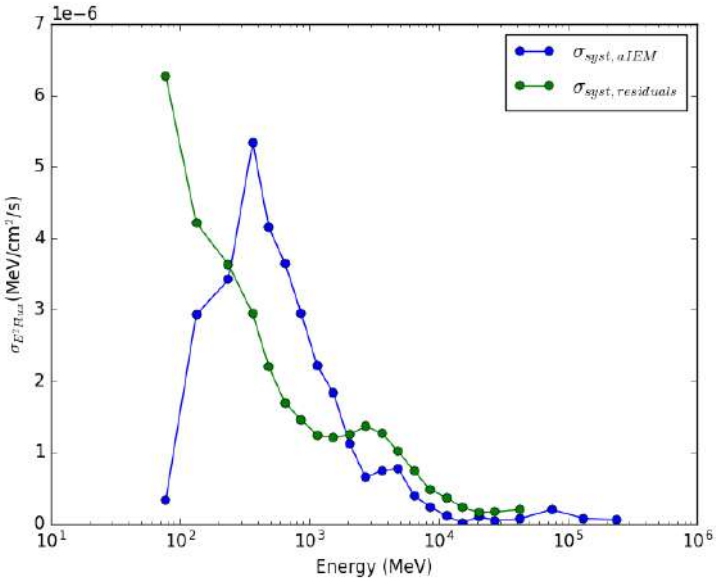

FIGURE 5.14: Comparison of the systematic errors on the differential E^2 flux as a function of energy derived from the GIEM residuals (blue) and from the aIEMs for Cas A SNR (green).

Chapter 6

The origin of the Supernova Remnant spectra

6.1 Introduction

The interpretation of the SED of the two SNRs can be provided through a model for the photon spectrum which is given by the convolution of the cross sections of the γ-ray production mechanisms (see section 1.5) with the injection spectra of accelerated particles. As already pointed out in chapter 2, the energy range around 100 MeV is crucial to disentangle between leptonic and hadronic origin of the γ-ray spectrum and therefore to obtain a direct evidence of CR acceleration in SNRs.

In this work, a model was developed to explain the multi-wavelength SED of Cas A and Tycho SNRs, from radio to TeV energy band, including the *Fermi*-LAT measurements derived in chapter 5. The model is based on the hadronic interpretation of the γ-ray spectrum, but leptonic contribution is also taken into account.

6.2 Model definition

In order to predict the photon flux, the cross sections of the non-thermal emission mechanisms described in section 1.5 were convolved with the spectra of accelerated particles.

No detailed calculation of the SNR evolution was performed, but a simple power-law in momentum was assumed for the accelerated proton and electron populations, following equations (2.22) and (2.23). As regards the electron population, a super-exponential cutoff was introduced in the particle spectrum to take into account energy losses which affect electrons radiating in strong magnetic fields, following [80]. The particle densities (number of particles per unit volume and unit momentum) are therefore described as follows:

$$\begin{aligned} \frac{dn_p}{dp} &= A_p \left(\frac{p}{p_0}\right)^{-s_p}, \\ \frac{dn_e}{dp} &= A_e \left(\frac{p}{p_0}\right)^{-s_e} \exp\left(-\frac{p}{p_{cut,e}}\right)^b, \end{aligned} \tag{6.1}$$

with $b = 2$ for the electron energy losses. The particle intensity (number of particles per unit area, unit time, unit solid angle and unit momentum) is then obtained by multiplying the particle density by the factor $\beta c/4\pi$:

$$J(p) = \frac{\beta c}{4\pi} \frac{dn_{p/e}}{dp}. \tag{6.2}$$

Since cross-sections are usually expressed as a function of kinetic energy, the particle intensity as a function of the kinetic energy E_k is:

$$J(E_k) = \frac{dp}{dE_k} J(p(E_k)) = \frac{1}{\beta} J(p(E_k)), \tag{6.3}$$

with $p(E_k) = (E_k(E_k + 2m))^{1/2}$.

The normalizations, the spectral indices and the electron cutoff energy were fitted to the data. Accelerated electrons are responsible of the radio to X-ray non-thermal emission via synchrotron radiation and contribute to the γ-ray spectrum via bremsstrahlung and inverse Compton emissions. Accelerated protons produce γ-rays via π^0 decay. The interaction cross-section was derived using FLUKA code [22]. The four processes involving the interaction of accelerated protons and helium nuclei on target protons and helium nuclei were taken into account, as described in section 1.5.5. For both the accelerated and the target helium, it was assumed that the densities are equal to the 10% of the accelerated and target proton densities respectively.

6.3 Cassiopeia A

Cas A, also known as SNR G111.72.1, is the remnant of the historical core-collapse Supernova exploded in 1680 ($\sim$ 340 years ago). It is one of the brightest young SNRs in the Galaxy and is very well studied and observed at all wavelengths. It is located at a distance of $3.4^{+0.3}_{-0.1}$kpc and has an angular size of $5'$ in radius corresponding to a physical size of $2.47pc$ [81].

It is the brightest radio source in our Galaxy and its overall brightness across the electromagnetic spectrum makes it a very good source to study particle acceleration in SNRs.

Cas A has been extensively studied in radio wavelengths [82–92]. The radio spectrum is close to a power-law with spectral index equal to 0.77 [88]. Most of the emission comes from a bright radio ring, which is believed to be related to the reverse shock propagating into the supernova ejecta. Several bright knots are also observed [91], which are attributed to dense clumps of ejecta that are not strongly decelerated after the Supernova explosion.

Several emission regions were also identified in the X-ray band (Chandra [93, 94], Suzaku [95], NuSTAR [96], INTEGRAL [97]). Chandra X-ray images [93] and high-resolution VLA radio synchrotron maps [98] show a thin outer edge to the SNR that has been interpreted to represent the forward shock, where the shock wave encounters the circumstellar medium [99]. The shock velocity has been measured by observing the proper motion of these filaments thanks to the Chandra observations, resulting in an estimate of 4900 km s^{-1} [100]. High-resolution observations [93, 101–103] also confirm the existence of the reverse shock that decelerates the impinging ejecta. In [104], the authors have observed an year-scale variability in the synchrotron X-ray filaments at the reverse shock, which would require a magnetic field amplification at the shock of the order of mG. Hard X-ray observations [96, 105], have also confirmed the presence of dense knots, proving the presence of relativistic electrons, which can also produce γ-rays through relativistic bremsstrahlung.

In the γ-ray domain, *Fermi*-LAT detected the source at GeV energies [76] and later derived a spectrum that shows a low energy spectral break at 1.72 ± 1.35 GeV [77]. In the TeV energy range, Cas A was first detected by HEGRA [106] and later confirmed by MAGIC [107] and VERITAS [108]. Updated measurements

have been recently reported by MAGIC [109] and VERITAS [110] extending the spectrum up to 10 TeV and suggesting that the spectral index in the TeV band is steeper with respect to the *Fermi*-LAT band.

Multi-wavelength modelling of Cas A observations has not yet resulted in a clear discrimination between hadronic and leptonic origin of the observed radiation in the GeV to TeV energy range [77, 111–114]. However, the break in the *Fermi*-LAT spectrum at 1 GeV suggested that the observed γ-ray flux has either a pure hadronic origin or that several mechanisms (hadronic and leptonic) are involved. For this reason, the detailed study of systematic uncertainties in the previous section is crucial to possibly detect the low-energy spectral break.

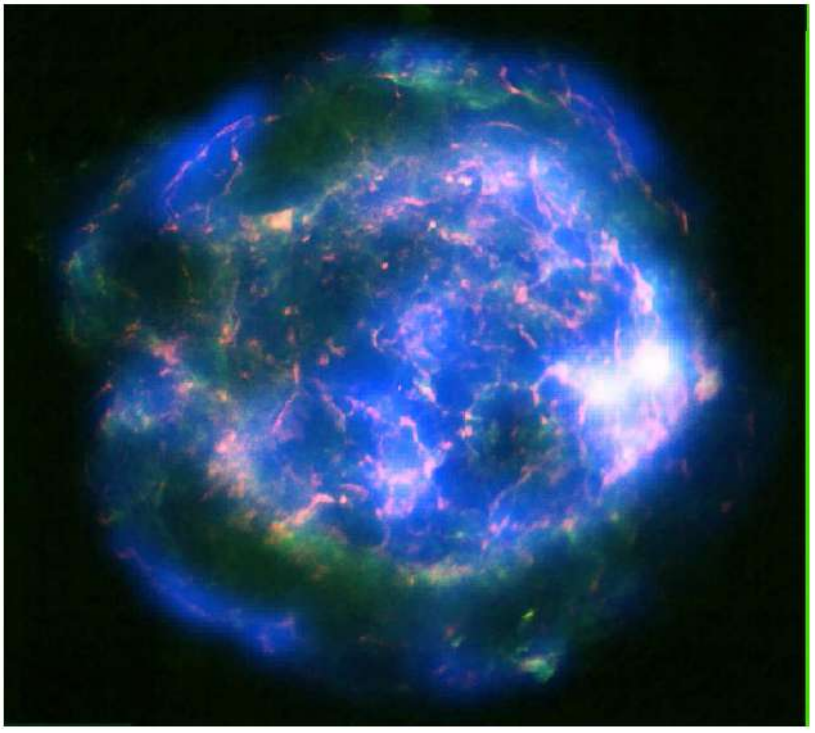

FIGURE 6.1: Comparison of the Chandra, VLA, and NuSTAR continuum images of Cas A. Red: Chandra 4–6 keV data [94]; Green: VLA 6 cm data; Blue: NuSTAR 10–15 keV data [96]. Figure taken from [96].

6.3.1 Modeling results

In order to study the multi-wavelength SED, data from different energy bands were selected (radio [88], X-ray [95, 97], TeV [109] and combined to the *Fermi*-LAT data derived in this work.

In order to predict the synchrotron emission, the value of the amplified magnetic field was fixed to 1 mG, following the results based on X-ray observations. The inverse Compton scattering was calculated on the CMB photon field, characterized by a temperature of 2.73 K and an energy density of 0.25 eV/cm^3, and on the infrared (IR) dust emission, with a temperature of 100 K and an energy density of 2 eV/cm^3 [115]. The target (or ambient) density necessary for the bremsstrahlung emission and the hadronic interaction was fixed to 2 cm^{-3} [116]. A distance of 3.4 kpc [81] was assumed in order to obtain an estimate of the CR energy content in the SNR.

Figure 6.2 shows the multi-wavelength spectral points with the best-fit model (black thick line). The colored thin lines represent the individual components.

The electron spectral index well reproduces the radio index and is compatible from the expectations from equation 1.41, given the measured radio index of 0.77. However, it was found that the cutoff in the synchrotron spectrum is not as sharp as expected from equation (6.1). An exponential cutoff with $b = 1$ was tested and results in a better fit.

The γ-ray spectrum is dominated by the hadronic interaction at energies below few hundreds GeV. However, as also found in previous works [77, 109], the different shapes of the GeV and TeV emissions require a cutoff in the proton spectrum, which is modelled as in the electron spectrum in equation (6.1) with $b = 1$. This cutoff is fitted to the data resulting in a value of approximately 15 TeV. This suggests that Cas A is not an efficient accelerator at high energies.

The estimated value of the proton energy content W_p, i.e. the total energy transferred to accelerated protons, results in an acceleration efficiency of 2%, if the an explosion energy value of $2 \cdot 10^{51}$ erg is assumed. Finally, the K_{ep} value is quoted, i.e. the ratio between the electron and proton energy content W_e/W_p, which is found to be approximately equal to 15%.

The best-fit parameters are reported in table 6.1.

TABLE 6.1: Best fit parameters of the interpretation model for Cas A SNR.

s_p	$p_{cut,p}$ (TeV/c)	s_e	$p_{cut,e}$ (TeV/c)	W_p (erg)	K_{ep}	χ^2/dof
2.23 ± 0.02	14.8 ± 2.7	2.535 ± 0.007	4.2 ± 0.1	$4.3 \cdot 10^{49}$	15%	183/91

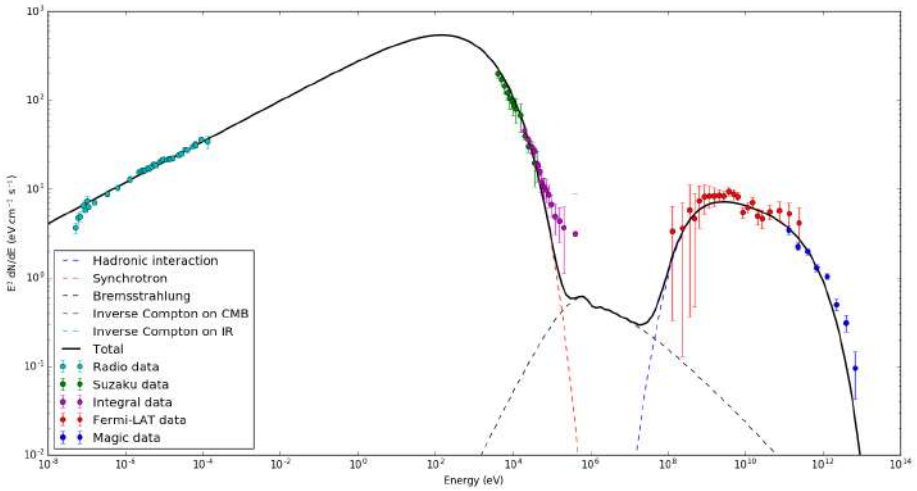

FIGURE 6.2: Multi-wavelength SED of Cas A SNR with the best-fit interpretation model. The thick black line represents the total model, while colored lines the individual components. Data points are taken from: radio (cyan) from [88]; X-ray from Suzaku (green) [95] and from Integral (magenta) [97]; MeV-GeV (red) from *Fermi*-LAT (this work); TeV (blue) from Magic [109].

6.4 Tycho

Tycho Supernova Remnant, also known as SNR G120.1+1.4, is another well studied young SNR in our Galaxy. It originates from the historical Supernova observed in 1572. The historical light curve records [117] and ejecta composition measurements in the X-ray band [118] suggested a Type Ia origin.

The observed radio and X-ray expansion rate suggest that it is in a pre-Sedov evolutional state, even though local region with higher density are in a more advanced stage [119]. In fact, its shape is roughly spherical both in the radio and X-ray bands. Detailed measurements in radio [120] and X-ray [121] showed different expansion rates in the northern, northeastern, and eastern parts compared to the southern part of the shell of the remnant. An expansion index ~ 0.25 (meaning $R_s \propto t^{0.25}$, where R_s is the shell radius) was observed in the eastern part, suggesting that the shock is decelerating due to the collision with a dense clump, while an index ≥ 0.8 was measured in the southwest, where the shock is still in the free expansion phase (see section 2.3.1).

In [122], authors reported on the existence of an azimuthal density variation around the rim of Tycho using Spitzer data, showing that the northeastern region has 3-10 times higher density compared to the southwestern region of the remnant. A large

molecular cloud was observed near Tycho in the northeastern region. Interactions between the northeastern region of the remnant and the molecular cloud were suggested based on radio HI and CO measurements [123, 124].

Radio flux measurements [125] shows a power-law spectrum with a spectral index of 0.6-0.65 and a flux density of 40.5 Jy at 1.4 GHz. A hint of curvature in the radio spectrum, consistent with nonlinear theories, was also reported in [126], who also inferred a magnetic field strength of 100 μG.

X-ray observations showed thin filamentary structures in the rim of Tycho [121, 127–130], coming from the non-thermal X-ray emission of high-energy electrons in a strong magnetic field. This interpretation requires a magnetic field as high as few hundreds μG, confirming the magnetic field amplification. The presence of such a strong magnetic field causes strong radiative energy loss of high-energy electrons, limiting the maximum electron energy to 5-7 TeV [131]. An alternative explanation for such thin filaments is based on mechanisms of magnetic field damping [132], in which case the magnetic field may not be as high. In [133], authors suggested a combination of electron cooling and rapid damping to explain the filamentary structures, predicting a magnetic field as high as 200 μG. Regardless of the mechanism, the small thickness of the X-ray filaments leads to a magnetic field amplification to few hundreds μG.

Deep observations with Chandra revealed a pattern of nearly regularly spaced stripes on the shell surface of non-thermal emission [130] (see figure 6.3). A detailed analysis of the stripes showed that these filaments are associated with an emission on the surface of the SNR. The intensity of the X-ray radiation in the stripes was found to be approximately 25 times the average value of the nearby regions and it is not compatible with an enhancement of the emissivity due to a simple projection of the shell geometry. Authors in [130] interpreted the stripes as arising from the gyration of high-energy protons in a magnetic field and they obtained an estimate of the maximum proton energy in the range 100 TeV - 1 PeV by measuring the gaps between the stripes. In contrast, in [134] authors explained these stripes as the result of magnetic field turbulence, still estimating a maximum proton energy of the order of 1 PeV.

Recent NuSTAR observations in the hard X-ray band [135] were used to study the correlation of the expansion parameters with the X-ray spectral rolloff energy $E_{rolloff}$, i.e. the characteristic cutoff energy of the synchrotron spectrum. From

$E_{rolloff}$, an esitimate on the maximum energy of high energy electrons can be derived, using the relation $E_{max,e} = 120(E_{rolloff}/1keV)^{1/2}(B/1\mu G)^{-1/2}$, where B is the magnetic field. Measurements resulted in a value of $E_{max,e} = 5 - 12$ TeV.

In the γ-rays, *Fermi*-LAT detected Tycho at GeV energies [78], while Veritas studied the source in the TeV range [136]. Latest measurements performed by Veritas [137] suggested a steeper TeV spectral index (2.9 ± 0.4) with respect to the GeV index in [78] (2.14 ± 0.09).

Several models were developed to explain the γ-ray emission from Tycho [138–141] and the multi-wavelength emission from radio to TeV energies [80, 142]. Most of these models interpret the γ-ray emission as the result of the hadronic interaction. Only in [140] a multi-zone model was developed in order to explain the γ-ray spectrum with leptonic emission mechanisms.

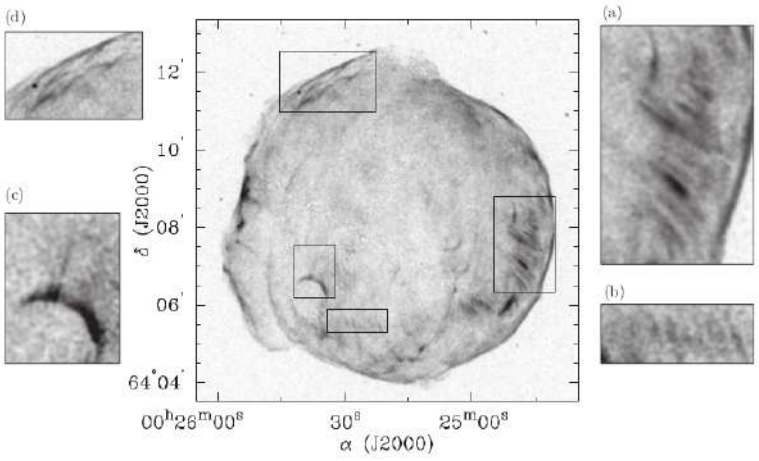

FIGURE 6.3: Chandra X-ray 4.0–6.0 keV image of the Tycho SNR, showing regularly spaced stripes of the non-thermal emission [130].

6.4.1 Modeling results

Also in for Tycho case, data from different energy bands were selected (radio [126], X-ray [143], TeV [137] and combined to the *Fermi*-LAT data derived in this work.

The value of the amplified magnetic field was 300 μG, while the ambient density was fixed to 0.24 cm^{-3}. The inverse Compton scattering was calculated on the CMB photon field and on the infrared (IR) dust emission, with a temperature of 100 K and an energy density of 3.1 eV/cm^3 [80]. A distance of 3.5 kpc was

assumed for Tycho in order to obtain an estimate of the CR energy content in the SNR.

Contrary to Cas A, the simple power-law hypothesis for the proton population allows a good description of the γ-ray data, since the additional cutoff in the proton spectrum does not improve the fit.

Figure 6.4 shows the multi-wavelength spectral points with the best-fit model (black thick line). The colored thin lines represent the individual components.

The electron spectral index well reproduces the radio index, even though a slightly harder value was expected from equation 1.41, given the measured radio index of 0.6-0.65. The electron cutoff energy of 8.5 ± 1.0 TeV is compatible with the X-ray measurements. The γ-ray spectrum is dominated by the hadronic interaction at energies below few hundreds GeV, while the inverse Compton scattering on the dense IR radiation field contributes in the TeV range.

The estimated value of the proton energy content W_p results in an acceleration efficiency of 7%, if the classical explosion energy value of 10^{51} erg is assumed. Finally, the K_{ep} value is found to be approximately equal to 1.6%.

The best-fit parameters are reported in table 6.2.

TABLE 6.2: Best fit parameters of the interpretation model for Tycho SNR.

s_p	s_e	$p_{cut,e}$ (TeV/c)	W_p (erg)	K_{ep}	χ^2/dof
2.50 ± 0.08	2.39 ± 0.03	8.5 ± 1.0	$7.2 \cdot 10^{49}$	1.6%	22.35/32

6.5 Discussion

The models derived for the two SNRs provide a good overall description of the multi-wavelength SEDs. In both cases the γ-ray spectrum is dominated by the hadronic interaction. This is a natural consequence of the multi-wavelength fit. In fact, the high value of the amplified magnetic field limits the accelerated electron energy content, limiting the leptonic components in the γ-ray energy range.

Nevertheless, the proton populations of the two SNRs have different shapes. Cas A is characterized by a spectral index sligthly softer than 2, which is close to what

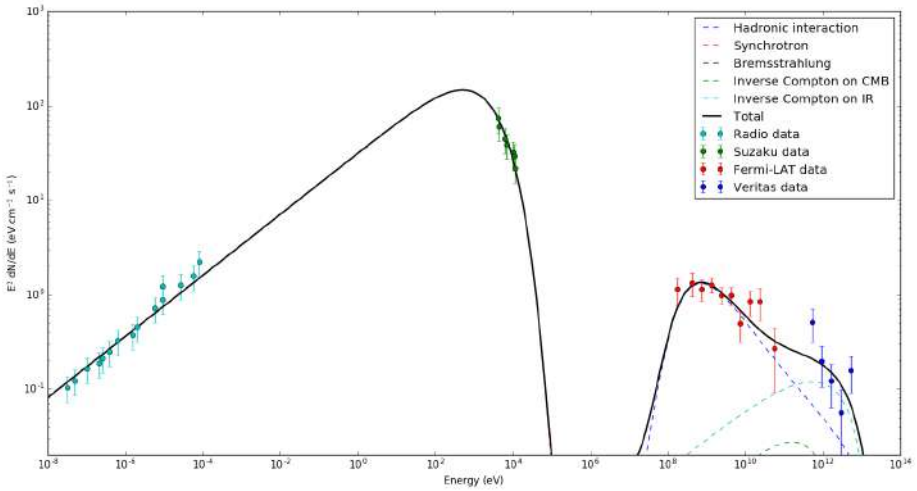

FIGURE 6.4: Multi-wavelength SED of Tycho SNR with the best-fit interpretation model. The thick black line represents the total model, while colored lines the individual components. Data points are taken from: radio (cyan) from [126]; X-ray (green) from Suzaku [143]; MeV-GeV (red) from *Fermi*-LAT (this work); TeV (blue) from Veritas [137].

the DSA theory predicts and is in good agreement with the expected spectral index from direct CR measurements (see section 1.4.4). On the other side, the presence of a cutoff in the proton spectrum suggests that the Cas A is not accelerating CRs at energies above few tens of TeV and is not a good candidate to search for PeV cosmic rays.

The case of Tycho is different. The proton population is characterized by a simple power-law spetrum but a much softer spectral index. This is due to the contribution of the inverse Compton to the TeV γ-rays. It must be noted that if this contribution is reduced (for example with different values of the magnetic field or of the electron cutoff energy), the γ-ray spectrum would be well described by a simple power-law with a spectral index close ot 2.4.

As a comparison, the γ-ray spectra of the two SNRs are compared with models already published in figures 6.5 6.6. Most of the models plotted are based on the hadronic interpretation of the γ-ray spectrum. The only exceptions are the model from [77] for Cas A and from [140] for Tycho. Both these models are still compatible with the GeV and TeV data points.

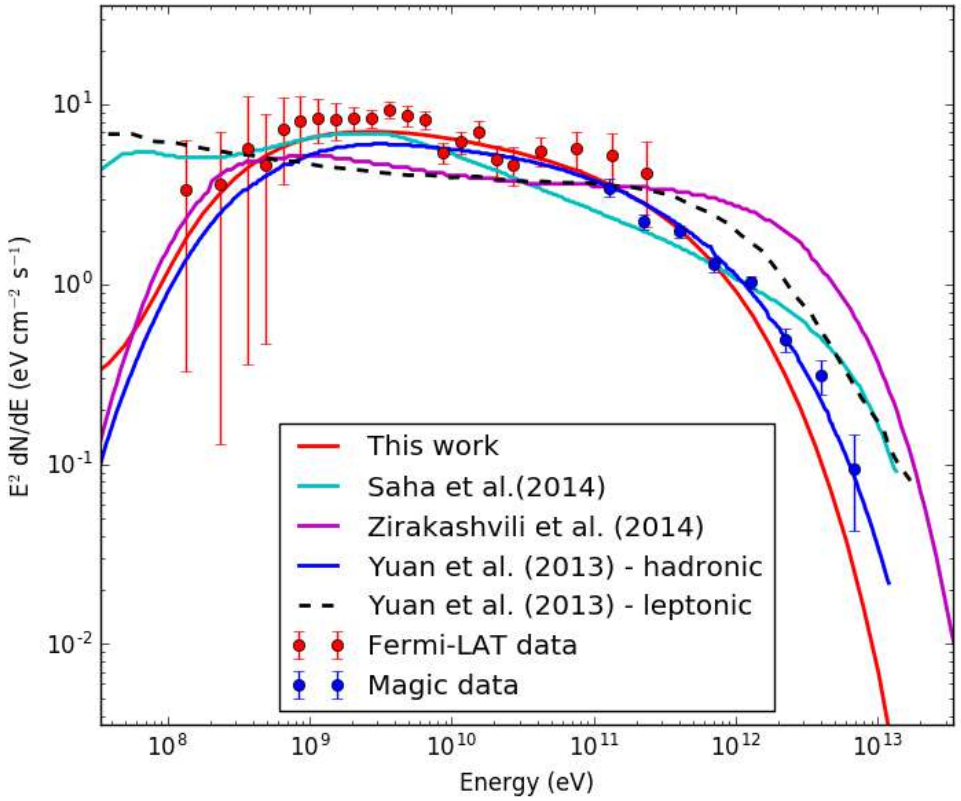

FIGURE 6.5: γ-ray spectrum of Cas A SNR with several hadronic interpretation models (this work (red), [77] (blue), [113] (cyan), [114] (magenta)) and a leptonic model ([77] (dashed black)). Data points are taken from: MeV-GeV (red) from *Fermi*-LAT (this work); TeV (blue) from Magic [109].

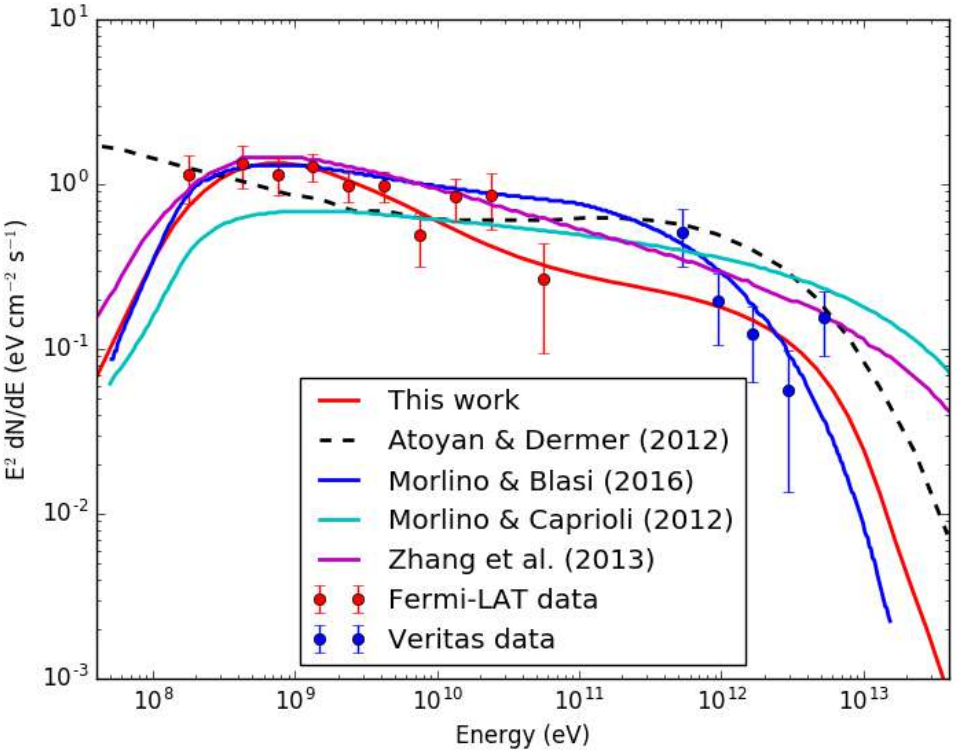

FIGURE 6.6: γ-ray spectrum of Tycho SNR with several hadronic interpretation models (this work (red), [141] (blue), [80] (cyan), [139] (magenta)) and a leptonic model ([140] (dashed black)). Data points are taken from: MeV-GeV (red) from *Fermi*-LAT (this work); TeV (blue) from Veritas [137].

Conclusions

According to the *SNR paradigm*, SNRs are considered the main accelerators of Galactic CRs. The study of the non-thermal emission from this kind of sources can provide information about the CR acceleration mechanism. The γ-ray emission from SNRs could be produced by the decay of neutral pions, generated in the hadronic interactions between relativistic particles (protons or heavier nuclei) and the target gas. In particular, the energy range around and below 100 MeV is crucial to disentangle between leptonic and hadronic contribution to the γ-ray spectrum.

This work focused on the analysis of two young Supernova Remnants (Cassiopeia A and Tycho) with *Fermi*-LAT data in the energy range from 60 MeV to 300 GeV. Using almost 9 years of `Pass 8` data, a detailed analysis of the region surrounding the two SNRs was conducted, with particular attention to the description of the background model. The γ-ray spectra were derived in the energy range analysed. Cas A was well described by a broken power-law function, with spectral indices of -1.64 ± 0.06 and -2.18 ± 0.04 and a spectral break at energy of 1844 ± 394 MeV. The measured integrated flux is $(6.2 \pm 2.9)10^{-8}$ ph. cm^{-2} s^{-1}. Tycho was described by a simple power-law with a spectral index of -2.10 ± 0.06, with an integrated flux of $(2.2 \pm 0.4)10^{-8}$ ph. cm^{-2} s^{-1}. The Spectral Energy Distribution (SED) of the two SNRs was also obtained by performing independent likelihood fits in small energy bands. A different binning was chosen for the two sources depending on their significance.

The systematic uncertainties deriving from the background diffuse model were deeply investigated. The approach based on the usage of the alternative IEMs developed in the first *Fermi*-LAT Supernova Remnant catalog was applied to these SNRs. Systematic uncertainties on the SED points were therefore estimated.

A new approach to estimate the systematic uncertainty from the diffuse model was also developed. This method is based on the study of the residuals of the standard diffuse model along the Galactic plane. An estimate of the systematic error is obtained by evaluating the positive and negative flux of a test source in different positions of the sky. The method was also tested using a Monte Carlo simulation. The results obtained with this new approach are compatible with those derived with the usage of aIEMs. Further improvements of the procedure will lead to a more reliable estimate of the systematic uncertainty, providing a useful method also for catalog analysis.

The measured γ-ray spectra were used to develop an interpretation model of the multi-wavelength photon emission of the two SNRs. The parameters describing the SNR environment (ambient density, magnetic field) were chosen based on radio and X-ray observations. Spectral data points from radio, X-ray and TeV observations were also selected.

The radio to X-ray data were modelled with the synchrotron emission of high energy electrons, while inverse Compton scattering, bremsstrahlung radiation and hadronic interaction contribute to the γ-ray energy range. The hadronic interaction cross sections based on the FLUKA simulation codes were adopted. The model was fit to the data to obtain information on the accelerated proton and electron populations.

In both the SNRs the main contribution to the γ-ray spectrum was due to the accelerated protons. However, the spectral shape of the proton population was different for the two sources. In the case of Cas A, the proton spectrum was described by a power-law in momentum with spectral index of 2.23 ± 0.02 and with an exponential cutoff at 14.8 ± 2.7 TeV/c. The acceleration efficiency was around 2%, while the K_{ep} was found to be approximately 15%. In the case of Tycho, the proton spectrum was well described by a simple power-law in momentum with a spectral index of 2.50 ± 0.08. The acceleration efficiency was about 7% and the K_{ep} was approximately 1.6%. The contribution of the inverse Compton scattering on the infrared radiation field proved to be relevant at energies above few TeVs.

The spectral points were also compared to other already published interpretation models, based on both the leptonic and hadronic origin of the γ-ray spectrum,, showing that no conclusive conlusion can be drawn. Future improvements of the methods developed in this work will provide useful tools to better investigate and

possibly reduce the systematic uncertainties at low energies, in order to obtain more stringent constraints on the interpretation models.

Appendix A

The spectral index of the synchrotron emission

As already discussed in section 1.5, the typical shape of the synchrotron emission covers the radio to X-ray energy band and is peaked[1] around a value which depends on the maximum energy of the relativistic electrons.

One of the most important features of this "peaked" distribution is that a power-law spectral shape for the electron population results in a power-law photon spectrum up to the maximum value of the distribution and the two spectral indices are strictly related:

$$\alpha = \frac{s-1}{2}, \tag{A.1}$$

where s is the spectral index of the electron population and α is the one of the synchrotron emission. This result is very important because few measurements in the radio band give strong constraints on s.

In principle this result can be derived assuming a power-law distribution for $dN/d\gamma$ and solving the integral in equation (1.38). However, it can be derived in a much simpler way.

As can be seen in figure A.1, the synchrotron spectrum emitted by the single electron is peaked. Then, the emission at frequency ν can be supposed to depend only on electrons with Lorentz-factor γ, so that their single-electron spectrum

[1]The typical shape of the photon flux is always a decreasing curve and no peak is visible. The "peak" appears when the flux is represented in the form of Spectral Energy Distribution (SED), i.e. it is multiplied by the factor E^2.

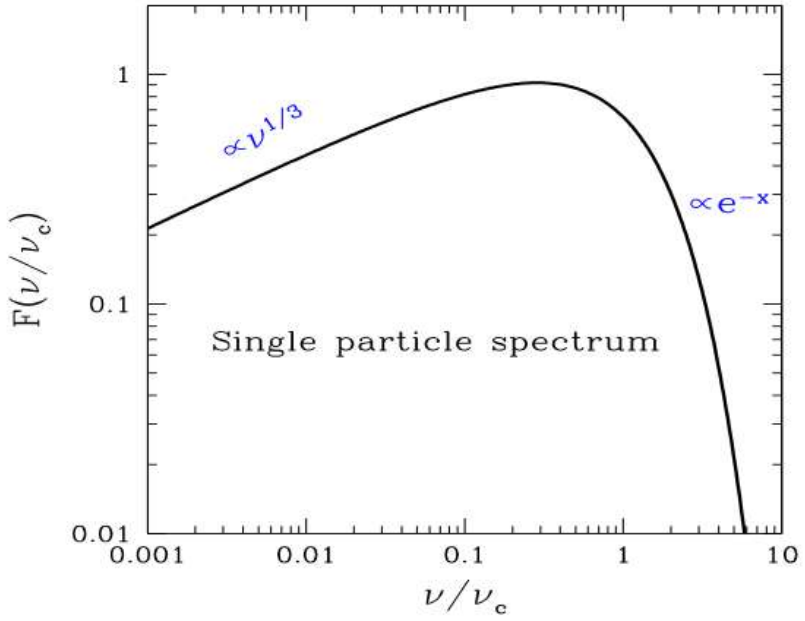

FIGURE A.1: Synchrotron spectrum emitted by a single electron.

peaks at ν. According to equation (1.35), the relation between ν and γ is: $\nu = \gamma^2 \nu_L$. To simplify, assume that the *pitch angle* is 90°. From equations (1.30) and (1.32), the power emitted by a single electron of Lorentz factor γ is:

$$P_e = \frac{2e^2}{3c^3}\gamma^4 a_\perp^2 = \frac{2e^2}{3c^3}\gamma^4 \left(\frac{evB\sin\theta}{\gamma mc}\right)^2 = \frac{2e^4}{3m^2c^3}\gamma^2\beta^2 B^2. \tag{A.2}$$

Be $dN/d\gamma \propto \gamma^{-s}$, the emissivity from the electrons with Lorentz factor γ is:

$$\epsilon_s(\nu)d\nu \propto P_e \frac{dN}{d\gamma}d\gamma \Rightarrow \epsilon_s \propto P_e \frac{dN}{d\gamma}\frac{d\gamma}{d\nu}. \tag{A.3}$$

From the relation $\nu = \gamma^2 \nu_L$, one obtains:

$$\nu = \gamma^2\nu_L \Rightarrow \gamma = \left(\frac{\nu}{\nu_L}\right)^{1/2} \Rightarrow \frac{d\gamma}{d\nu} = \frac{1}{2}\frac{\nu^{-1/2}}{\nu_L^{1/2}}. \tag{A.4}$$

Hence, recalling that $\nu_L \propto B$ and assuming $\beta \approx 1$:

$$\epsilon_s \propto \gamma^2 B^2 \gamma^{-s} \nu^{-1/2} B^{-1/2}. \tag{A.5}$$

Finally, from equation (A.4):

$$\epsilon_s \propto \left(\frac{\nu}{\nu_L}\right)^{(2-s)/2} B^{3/2}\nu^{-1/2} \propto \nu^{1-s/2}B^{s/2-1}B^{3/2}\nu^{-1/2} = B^{(s+1)/2}\nu^{-(s-1)/2}. \quad \text{(A.6)}$$

If $\epsilon_s \propto \nu^{-\alpha}$, then:

$$\alpha = \frac{s-1}{2}, \qquad \text{q.e.d.} \quad \text{(A.7)}$$

Bibliography

[1] Adriani, O. *et al.* "An anomalous positron abundance in cosmic rays with energies 1.5–100 GeV". *Nature* **458,** 07942 (2009).

[2] Accardo, L. *et al.* "High Statistics Measurement of the Positron Fraction in Primary Cosmic Rays of 0.5–500 GeV with the Alpha Magnetic Spectrometer on the International Space Station". *Phys. Rev. Lett.* **113,** 121101 (2014).

[3] Hillas, A. M. "Cosmic Rays: Recent Progress and some Current Questions", arXiv:astro–ph/0607109.

[4] University of Delaware and Bartol Research Institute. *"Neutron Monitor Program"* `http://neutronm.bartol.udel.edu/`.

[5] Patrignani, C. et al. (Particle Data Group). "2016 Review of Particle Physics". *Chin. Phys. C* **40.** `http://pdg.lbl.gov` (2016).

[6] Israel, M. H. *et al.* "Isotopic Composition of Cosmic Rays: Results from the Cosmic Ray Isotope Spectrometer on the ACE Spacecraft". *Nucl. Phys.* **A758,** 201 (2005).

[7] Aguilar, M. *et al.* "Precision Measurement of the Boron to Carbon Flux Ratio in Cosmic Rays from 1.9 GV to 2.6 TV with the Alpha Magnetic Spectrometer on the International Space Station". *Phys. Rev. Lett.* **117,** 231102 (2016).

[8] Adriani, O. *et al.* "Measurement of Boron and Carbon Fluxes in Cosmic Rays with the PAMELA experiment". *Astrophys. Journ.* **791,** 93 (2014).

[9] Abdollahi, S. *et al.* "Cosmic-ray electron-positron spectrum form 7 GeV to 2 TeV with the Fermi Large Area Telescope". *Phys. Rev.* **D95,** 082007 (2017).

[10] Aguilar, M. *et al.* "Precision Measurement of the $(e^+ + e^-)$ Flux in Primary Cosmic Rays from 0.5 GeV to 1 TeV with the Alpha Magnetic Spectrometer on the International Space Station". *Phys. Rev. Lett.* **113,** 221102 (2014).

[11] Aguilar, M. *et al.* "Electron and Positron Fluxes in Primary Cosmic Rays Measured with the Alpha Magnetic Spectrometer on the International Space Station". *Phys. Rev. Lett.* **113,** 121102 (2014).

[12] Ginzburg, V. L. & Ptuskin, V. S. *Rev. Mod. Phys.* **48** (1976).

[13] Strong, A. W. & Moskalenko, I. V. "Propagation of Cosmic-ray Nucleons in the Galaxy". *Astrophys. Journ.* **509,** 212 (1998).

[14] Evoli, C. *et al.* "Cosmic-ray propagation with DRAGON2: I. numerical solver and astrophysical ingredients". *Journ. Cosm. Astrop. Phys.* **2,** 015 (2017).

[15] Longair, M. S. *"High Energy Astrophysics"* 3rd (ed Press, C. U.) (2011).

[16] Amenomori, M. *et al.* "Northern Sky Galactic Cosmic Ray Anisotropy between 10 and 1000 TeV with the Tibet Air Shower Array". *Astrophys. Journ.* **836,** 153 (2017).

[17] Deligny, O. *et al.* "Measurement of Anisotropy and Search for UHECR Sources", arXiv:1702.07209.

[18] Blumenthal, G. R. & Gould, R. J. "Bremsstrahlung, Synchrotron Radiation and Compton Scattering of High-Energy Electrons Traversing Diluted Gases". *Rev. Mod. Phys.* **42,** 237 (1970).

[19] Baring, M. G. *et al.* "Radio to gamma-ray emission form shell-type Supernova Remnants: predictions from non-linear acceleration models". *Astrophys. Journ.* **513,** 311 (1999).

[20] Kamae, T. *et al.* "Diffractive interaction and scaling violation in $pp \to \pi^0$ interaction and GeV excess in Galactic diffuse gamma-ray spectrum of EGRET". *Astrophys. Journ.* **620,** 244 (2005).

[21] Kamae, T. *et al.* "Parametrization of γ, $e^{\pm}$ and neutrino spectra produced by $p-p$ interaction in astronomical environments". *Astrophys. Journ.* **647,** 692 (2006).

[22] Mazziotta, M. N. *et al.* "Production of secondary particles and nuclei in cosmic rays collisions with the interstellar gas using the FLUKA code". *Astrop. Phys.* **81,** 21 (2016).

[23] Hirata, K. *et al.* "Observation of a neutrino burst from the supernova SN1987A". *Phys. Rev. Lett.* **58,** 1490 (1987).

[24] Bionta, R. M. *et al.* "Observation of a neutrino burst in coincidence with supernova 1987A in the Large Magellanic Cloud". *Phys. Rev. Lett.* **58,** 1494 (1987).

[25] Riess, A. G. *et al.* "New Hubble Space Telescope Discoveries of Type Ia Supernovae at $z \geq 1$: Narrowing Constraints on the Early Behavior of Dark Energy". *Astrophys. Journ.* **659,** 98 (2007).

[26] Green, D. A. "A catalogue of 294 Galactic supernova remnants". *Bull. Astron. Soc. India.* **42,** 47 (2014).

[27] Ferrand, G. *et al.* "A census of high-energy observations of Galactic supernova remnants". *Advances in Space Research* **49,** 1313 (2012).

[28] Fermi, E. "On the Origin of the Cosmic Radiation". *Phys. Rev.* **75,** 1169 (1949).

[29] Fermi, E. "Galactic Magnetic Fields and the Origin of Cosmic Radiation". *Astrophys. Journ.* **119,** 1 (1954).

[30] Blasi, P. "The Origin of Galactic Cosmic Rays". *Astron. Astrophys. Rev.* **21,** 70 (2013).

[31] Blasi, P., Gabici, S. & Vannoni, G. "On the role of injection in kinetic approaches to nonlinear particle acceleration at non-relativistic shock waves". *Month. Not. Royal Astron. Soc.* **361,** 907 (2005).

[32] Bell, A. R. "Turbulent amplification of magnetic field and diffusive shock acceleration of cosmic rays". *Month. Not. Royal Astron. Soc.* **353,** 550 (2004).

[33] Ackermann, M. *et al.* "Detection of the Characteristic Pion-Decay Signature in Supernova Remnants". *Science* **339,** 807 (2013).

[34] Jogler, T. & Funk, S. "Revealing W51C as a Cosmic Ray Source Using Fermi-LAT Data". *Astrophys. Journ.* **816,** 100 (2016).

[35] Cardillo, M. *et al.* "Supernova remnant W44: a case of cosmic-ray reacceleration". *Astron. Astrophys.* **595,** A58 (2016).

[36] Abdo, A. A. *et al.* "Observations of the Young Supernova Remnant RX J1713.7–3946 with the Fermi Large Area Telescope". *Astrophys. Journ.* **734,** 28 (2011).

[37] Ajello, M. *et al.* "Deep morphological and spectral study of the SNR RCW 86 with Fermi-LAT". *Astrophys. Journ.* **819,** 98 (2016).

[38] Acero, F. *et al.* "The First *Fermi*-LAT Supernova Remnant Catalog". *Astrophys. Journ. Suppl. Series* **224,** 8 (2016).

[39] Green, D. A. *Bull. Astron. Soc. India.* **37,** 45 (2009).

[40] Abdo, A. A. *et al.* "The on-orbit calibration of the Fermi Large Area Telescope". *Astrop. Phys.* **32,** 193 (2009).

[41] Atwood, W. B. *et al.* "The Large Area Telescope on the *Fermi Gamma-ray Space Telescope* Mission". *Astrophys. Journ.* **697,** 1071 (2009).

[42] Moiseev, A. A. *et al.* "The anti-coincidence detector for the GLAST large area telescope". *Astrop. Phys.* **27,** 339 (2007).

[43] Ackermann, M. *et al.* "Measurement of Separate Cosmic-Ray Electron and Positron Spectra with the Fermi Large Area Telescope". *Phys. Rev. Lett.* **108,** 011103 (2012).

[44] Rando, R. "Post-launch performance of the Fermi Large Area Telescope", arXiv:0907.0626v1.

[45] Ackermann, M. *et al.* "The Fermi Large Area Telescope on orbit: event classification, instrument response functions, and calibration". *Astrophys. Journ. Suppl. Series* **203,** 4 (2012).

[46] Bregeon, J. "*Fermi*-LAT data reprocessed with updated calibration constants", arXiv:1304.5456v3.

[47] Atwood, W. *et al.* "Pass 8: Toward the full realization of the *Fermi*-LAT scientific potential", arXiv:1303.3514v1.

[48] Cowan, G. *"Statistical Data Analysis"* 1st (ed Oxford, C. P.) (1998).

[49] Wilk, S. S. "The Large-Sample Distribution of the Likelihood Ratio for Testing Composite Hypotheses". *Ann. Math. Stat.* **9,** 60 (1938).

[50] *Minuit Library* `http://wwwasdoc.web.cern.ch/wwwasdoc/minuit/minmain.html`; `http://seal.web.cern.ch/seal/MathLibs/Minuit2/html/index.html`.

[51] Giordano, F. *"Extension studies of galactic sources with Fermi"* in *High-energy Emission from Pulsars and Their Systems* (eds Rea, N. & Torres, D. F.) (2011), 69.

[52] Lande, J. *et al.* "Search for Spatially Extended *Fermi* Large Area Telescope Sources Using Two Years of Data". *Astrophys. Journ.* **756,** 5 (2012).

[53] Kerr, M. *"Likelihood Methods for the Detection and Characterization of Gamma-ray Pulsars with the Fermi Large Area Telescope"* PHD Thesis (University of Washington, 2010).

[54] Abdo, A. A. *et al.* "*Fermi* Large Area Telescope First Source Catalog". *Astrophys. Journ. Suppl. Series* **188,** 405 (2010).

[55] Nolan, P. L. *et al.* "*Fermi* Large Area Telescope Second Source Catalog". *Astrophys. Journ. Suppl. Series* **199,** 31 (2012).

[56] Acero, F. *et al.* "*Fermi* Large Area Telescope Third Source Catalog". *Astrophys. Journ. Suppl. Series* **218,** 23 (2015).

[57] Wood, M. *et al.* "Fermipy: an open-source Python package for analysis of *Fermi*-LAT data", arXiv:1707.09551v1.

[58] Lebrun, F. & Paul, J. A. "Gamma-Ray Astronomy and Structure and Content of the Local Interstellar Medium". *Proc. 16th ICRC (Kyoto)* **12,** 13 (1979).

[59] Lebrun, F. *et al.* "COS-B gamma-ray measurements, cosmic rays and the local interstellar medium". *Astron. Astrophys.* **107,** 390 (1982).

[60] Strong, A. W. *et al.* "The local interstellar medium as traced by gamma rays". *Astron. Astrophys.* **115,** 404 (1982).

[61] Acero, F. *et al.* "Development of the model of Galactic Interstellar Emission for Standard Point-source analysis of Fermi Large Area Telescope Data". *Astrophys. Journ. Suppl. Series* **223,** 26 (2016).

[62] Ackermann, M. *et al.* "FERMI-LAT OBSERVATIONS OF THE DIFFUSE γ-RAY EMISSION: IMPLICATIONS FOR COSMIC RAYS AND THE INTERSTELLAR MEDIUM". *Astrophys. Journ.* **750,** 3 (2012).

[63] Abdo, A. A. *et al.* "Fermi Observations of Cassiopeia and Cepheus: diffuse gamma-ray emission in the outer Galaxy". *Astrophys. Journ.* **710,** 133 (2010).

[64] Gaggero, D. *et al.* "Gamma-ray sky points to radial gradients in cosmic-ray transport". *Phys. Rev.* **D91** (2015).

[65] Kalberla, P. M. W. *et al.* "The Leiden/Argentine/Bonn (LAB) Survey of Galactic HI". *Astron. Astrophys.* **440,** 775 (2005).

[66] Dame, T. M. *et al.* "The Milky Way in Molecular Clouds: A New Complete CO Survey". *Astrophys. Journ.* **547,** 792 (2001).

[67] Shetty, R. *et al.* "Modelling CO emission - II. The physical characteristics that determine the X factor in Galactic molecular clouds". *Month. Not. Royal Astron. Soc.* **415,** 3253 (2011).

[68] Schlegel, D. J., Finkbeiner, D. P. & Davis, M. "Maps of dust infrared emission for use in estimation of reddening and cosmic microwave background radiation foregrounds". *Astrophys. Journ.* **500,** 525 (1998).

[69] Abergel, A. *et al.* "Planck 2013 results. XI. All-sky model of thermal dust emission". *Astron. Astrophys.* **571,** A11 (2014).

[70] Abdo, A. A. *et al.* "Fermi Large Area Telescope Observations of Two Gamma-Ray Emission Components from the Quiescent Sun". *Astrophys. Journ.* **734,** 116 (2011).

[71] Abdo, A. A. *et al.* "Fermi Observations of γ-Ray Emission from the Moon". *Astrophys. Journ.* **758,** 140 (2012).

[72] Gould, R. J. "High-Energy Bremsstrahlung in Collisions of Electrons with One and Two-Electron Atoms". *Phys. Rev.* **185,** 72 (1969).

[73] Shikaze, Y. *et al.* "Measurements of 0.2–20 GeV/n cosmic-ray proton and helium spectra from 1997 through 2002 with the BESS spectrometer". *Astrop. Phys.* **28,** 154 (2007).

[74] Case, G. L. & Bhattacharya, D. "A New Σ-D Relation and Its Application to the Galactic Supernova Remnant Distribution". *Astrophys. Journ.* **504,** 761 (1998).

[75] Lorimer, D. R. *et al. Month. Not. Royal Astron. Soc.* **372,** 777 (2006).

[76] Abdo, A. A. *et al.* "Fermi-LAT discovery of GeV gamma-ray emission from the young Supernova Remnant Cassiopeia A". *Astrophys. Journ. Lett.* **710,** L92 (2010).

[77] Yuan, Y. *et al.* "Fermi-LAT Detection of a Break in the Gamma-Ray Spectrum of the Supernova Remnant Cassiopeia A". *Astrophys. Journ.* **779,** 117 (2013).

[78] Giordano, F. *et al.* "Fermi-LAT Detection of the Young SuperNova Remnant Tycho". *Astrophys. Journ.* **744,** L2 (2012).

[79] Acero, F. *et al.* "Fermi-LAT Observations of High Energy γ-Ray Emission toward the Galactic center". *Astrophys. Journ.* **819,** 44 (2016).

[80] Morlino, G. & Caprioli, D. "Strong evidence for hadron acceleration in Tycho's supernova remnant ". *Astron. Astrophys.* **538,** A81 (2012).

[81] Reed, J. E. *et al.* "The Three-dimensional Structure of the Cassiopeia A Supernova Remnant. I. The Spherical Shell". *Astrophys. Journ.* **440,** 706 (1995).

[82] Medd, W. J. & Ramana, K. V. V. "Flux-Density Measurements at 3.15 Gc/s". *Astrophys. Journ.* **142,** 383M (1965).

[83] Allen, R. J. & Barrett, A. H. "Absolute Measurements of the Radio Flux from Cassiopeia A and Taurus A at 3.64 and 1.94 cm". *Astrophys. Journ.* **149,** 1A (1967).

[84] Parker, E. A. "Precise Measurements of the Flux Densities of the Radio Sources Cas A and Cyg A at metre wavelengths". *Month. Not. Royal Astron. Soc.* **138,** 407 (1968).

[85] Braude, S. Y. *et al.* "The Spectra of Discrete Radio Sources at Decametric Wavelengths-I". *Month. Not. Royal Astron. Soc.* **143,** 289 (1969).

[86] Braude, S. Y. *et al.* "The Spectra of Discrete Radio Sources at Decametric Wavelengths-II". *Month. Not. Royal Astron. Soc.* **143,** 301 (1969).

[87] Bell, A. R. *et al.* "New radio map of Cassiopeia A at 5 GHz". *Nature* **257,** 463 (1975).

[88] Baars, J. W. M. *et al.* "The Absolute Spectrum of Cas A; An Accurate Flux Density Scale and a Set of Secondary Calibrators". *Astron. Astrophys.* **61,** 99 (1977).

[89] Tuffs, R. J. "Secular changes within Cassiopeia A at 5 GHz-I". *Month. Not. Royal Astron. Soc.* **219,** 13 (1986).

[90] Braun, R. *et al.* "Physical process which shapes Cassiopeia A". *Nature* **327,** 395 (1987).

[91] Anderson, M *et al.* "Relativistic Electron Populations in Cassiopeia A". *Astrophys. Journ.* **373,** 146 (1991).

[92] Kassim, N. E. *et al.* "Evidence for Thermal Absorption inside Cassiopeia A". *Astrophys. Journ. Lett.* **455,** L59 (1995).

[93] Gotthelf, E. V. *et al.* "Chandra Detection of the Forward and Reverse Shocks in Cassiopeia A". *Astrophys. Journ. Lett.* **552,** L39 (2001).

[94] Hwang, U. *et al.* "A Million Second Chandra View of Cassiopeia A". *Astrophys. Journ. Lett.* **615,** L117 (2004).

[95] Maeda, Y. *et al.* "Suzaku X-Ray Imaging and Spectroscopy of Cassiopeia A". *Pub. Astron. Soc. Japan* **61,** 121 (2009).

[96] Grefenstette, B. W. *et al.* "Locating the Most Energetic Electrons in Cassiopeia A". *Astrophys. Journ.* **802,** 15 (2015).

[97] Wang, W. & Li, Z. "Hard X-Ray Emissions from Cassiopeia A Observed by INTEGRAL". *Astrophys. Journ.* **825,** 102 (2016).

[98] Anderson, M. C. & Rudnick, L. "The deceleration powering of synchrotron emission from ejecta components in supernova remnant Cassiopeia A". **441,** 307 (1995).

[99] Delaney, T. & Rudnick, L. "The First Measurement of Cassiopeia A's Forward Shock Expansion Rate". *Astrophys. Journ.* **589,** 818 (2003).

[100] Patnaude, D. J. & Fesen, R. A. "Proper motions and brightness variation of nonthermal X-ray filaments in Cassiopeia A Supernova Remnants". *Astrophys. Journ.* **697,** 535 (2009).

[101] Morse, J. A. *et al.* "Location of the Optical Reverse Shock in the Cassiopeia A Supernova Remnant". *Astrophys. Journ.* **614,** 727 (2004).

[102] Patnaude, D. J. & Fesen, R. A. "Small-scale X-ray variability in the Cassiopeia A Supernova Remnant". *Astron. Journ.* **133,** 147 (2007).

[103] Helder, E. A. & Vink, J. "Characterizing the Nonthermal Emission of Cassiopeia A". *Astrophys. Journ.* **686,** 1094 (2008).

[104] Uchiyama, Y & Aharonian, F. A. "Fast Variability of Nonthermal X-Ray Emission in Cassiopeia A: Probing Electron Acceleration in Reverse-Shocked Ejecta". *Astrophys. Journ. Lett.* **677,** L105 (2008).

[105] Siegert, T. *et al.* "Revisiting INTEGRAL/SPI observations of ^{44}Ti from Cassiopeia A". *Astron. Astrophys.* **579,** A124 (2015).

[106] Aharonian, F. *et al.* "Evidence for TeV gamma ray emission from Cassiopeia A". *Astron. Astrophys.* **379,** 112 (2001).

[107] Albert, J. *et al.* "Observation of VHE -rays from Cassiopeia A with the MAGIC telescope". *Astron. Astrophys.* **474,** 937 (2007).

[108] Acciari, V. A. *et al.* "Observations of the Shell-type Supernova Remnant Cassiopeia A at TeV Energies with VERITAS". *Astrophys. Journ.* **714,** 163 (2010).

[109] Ahnen, M. L. *et al.* "A cut-off in the TeV gamma-ray spectrum of the SNR Cassiopeia A". *Month. Not. Royal Astron. Soc.* **472,** 2956 (2017).

[110] Holder, J. *"Latest Results from VERITAS: Gamma 2016"* in *Proc. of the 6th International Symposium on High-Energy Gamma-Ray Astronomy - Gamma2016* (), arXiv:1609.02881.

[111] Berezhko, E. G. *et al.* "Gamma-ray emission from Cassiopeia A produced by accelerated cosmic rays". *Astron. Astrophys.* **400,** 971 (2003).

[112] Vink, J. & Laming, J. M. "On the Magnetic Fields and Particle Acceleration in Cassiopeia A". *Astrophys. Journ.* **584,** 758 (2003).

[113] Saha, L. *et al.* "Origin of gamma-ray emission in the shell of Cassiopeia A". *Astron. Astrophys.* **563,** A88 (2014).

[114] Zirakashvili, V. N. *et al.* "Nonthermal radiation of young Supernova Remnants: the case of Cas A". *Astrophys. Journ.* **785,** 130 (2014).

[115] Mezger, P. G. *et al.* "Maps of Cassiopeia A and the Crab Nebula at λ 1.2 mm". *Astron. Astrophys.* **167,** 145 (1986).

[116] Laming, J. M. & Hwang, U. "On the Determination of Ejecta Structure and Explosion Asymmetry from the X-Ray Knots of Cassiopeia A". *Astron. Astrophys.* **597,** 347 (2003).

[117] Baade, W. "B Cassiopeiae as a Supernova of Type I". *Astrophys. Journ.* **102,** 309 (1945).

[118] Decourchelle, A. *et al.* "XMM-Newton observation of the Tycho supernova remnant". *Astron. Astrophys.* **365,** L218 (2001).

[119] Aharonian, F. A. *et al.* "A study of Tycho's SNR at TeV energies with the HEGRA CT-System ". *Astron. Astrophys.* **373,** 292 (2001).

[120] Reynoso, E. M. *et al.* "A VLA Study of the Expansion of Tycho's Supernova Remnant". *Astrophys. Journ.* **491,** 816 (1997).

[121] Katsuda, S. *et al.* "X-ray Measured Dynamics of Tycho's Supernova Remnant". *Astrophys. Journ.* **709,** 1387 (2010).

[122] Williams, B. J. *et al.* "Azimuthal Density Variations around the Rim of Tycho's Supernova Remnant". *Astrophys. Journ.* **770,** 129 (2013).

[123] Reynoso, E. M. *et al.* "The Environs of Tycho's Supernova Remnant Explored through the H I 21 Centimeter Line". *Astron. Journ.* **117,** 1827 (1999).

[124] Lee, J. J. *et al.* "The Environment of Tycho: Possible Interaction with the Molecular Cloud". *Astrophys. Journ. Lett.* **605,** L113 (2004).

[125] Kothes, R. *et al.* "A catalogue of Galactic supernova remnants from the Canadian Galactic plane survey - I. Flux densities, spectra, and polarization characteristics". *Astron. Astrophys.* **457,** 1081 (2006).

[126] Reynolds, S. P. & Ellison, D. C. "Electron Acceleration in Tycho's and Kepler's Supernova Remnants: Spectral Evidence of Fermi Shock Acceleration". *Astrophys. Journ. Lett.* **339,** L75 (1992).

[127] Hwang, U. *et al.* "Thermal and Nonthermal X-Ray Emission from the Forward Shock in Tycho's Supernova Remnant". *Astrophys. Journ.* **581,** 1101 (2002).

[128] Bamba, A. *et al.* "A Spatial and Spectral Study of Nonthermal Filaments in Historical Supernova Remnants: Observational Results with Chandra". *Astrophys. Journ.* **621,** 793 (2005).

[129] Warren, J. S. *et al.* "Cosmic-Ray Acceleration at the Forward Shock in Tycho's Supernova Remnant: Evidence from Chandra X-Ray Observations". *Astrophys. Journ.* **634,** 376 (2005).

[130] Eriksen, K. A. *et al.* "Evidence for Particle Acceleration to the Knee of the Cosmic Ray Spectrum in Tycho's Supernova Remnant". *Astrophys. Journ. Lett.* **728,** L28 (2011).

[131] Parizot, E. *et al.* "Observational constraints on energetic particle diffusion in young supernovae remnants: amplified magnetic field and maximum energy". *Astron. Astrophys.* **453,** 387 (2006).

[132] Pohl, M. *et al.* "Magnetically Limited X-Ray Filaments in Young Supernova Remnants". *Astrophys. Journ. Lett.* **626,** L101 (2005).

[133] Cassam-Chenaï, G. *et al.* "The Blast Wave of Tycho's Supernova Remnant". *Astrophys. Journ.* **665,** 315 (2007).

[134] Bykov, A. M. *et al.* "X-ray Stripes in Tycho's Supernova Remnant: Synchrotron Footprints of a Nonlinear Cosmic-ray-driven Instability". *Astrophys. Journ. Lett.* **735,** L40 (2011).

[135] Lopez, L. A. *et al.* "A Spatially Resolved Study of the Synchrotron Emission and Titanium in Tycho's Supernova Remnant Using NuSTAR". *Astrophys. Journ.* **814,** 132 (2015).

[136] Acciari, V. A. *et al. Astrophys. Journ.* **730,** L20 (2011).

[137] Archambault, S. *et al.* "Gamma-ray observations of Tycho's supernova remnant with VERITAS and Fermi". *Astrophys. Journ.* **836,** 23 (2017).

[138] Berezhko, E. G. *et al.* "The Nature of Gamma-Ray Emission of Tycho's Supernova Remnant". *Astrophys. Journ.* **763,** 14 (2013).

[139] Zhang, X. *et al.* "On the hadronic γ-ray emission from Tycho's supernova remnant". *Month. Not. Royal Astron. Soc. Lett.* **429,** L25 (2013).

[140] Atoyan, A. & Dermer, C. D. "Gamma Rays from the Tycho Supernova Remnant: Multi-zone versus Single-zone Modeling". *Astrophys. Journ. Lett.* **749,** L26 (2012).

[141] Morlino, G. & Blasi, P. "Spectra of accelerated particles at supernova shocks in the presence of neutral hydrogen: the case of Tycho". *Astron. Astrophys.* **589,** A7 (2016).

[142] Slane, P. *et al.* "A CR-hydro-NEI Model of the Structure and Broadband Emission from Tycho's Supernova Remnant". *Astrophys. Journ.* **783,** 33 (2014).

[143] Tawagawa, T. *et al.* "Suzaku Observations of Tycho's Supernova Remnant". *Pub. Astron. Soc. Japan* **61,** 167 (2009).